# CAPTURING THE IMPACT OF MODEL ERROR ON STRUCTURAL DYNAMIC ANALYSES DURING DESIGN EVOLUTION

by

Alissa Naomi Clawson

B.S., Aerospace Engineering
Boston University, 1999

SUBMITTED TO THE DEPARTMENT OF AERONAUTICS AND ASTRONAUTICS
IN PARTIAL FULFILLMENT OF THE REQUIREMENTS FOR THE DEGREE OF

MASTER OF SCIENCE
IN AERONAUTICS AND ASTRONAUTICS

at the

MASSACHUSETTS INSTITUTE OF TECHNOLOGY

August 24, 2001





Signature of Author .....
Alissa N. Clawson, Department of Aeronautics and Astronautics
August 24, 2001

Certified by .....
David W. Miller, Assistant Professor of Aeronautics and Astronautics
Thesis Supervisor

Accepted by .....
Wallace E. Vander Velde, Professor of Aeronautics and Astronautics
Chairman, Department Graduate Committee

# Capturing the Impact of Model Error on Structural Dynamic Analyses During Design Evolution

by

ALISSA NAOMI CLAWSON

Submitted to the Department of Aeronautics and Astronautics
on August 24, 2001 in Partial Fulfillment of the
Requirements for the Degree of
Master of Science in Aeronautics and Astronautics

ABSTRACT

Space telescopes are complex structures, with stringent performance requirements which must be met while conforming to design constraints. In order to ensure that the performance requirements are met, accurate models of all the different components of the integrated model is needed. In modeling the structure, however, early in the project, the design is not complete when analysis starts and key design decisions are made. Knowledge of how the model fidelity evolves as the design or model improves helps with the interpretation of the analysis such that only the appropriate information from the data will be used. In this thesis, model fidelity evolution is studied to understand what key information can be gathered at the different stages of fidelity and what error types to expect. First, a simple truss problem is used as an example of the different stages of model fidelity by using four different types of models: Bernoulli-Euler beam, Timoshenko beam, truss with rod members and truss with bending members. Then, the Origins Testbed is used as an example of a completed design to parallel model updating error to design fidelity error. Finally, the ARGOS testbed is introduced as a low fidelity model. The conclusions drawn from the Origins Testbed and example problem are applied to the results of a disturbance analysis of ARGOS.

Thesis Supervisor: David W. Miller
Title: Assistant Professor of Aeronautics and Astronautics

# ACKNOWLEDGMENTS

I would like to thank (NOT in order of importance):

- the U.S. Navy for the FY99 scholarship that allowed me to work for my Masters Degree (and for letting me fly),

- my parents for encouraging their children to be intelligent, independent, and hard working people,

- my friends for persuading me to not study ALL the time,

- the SSL for being an awesome group of students, faculty and staff, who all made life at MIT fun,

- Becky Masterson, who (who's "who"?) probably has this (what does "this" mean?) entire thesis memorized,

- the PIT crew for just being,

- my BU girls for being the sisters I never had,

- my advisor, Prof. Miller, for directing my thesis,

- and Prof. JP Clarke for helping me in the beginning when I was lost in the shuffle.

# TABLE OF CONTENTS

# LIST OF FIGURES

# LIST OF TABLES

# NOMENCLATURE

## Abbreviations

| | |
|---|---|
| AFRL | Air Force Research Laboratory |
| ARGOS | Active Reconnaissance Golay-3 Optical Satellite |
| BE | Bernoulli-Euler |
| CCD | Charged Couple Device |
| CDIO | Conceive, Design, Implement, Operate |
| CG | center of gravity |
| COBE | Cosmic Background Explorer |
| DOCS | Dynamics, Optics, Controls, Structures |
| dof | degree of freedom |
| FE | Finite Element |
| FEM | Finite Element Model |
| FRF | frequency response function |
| FOV | field of view |
| GSFC | Goddard Space Flight Center |
| GUI | Graphical User Interface |
| IEEE | Institute of Electrical and Electronics Engineers |
| ISO | Infrared Space Observatory |
| ISS | International Space Station |
| LBT | Large Binocular Telescope |
| MACE | Middeck Active Control Experiment |
| MIT | Massachusetts Institute of Technology |
| MTF | Modulation Transfer Function |
| NASA | National Aeronautics and Space Administration |
| NGST | Next Generation Space Telescope |
| NICMOS | Near Infrared Camera and Multi-Object Spectrometer |
| NRO | National Reconnaissance Office |
| OPD | Optical Path-Length Difference [m] |
| OPL | Optical Path Length [m] |
| OT | Origins Testbed |
| PDE | Partial Differential Equation |
| PDR | Preliminary Design Review |
| PSF | Point Spread Function |
| RBM | rigid body mode |
| RMS | root mean square |
| RSS | root sum squared |
| RWA | Reaction Wheel Assembly |
| SIM | Space Interferometry Mission |
| SIRTF | Space Infrared Telescope Facility |

| | |
|---|---|
| SPIE | International Society for Optical Engineering |
| SSL | Space Systems Laboratory |

## Symbols

| | |
|---|---|
| A | area [$m^2$] |
| A | state space dynamics matrix |
| B | state space input matrix |
| C | state space output matrix |
| d | unit intensity Gaussian white noise |
| d | diameter [m] |
| D | state space feed through matrix |
| E | Young's modulus [Pa] |
| f | frequency [Hz] |
| F | force [N] |
| g | gravitational acceleration [m/s2] |
| G | modulus of elasticity in shear [Pa] |
| G | transfer function |
| I | Moment of Inertia [$m^4$] |
| J | rotary inertia per unit length [kg m] |
| J | cost function |
| k | stiffness [N/m] |
| k' | shear area factor |
| K | stiffness matrix |
| l | length [m] |
| m | mass [kg] |
| m | mass per unit length [kg/m] |
| m | meter |
| $m_j$ | $j^{th}$ modal mass |
| M | mass matrix |
| q | state variables |
| r | radius [m] |
| u(x,t) | axial translational displacement of a beam [m] |
| V | volume [$m^3$] |
| w(x,t) | transverse translational displacement of a beam [m] |
| w | physical plant disturbances (shaped noise) |
| y | (sensor) output |
| z | performance |
| $\beta$ | slope of deflection curve due to shear |
| $\lambda$ | eigenvalue [radian/$s^{-2}$] |
| $\nu$ | Poisson's ratio |
| $\rho$ | mass density [kg/$m^3$] |
| $\phi_j$ | $j^{th}$ mode shape, eigenvector |

| | |
|---|---|
| $\Phi$ | modal matrix |
| $\psi$ | slope of deflection curve when shear is neglected |
| $\omega_j$ | $j^{th}$ modal frequency, natural frequency, eigenvalue [radians/s] |
| $\Omega$ | matrix of natural frequencies |

# Chapter 1

# INTRODUCTION

## 1.1 Background

*"For the first time in history, humanity is on the verge of having the technological capability to explore age-old questions about our cosmic origins and the possibility of life beyond Earth." - NASA Origins Program Web Site*[1]

### 1.1.1 NASA Origins Program

"Where do we come from?"

"Are there others out there like us?"

These two fundamental philosophical questions have perplexed humans since the beginning of civilization, yet humanity is only now entering the age with the technological capabilities to answer them. NASA has decided to foster those technologies and has created a program called Origins. These two questions drive four science goals that guide the direction of the program:

1. To understand how galaxies formed in the early universe.
2. To understand how stars and planetary systems form and evolve.

1. http://origins.jpl.nasa.gov/missions/missions.html

3. To determine whether habitable or life-bearing planets exist around nearby stars.
4. To understand how life forms and evolves.

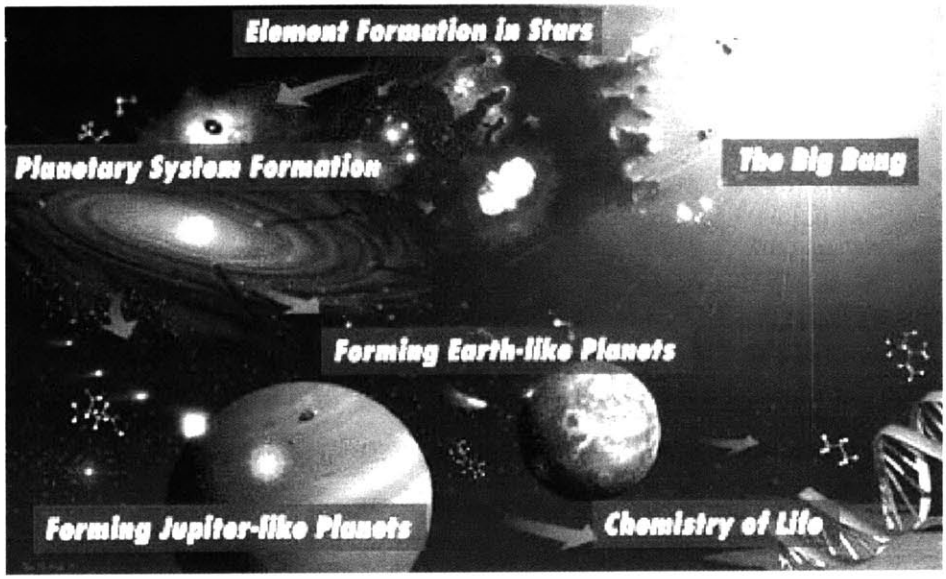


**Figure 1.1** Timeline of the Universe[a]

a. http://origins.jpl.nasa.gov

The knowledge of the universe is limited to the extremes of its timeline. Existing space-based and ground-based observatories provide ample knowledge of the present and recent past (roughly 10-15 billion years since the big bang). There is also knowledge of the primordial beginnings of the universe (through roughly 1 million years) via cosmic microwave background radiation (Cosmic Background Explorer (COBE)) and high energy particle physics.[1] However, very little is known about the period beginning 1 million years after the big bang and ending in the recent past. It is during this period that complex structures such as galaxies, stars, and planets began to form. Very little information exists about the processes governing the formation of the earliest space structures, and this information is the key to understanding how our own galaxy, solar system and planet were created.

1. http://www.ngst.nasa.gov/science/Goals.html

The first two science goals require an observatory that is capable of imaging the missing portion of the timeline.

Meeting the third science goal requires the ability to detect extrasolar planets capable of sustaining life. Planet detection technology is currently limited to passive means by measuring the wobble of parent stars. The frequency of the wobble indicates the period of the orbit, and the amplitude of the wobble indicates the mass and thus the size of its orbit. This method is limited by the minimum wobble detectable. Current observatories are restricted to measuring wobbles induced by Jupiter-sized planets in close orbits around nearby stars. Such planets are thought to be too large and too close to the parent star to sustain life. Planets that have similar mass and orbits to Earth are undetectable with current technologies.

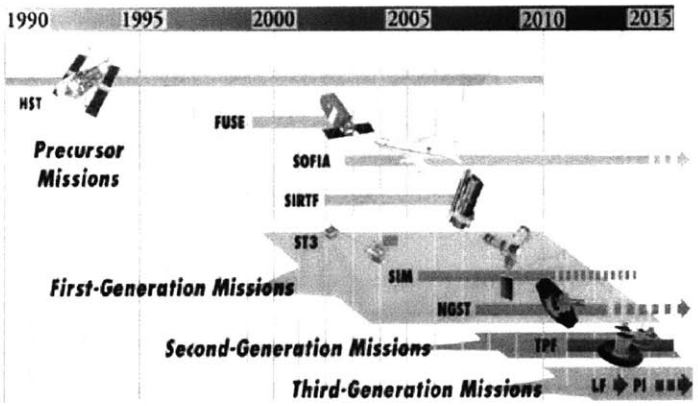


**Figure 1.2** Space Telescope Timeline[a]

a. http://origins.jpl.nasa.gov

The timeline of the telescopes planned for the NASA Origins Program is shown in Figure 1.2. Each new telescope incorporates technology and lessons learned from its predecessor. Therefore, only small increases in technology rather than major jumps need be developed for each new mission. The MIT Space Systems Laboratory (SSL) has assisted NASA on the analyses of several of the Origins Program telescopes. Two of the telescopes

discussed below are the Next Generation Space Telescope (NGST) and the Space Interferometry Mission (SIM).

### The Next Generation Space Telescope

The Next Generation Space Telescope (NGST) is planned for launch in 2009 to accomplish the first two science goals of the Origins Program[1]. NGST's wavelength of interest is in the infrared region of the electromagnetic spectrum, in the range 0.6 to 20 μm. NGST will be able to see objects 400 times fainter than the ground based observatories (Keck Observatory, Gemini Project) and current space based observatories. To achieve this visibility, NGST's angular resolution must be comparable to that of the Hubble Space Telescope (HST)[2].

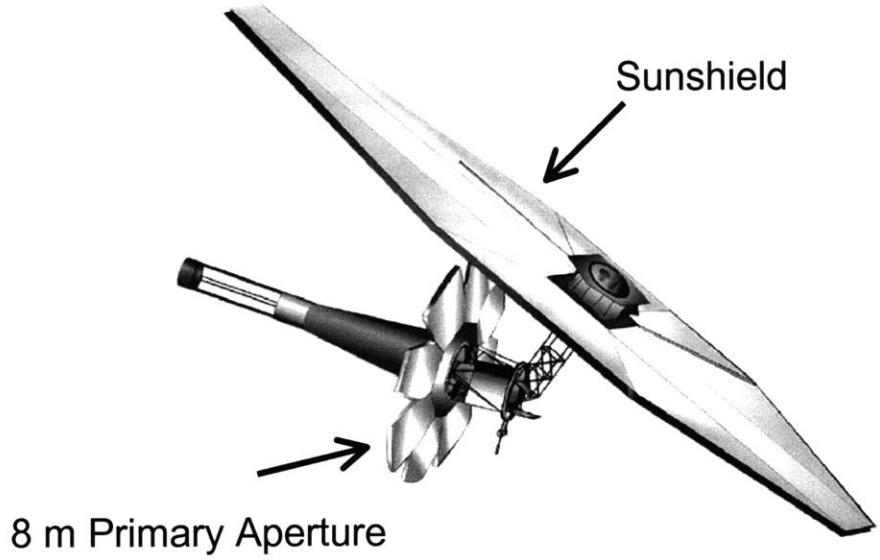


**Figure 1.3** Next Generation Space Telescope - GSFC Design[a]

a. http://www.ngst.nasa.gov

1. http://www.ngst.nasa.gov
2. http://www.ngst.nasa.gov/science/Goals.html

Angular resolution refers to the size of the smallest discernible detail of an image. It is often given in terms of the angle that an object subtends rather than the actual size of the object. A penny at seven feet away from your eye subtends approximately the same angle, half a degree, as the moon in the night sky. The penny 24 miles away subtends an angle of 0.1 arc-seconds, which is the resolution of HST. The angular resolution of a telescope is proportional to the aperture area and inversely proportional to the wavelength of light. Therefore, for a fixed aperture size, resolution is higher at shorter wavelengths, and for a fixed wavelength, resolution improves as the aperture increases. Since NGST is intended to observe at longer wavelengths than HST, its aperture area must be larger to achieve the same angular resolution as HST.

NGST's primary mirror is 8 meters in diameter, almost four times the size that of HST. However, a solid 8m diameter mirror cannot fit into any existing launch vehicle fairings and it would be extremely heavy and costly to launch. One solution to these constraints is a deployable, light-weight 8m diameter mirror. Therefore, the primary mirror used for NGST must be deployable.

Another requirement of designing an infrared telescope to detect faint objects is that the thermal background (heat) must be smaller than the signal it is trying to detect. For NGST to reach its designed operating temperature of 35 degrees Kelvin, it must be removed from large sources of heat. The first source, Earth and the heat of the sun reflected off of Earth, is reduced by launching the satellite far from Earth at the L2 libration point. Once in orbit, the sun is the primary source of heat impinging on the telescope. To shield the optics from the heat, a large sunshield, approximately the size of a tennis court is required.[1] (Figure 1.3) The sunshield adds a large flexible appendage to the spacecraft that adds low frequency modes to the telescope dynamics.

1. [http://origins.jpl.nasa.gov/technology/ultra-lightweight.html]

### Space Interferometry Mission

The Space Interferometry Mission (SIM) planned for launch in 2006, is the first space-based interferometer. Its goals are to perform precision astrometry and demonstrate interferometry technology for future missions, such as TPF. Interferometers combine light from multiple apertures and create a single image with higher resolution than either aperture could produce alone. The angular resolution of the interferometer is determined by the distance between the apertures, rather than by the individual aperture size. Therefore, interferometers provide increased angular resolution without significant increase in mirror mass, cost, and size [DeYoung, 1998].

SIM, shown in Figure 1.4, is a 10m baseline Michelson interferometer. The baseline is the distance between the two apertures perpendicular to the incoming science light. SIM will be able to measure the angular position of stars to an accuracy of 4 microarcseconds, which is several hundred times more accurate than any previous telescope. The resolution provided by SIM will result in improved planet detection, with the ability to detect smaller planets closer to its parent star.

The main structure in Figure 1.4 is a lightweight, flexible truss that supports the light-collecting apertures. The metrology boom and the solar panels are also flexible structures. The optics on SIM are meters apart, yet their relative positions must be controlled to sub-nanometer level precision in order for the interferometer to achieve its astrometry goals.

## 1.1.2 Space Telescope Stringent Performances

Both NGST and SIM share a common goal of improved angular resolution. However, although the trend for improving telescope performance is towards larger aperture telescopes, the design solution of merely increasing the mirror size is limited by existent astronautical technology. The aperture size must be increased by innovative methods such as those mentioned for NGST and SIM: lightweight optics and interferometry. The challenge associated with these designs is the reduction of structural rigidity compared to designs like HST. Lightweight materials are less stiff than glass and subject to deforma-

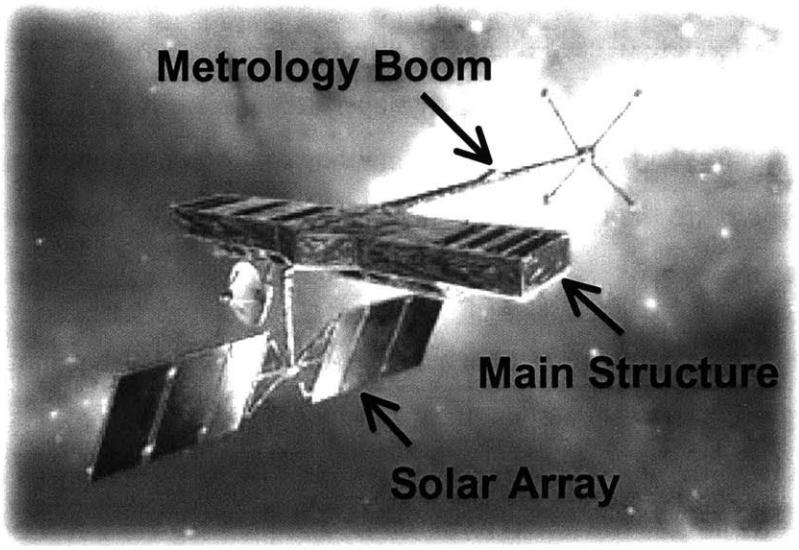


**Figure 1.4** Space Interferometry Mission

tion and vibrations. Deployable truss structures are also more flexible and add low frequency modes to the system. These effects must be taken into consideration when designing the telescope, to ensure that the vibrations attenuated by the structural flexibilities can be adequately damped or isolated from the optical components.

The optics demand extremely quiet, vibration-free environments. The surface of each mirror must hold its shape to fractions of the wavelength of the science light in order to reduce wavefront error. The wavefront consists of light that left the science target at the same time. Because the star is much further away than the dimensions of the telescope, the wavefront entering the telescope is considered planar; however, as it bounces off one mirror to the next, if the surface of the mirror is not a perfect ellipsoid, each ray of light will travel a slightly different distance than its neighbor. Thus, the wavefront will deviate from a perfect plane. For glass mirrors, the surface can be polished and manufactured to be as smooth as required. For example, the largest deviation of the surface of the Chandra X-ray telescope mirrors, the smoothest mirrors ever produced, is within several atoms.[1] If, to

reduce weight, the telescope mirror is not made out of glass, but a flexible membrane, then the shape must be maintained by means other than structural rigidity.

Motion of mirrors relative to each other also affects telescope performance. In an interferometer, the light gathered from two separate apertures must travel the same distance, or optical path length (OPL) from collectors to combiner to interfere constructively and create an image. Therefore the maximum optical path difference (OPD) allowable is on the order of nanometers.

A telescope with high angular resolution has failed in its mission if it cannot be steadied to look at the target for an adequate length of time for the camera to collect enough light. This deviation from the intended target direction represents the ability of a telescope to stay pointed on its target. Wavefront error, OPD, and pointing are a few possible optical performance metrics.

These optics are mounted to a structure whose purpose is to hold them in the correct configuration as well as support the other subsystems of the spacecraft bus. Again, constrained by mass, cost and launch volume, this structure cannot be as rigid as its ground based counterparts are. Engineers must look for alternative structural designs, whose trend is toward lighter and deployable structures, with the optics, themselves, following the same trend. These light, flexible structures easily transmit vibrational noise, which introduce errors into the optics train and reduce the quality of the image. The solution is either to isolate the optics from the sources of noise and/or to add controllers that will actively eliminate the vibrations to a level that is acceptable for optics performance.

These structural flexibilities are not a problem for the telescope unless a disturbance excites them. When satellites are placed in low earth orbits, they encounter atmospheric drag, gravity gradient or magnetic torques that may move the satellite from its desired attitude. Further from earth, in geosynchronous orbits or beyond, the effects of solar wind are

1. [http://chandra.harvard.edu/about/telescope_system2.html]

predominant and can cause external torquing on the satellite to move it from its desired attitude. To compensate for such disturbances from the orbital environment, reaction wheels are used for attitude control. However, reaction wheels themselves are a source of mechanical disturbances on board the telescope. If the wheel's center of gravity or primary inertial axis is off the axis of rotation, the resulting imbalances cause the vibrations that impact disturbances to the system. Reaction wheels are the largest expected disturbance source on space telescopes. Other possible on board disturbance sources are cryocoolers, guide star sensor noise, digital to analog quantization noise, and solar thermal flux.

## 1.2 Integrated Modeling

Integrated modeling is a methodology that combines the models from different sub-disciplines into one complete input-output system. It is interdisciplinary in nature, but in this thesis, the term will refer to the modeling of high-performance opto-structural plants, which includes the disciplines of structural dynamics, optics, and controls. The precision controlled opto-structural plant captures the essential characteristics of different space telescopes and standardizes the analysis [Basdogan, 1999, Gutierrez, 1999, Melody, 1995, Mosier, 1998a, Robertson, 1997]. Figure 1.5 is an example of an integrated model schematic. The highlighted portion within the dotted lines is the integrated model. The input is unit intensity white noise, d, and the outputs are the performances metrics, z. The blocks within the shaded region are the individual components of the integrated model. The following description of the integrated modeling is based on the work of Homero Gutierrez.

The "Opto-Structural Plant" block in Figure 1.5 represents the structural model of SIM. The model is built using finite element methods and represented in state-space format. The structural model represents the dynamics of the system, and accepts forces, f, as input and outputs the states, x, of the system as shown in Figure 1.6.

Performance metrics are use to determine if the telescope meets the engineering requirements, thereby accomplishing its science objectives. Two examples of performances are shown in Figure 1.5: OPD and pointing. The OPD metric is shown as the RMS of the time

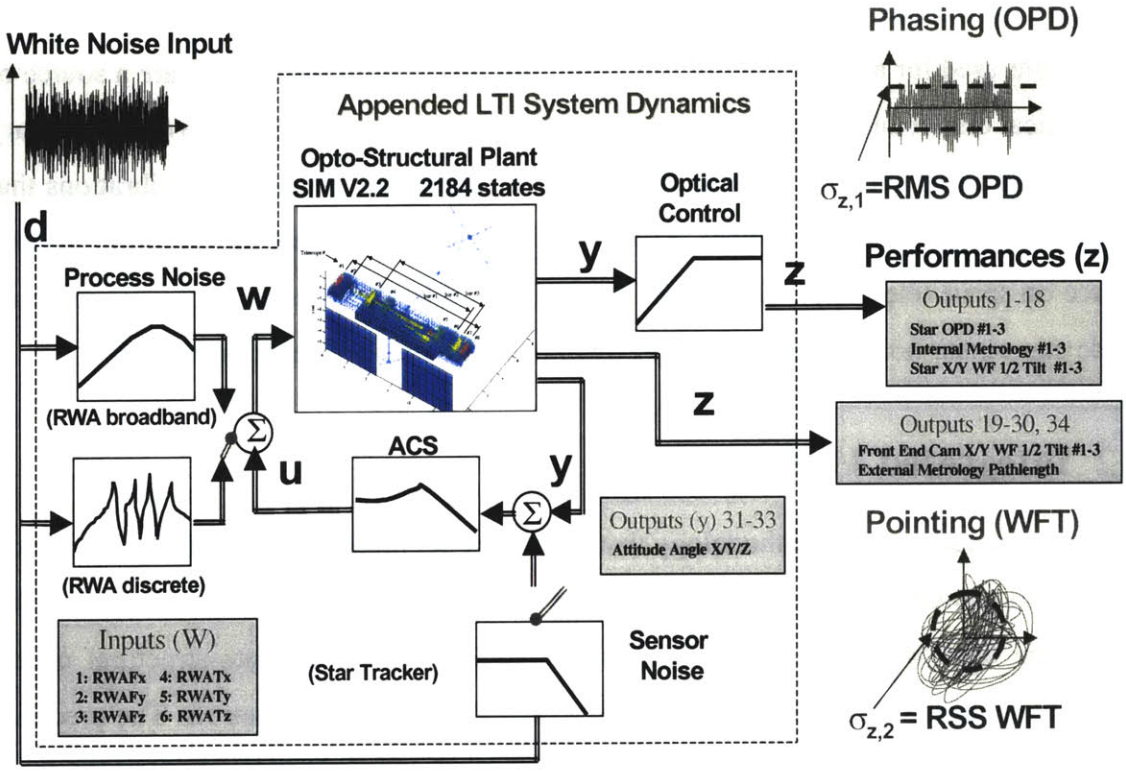


**Figure 1.5** Example Integrated Model: SIM

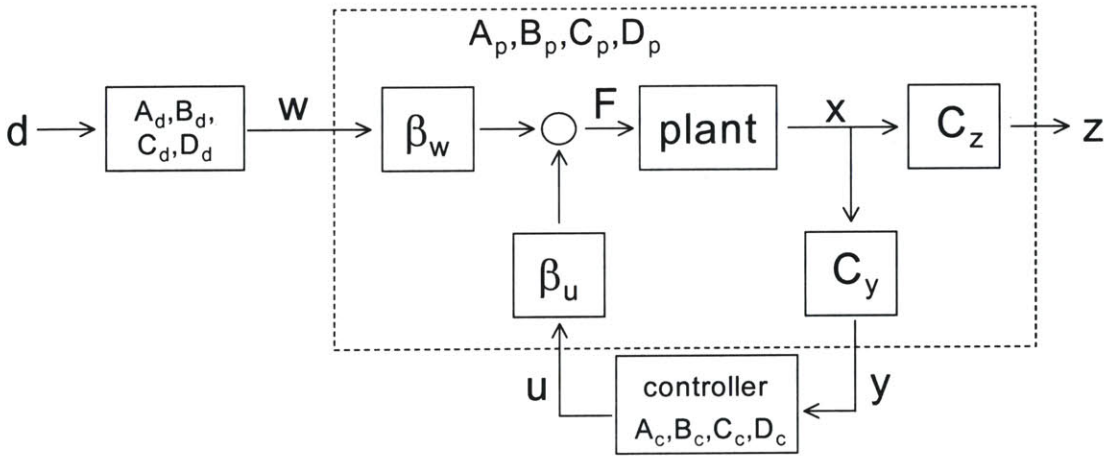


**Figure 1.6** block diagram representation of precision controlled opto-structural integrated model

history. The pointing error, or wavefront tilt (WFT) is given by the root sum squared (rss) of the radius of the time history. The pointing time history information is shown projected on the plane of the telescope's receiver.

The performance block, $C_z$, is not shown in Figure 1.5 because it is modeled in the plant model. The state-space matrix that is represents linearly combines the system states, x, to produce the output metric(s), z. Calculating space telescopes performance metrics requires creating a sensitivity matrix from the plant states to the performance metrics. Calculating these sensitivities require structural engineers and optical engineers to fuse their models together.

In Figure 1.6, w is the disturbance force and the block, $\beta_w$, represents the state-space matrix that maps the disturbances onto the appropriate degrees of freedom in the structural model. This block is also not shown in Figure 1.5, because it, too, is contained within the plant model.

The disturbances can be input into the structural model as a white noise shaping filter. The disturbance filter has its own states and state-space representation as shown in Figure 1.6, where d is the white noise input and w is the shaped disturbances. Modeling the disturbances involves either determining the time histories or creating the state-space filter or both. The subscripts d and p denote the disturbance verses the plant state space matrices, respectively.

If the plant does not meet the performance requirements in the presence of disturbances, a controller may be used to improve the system performance. In Figure 1.6, output y is input to the controller and the controller output, u, drives the plant. All blocks except the controller are part of the plant's state space representation as indicated by the dotted line. The complete integrated model has the state-space formulation of the plant dynamics, disturbance filter and the controller.

## 1.3 Thesis Objective

### 1.3.1 Importance of Accurate Structural Models

Section 1.1.1 and Section 1.1.2 introduced the difficulty of designing space telescopes to achieve the science goals of the Origins Program. The term nanodynamics appropriately implies the degree of precision to which the structures must be controlled.

The fundamental reason why analytical models are used to predict the capabilities of the design is because some structures can not be built for testing; also, the environment the system is being designed for cannot be adequately reproduced [Moses, 1998]. At the conceptual design stage, multiple architectures are compared to determine the direction for future development. Once an architecture is chosen, a number of design iterations are performed before the actual spacecraft is built and deployed. The performance must be able to be predicted through structural analysis to assess the design without building the structure at each iteration. Analytical modeling provides major cost and time savings by doing as much analysis on computers as possible instead of experimentally.

Besides time and cost savings, some telescopes are impractical to build for ground testing. NGST's sunshield, approximately the size of a tennis court, is an example of the trend in future designs towards increasingly larger spacecraft. Though individual subsystem prototypes are built for testing, the size of the complete spacecraft limits the practicality of integrating the entire structure on the ground. Space structures are also designed for operation in a zero-g environment, and may not be able to support their own weight on the ground.

Without ground test verification, the analytical model must accurately capture the dynamic behavior of the structure in order to have confidence in the performance predictions. Early in the project, however, the design is not fully complete when analysis starts and key design decisions are made. It is important to know what information from the low fidelity models can be used to make these critical decisions.

### 1.3.2 Model Fidelity

The accuracy of a model can only be as good as the maturity of the design it is based upon. The maturity of the design refers to how well the iteration represents the final version. If the iteration is in the conceptual design stage, analysis will not accurately reflect the characteristics of the finished product. If the iteration is near final, then its model will still not reflect the actual behavior of the "true" system, but will have less error than the low iteration model and the dynamics will more closely resemble the actual behavior of the final system. If the iterations are complete and the structure is being built or is built, then its model will represent the behavior of the system only to the uncertainty that is within the model itself and not due to uncertainties in the design [Berman, 1999]. Hence, as the design iterates and stabilizes towards the final solution, the fidelity of the model improves and becomes more reliable for predicting performance. In studying model fidelity, it is important to understand how the behavior of low fidelity models resemble the truth model.

Low fidelity designs occur at the beginning of the design process, when a mission concept and architecture are chosen. The design requirements are determined based on a flow down from the science requirements. For example, a maximum OPD RMS determined necessary for mission success is used to determine the extent that the structure must be made rigid, isolated, or controlled. At this stage, only a basic overview of the structure is known with general dimensions in order to keep the optics it its nominal positions.

From the different possible architectures to satisfy the requirements, one approach is chosen that satisfies the cost, requirements and constraints. As the design progresses, more subsystem requirements are determined, dimensions of components and materials are chosen, and a more detailed layout of the structure is created. Fidelity increases further in the design process when the design becomes fixed and most dimensions and material properties are known.

To understand the errors associated with model fidelity, an analogy can be made between the model evolution of a design in progress and the model updating evolution of an exist-

ing structure. This analogy is helpful because model updating is a well-researched topic; there is ample material on the errors associated with fidelity error of the model of a single design iteration [Berman, 1999]. Joshi et al. discuss model fidelity in the sense of model updating, where the increasing fidelity models are the increasingly accurate models of the same built structure [Joshi, 1997].

The updating process begins with a model based on simplifying assumptions and nominal material properties gathered from look-up tables. The model improves as the assumptions are checked for accurate representation of the structure's behavior and as parameter values are tested [Glease, 1994]. The model evolution of the design in progress undergoes a similar process, assuming that the models compared at each iteration have been updated. These models are based on a design that has simplifying assumptions and lack of parameter value knowledge. As the design evolves, the assumptions are solidified and the parameter choices are made. Thus there is a local model evolution within model updating and a global model fidelity evolution as a structure is being designed, as illustrated by Figure 1.7.

This analogy can help explain the types of errors involved in model fidelity evolution. As the term "evolution" implies, there is a change in the type of errors associated with the model at the different design stages. In the earlier stages, non-parametric errors predominate. These are errors that cannot be associated by a parameter (mass or stiffness) of a model element, but are akin to a "lack" of a parameter. Early design errors are associated with errors in design assumptions.

In early design stages and for initial models, large structures can be modeled by a simpler element, such as representing a truss by a beam element. This simplified model, called a stick model, saves computational time when conducting analysis. The beam's dynamics will resemble the global, fundamental characteristics of the truss while not requiring as many elements. The beam will not adequately resemble all the characteristics of the truss, but because the parameters, configuration and dimensions are not fixed, the uncertainty in

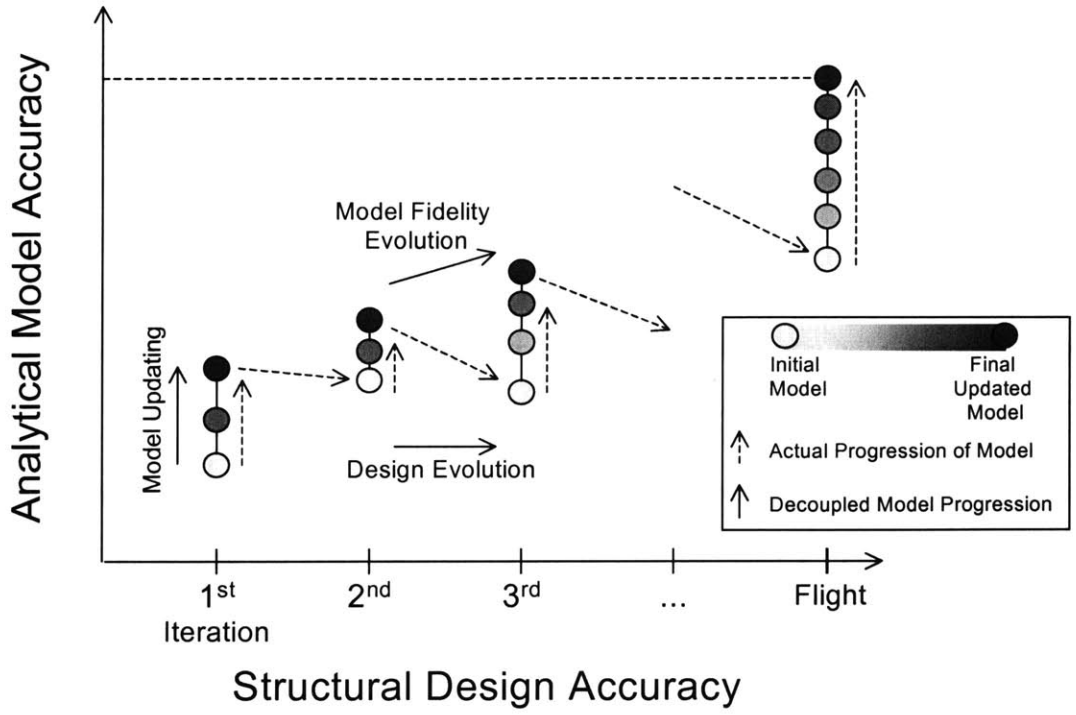


**Figure 1.7** Model Fidelity Evolution

the design is on the same order of magnitude or larger than that associated with the inaccuracies of the stick model.

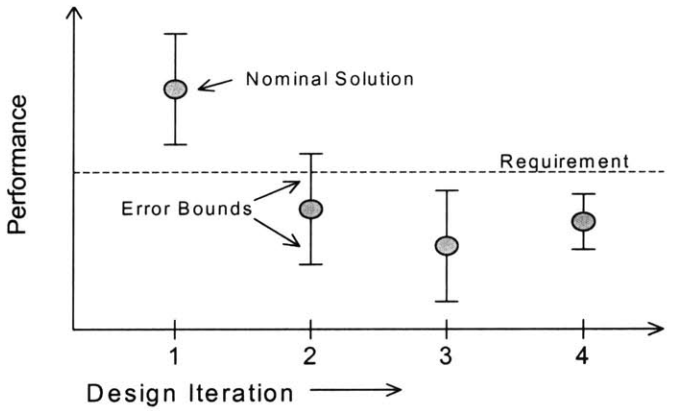


**Figure 1.8** Uncertainty [Gutierrez, 1999]

Figure 1.8 illustrates the performance prediction and error bounds for four design iterations of an imaginary system. The vertical scale in Figure 1.7 can be paralleled with the error bounds of Figure 1.8, where as the error bounds decrease, the analytical model accuracy increases. For Design 1, the performance prediction does not meet the requirement. For Design 2, the design is improved until the nominal solution meets the requirements, but the addition of the error bars shows that the design may or may not meet the requirement. Designs 3 and 4 are two different approaches from Design 2. Design 3 improves the design so that with the uncertainty, the design will meet the requirements. Design 4 does not change the design, but reduces the uncertainty.

Thus there are two ways that the error bars can be defined. The first is with accurate modeling but a low iteration design and the second is with a finalized design but a poor analytical model. Both of these types of error sources can contribute to poor model fidelity. The objective of this thesis is to look at model fidelity evolution compared to model updating to understand how the behavior of low fidelity models resembles the truth model.

## 1.4 Dynamics Optics Controls Structures (DOCS)

The Space Systems Laboratory at MIT has developed a set of software modules and a design and analysis methodology for precision space telescopes called DOCS. DOCS stands for Dynamics Optics Controls Structures and a flowchart for the methodology is shown in Figure 1.9.

The first step in DOCS is modeling all the components of the integrated model. Starting with the design of a telescope, the structure and optics models are created and the disturbance sources are determined and modeled. Since reaction wheels are the primary disturbance source for space telescopes, a lot of work has been done to model their disturbances. Work on reaction wheel modeling has been done by Rebecca Masterson [Masterson, 1999] and Laila Elias [Elias, 2001].

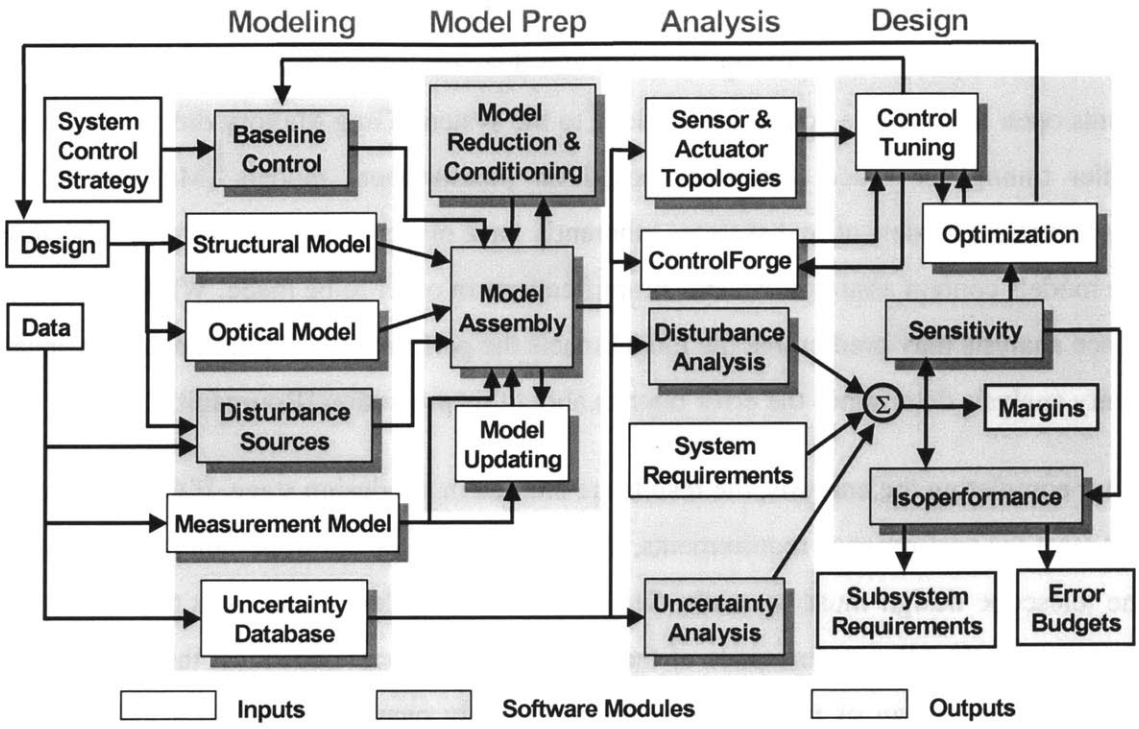


**Figure 1.9** DOCS Flowchart

The individual models are then assembled in the next stage of DOCS. Before being analyzed, however, the model must be updated, conditioned and reduced. The necessity of conditioning is a by-product of using computers to analyze structures. Poor numerical conditioning can cause problems in the analysis not related to the inherent design. For example, if the units of the structure's dimensions are in meters and the performance metrics are in nanometers, the model will be handling two sets of numbers nine orders of magnitude apart. Additionally, the final model can have an extremely large number of degrees of freedom with the addition of the dof's of the disturbance model and the controller. When converted to modal coordinates, not all modes are observable or controllable, and are unnecessary additional information adding to computational expense. Work on conditioning and model reduction has been done by Scott Uebelheart [Uebelhart, 2001].

After preparing the model, it then moves to the next stage, analysis. The fundamental analysis that is done is the disturbance analysis, which will determine if the model will meet

the performance. The disturbance analysis methods used in the Space Systems Lab and in this thesis were developed by Homero Gutierrez [Gutierrez, 1999]. Disturbance analysis can be done open or closed loop. If the model does not satisfy the performance requirements open loop, then a controller is added to the system. Greg Mallory did work on controller tuning for space telescopes based on measurement models [Mallory, 2000a]. Mathematical models of real systems inherently have errors associated with them because the models contain assumptions and simplifications in order to be made. While the disturbance analysis may predict that the model meets the performance requirements, the uncertainty analysis determines the error bounds about this prediction [Bourgault, 2000].

After completing the analysis, the results are studied in the design stage. If the model does not meet the performance requirements, then a change in the controller and/or a change in the telescope design must be made. Sensitivity analysis determines how the changes in parameters affect the performance of the system. If the model does meet the performance requirements, design of the system is not necessarily over. An isoperformance analysis finds multiple sets of design parameters that result in the same performance. This analysis can be important during manufacturing considerations; as some subsystems, like reaction wheels or optical sensors, do not have a continuous array of sizes or quality to choose from parameters traded. Also, improving the performance of one subsystem may be less expensive than improving the performance of another. Work on isoperformance is being done by Olivier de Weck [DeWeck, 1999].

## 1.5 Thesis Overview

Figure 1.10 illustrates how the organization of the chapters in this thesis fits in with the model fidelity evolution diagram of Figure 1.7. First, in Chapter 2 a two-dimensional truss structure is used as an example problem that demonstrates the evolution of a low fidelity "stick" model to a high fidelity "truth" model. Then, in Chapter 3, the Origins Testbed is given as an example of a high fidelity design - a structure that has already been built. The analytical model updating of the testbed is used as a demonstration of the model updating

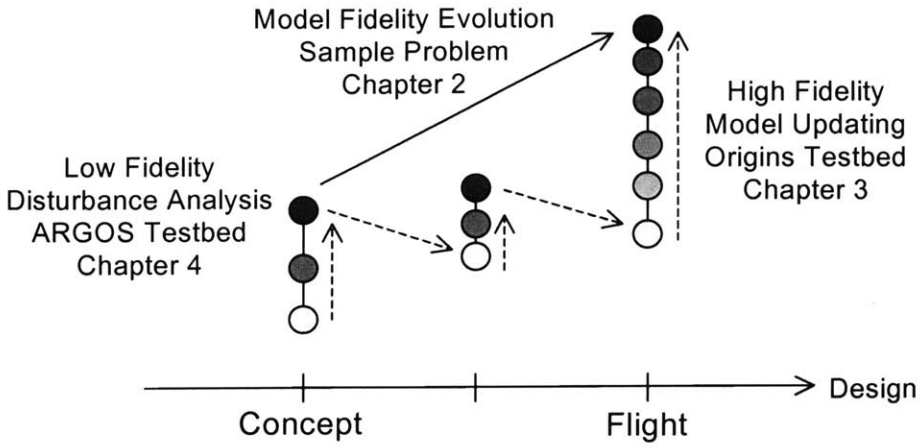


**Figure 1.10** Thesis Roadmap

error analogy to design evolution. In Chapter 4, the ARGOS testbed is described as an example of a low fidelity model. A disturbance analysis is done on ARGOS and conclusions on the analysis are drawn based upon knowledge of ARGOS' model fidelity.

# Chapter 2

# SAMPLE PROBLEM

In this chapter, a truss sample problem is presented to describe the different stages of model fidelity. The design maturity is simulated by different finite element types: (listed in order of increasing fidelity) a Bernoulli-Euler beam, a Timoshenko beam, a truss with rod elements and a truss with bending beam elements. Model updating is simulated by meshing the finite elements at different degrees of refinement. The models are compared to a "truth" model, which is the highly refined truss with bending elements.

## 2.1 State Space Representation

In this section the state space representation of equations of motion in structural modal form is derived. Then the disturbance states are appended to the plant states to create the integrated model. State space representation is first introduced using a simple harmonic oscillator as an example, and is then applied to a discrete multi-degree of freedom system. The 1-dof harmonic oscillator is shown in Figure 2.1, where m is the mass, k is the spring constant, c is the damping coefficient, x is the displacement of the mass and F is the force applied to the mass.

The equation of motion for the mass is given by:

$$m\ddot{x} + c\dot{x} + kx = F \tag{2.1}$$

Then solving for the acceleration of the mass gives:

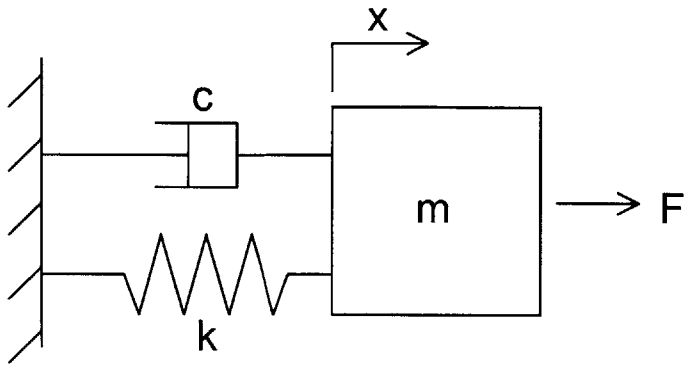


**Figure 2.1** Simple system

$$\ddot{x} = \left(-\frac{c}{m}\right)\dot{x} + \left(-\frac{k}{m}\right)x + \frac{F}{m} \tag{2.2}$$

Two new variables $x_1$ and $x_2$ are defined such that:

$$\begin{aligned} x_1 &\equiv x \\ x_2 &\equiv \dot{x} \end{aligned} \tag{2.3}$$

Written in matrix form, the equation for the time derivatives of the new variables, x1 and x2, using equations (2.2) and (2.3) are:

$$\begin{bmatrix} \dot{x}_1 \\ \dot{x}_2 \end{bmatrix} = \begin{bmatrix} 0 & 1 \\ \left(-\frac{k}{m}\right) & \left(-\frac{c}{m}\right) \end{bmatrix} \begin{bmatrix} x_1 \\ x_2 \end{bmatrix} + \begin{bmatrix} 0 \\ \frac{F}{m} \end{bmatrix} \tag{2.4}$$

The vector, $[x_1, x_2]^T$, contains the states of the system. Equation (2.4) is helpful for visualizing the state space representation since it still retains the physical characteristics of the system. The derivation of the structural modal form for the multi-degree of freedom systems is based on the physics of the structure, but the resulting equations are in modal coordinates, which are less physically intuitive. Notice from equation (2.4) that the number of

states is twice the number of degrees of freedom of the system. This fact always holds when converting to a physically-based state-space representation.

For discrete systems with more than one degree of freedom, the mass and stiffness terms are matrices instead of scalars. The equations of motion of a conservative (undamped), linear, time invariant (LTI) system can be written as:

$$\mathbf{M}\ddot{\mathbf{x}} + \mathbf{K}\mathbf{x} = \mathbf{F} \tag{2.5}$$

where $\mathbf{M}$ and $\mathbf{K}$ are the $(n \times n)$ mass and stiffness matrices, respectively, $\mathbf{x}$ is a vector of the n degrees of freedom (DOF) in the physical coordinate system, and $\mathbf{F}$ is a vector of external forces acting on the system.

Assuming that the homogenous solution of equation (2.5) is of the form:

$$\mathbf{x} = \phi e^{j\omega t} \tag{2.6}$$

and substituting this solution into equation (2.5) while setting $\mathbf{F} = 0$, we obtain:

$$-\omega^2\mathbf{M}\phi + \mathbf{K}\phi = \mathbf{0} \tag{2.7}$$

Then, by substituting $\omega^2 \equiv \lambda$ and rearranging, we obtain the generalized eigenvalue problem:

$$(\mathbf{K} - \lambda_i\mathbf{M})\phi_i = 0 \tag{2.8}$$

where $\lambda_i$ is the $i^{th}$ eigenvalue and $\phi_i$ is the corresponding eigenvector. The index, i, ranges from i = 1...m, where m is the number of modes of the system, $(m \leq n)$. In general, the total number of modes is equal to the number of DOF, but it is not always necessary to include all modes in the model. For instance, when using finite element methods, the higher modes are often neglected. They inherently have high error due to the linearization of finite elements and they add to the computational expense for large models. Additionally, if the analytical model is compared to data, the higher modes may exceed the frequency of the data and are then unnecessary information.

Due to the orthogonality of the eigenvectors, the following relationships hold:

$$
\begin{aligned}
{}^0\Phi^T \mathbf{M}\, {}^0\Phi &= \mathbf{I} \\
{}^0\Phi^T \mathbf{K}\, {}^0\Phi &= \begin{bmatrix} \backslash & & \\ & \omega_i^2 & \\ & & \backslash \end{bmatrix} = \Omega^2
\end{aligned}
\tag{2.9}
$$

where $\Phi$ is the $(n \times m)$ eigenvector matrix. The superscript, 0, indicates that ${}^0\Phi$ is mass normalized. The columns of ${}^0\Phi$ are the eigenvectors $\phi_1$, $\phi_2$, $\phi_3$,..., $\phi_m$, I is the identity matrix, and $\Omega^2$ is a diagonal matrix whose elements are the eigenvalues $\lambda_1 = \omega_1{}^2$, $\lambda_2 = \omega_2{}^2$, $\lambda_3 = \omega_3{}^2$, ... , $\lambda_m = \omega_m{}^2$.

Using equation (2.9), equation (2.5) can be decoupled through a coordinate transformation from physical to modal coordinates. Substituting:

$$\mathbf{x} = {}^0\Phi\xi \tag{2.10}$$

into the equation of motion we obtain:

$$\mathbf{M}\,{}^0\Phi\ddot{\xi} + \mathbf{K}\,{}^0\Phi\xi = \mathbf{F} \tag{2.11}$$

where $\xi$ is the vector of modal coordinates.

Pre-multiplying equation (2.11) by ${}^0\Phi^T$ gives:

$${}^0\Phi^T\mathbf{M}\,{}^0\Phi\ddot{\xi} + {}^0\Phi^T\mathbf{K}\,{}^0\Phi\xi = {}^0\Phi^T\mathbf{F} \tag{2.12}$$

Then using equations (2.9) and (2.11), we rewrite equation (2.12) as:

$$\ddot{\xi} + \Omega^2\xi = \mathbf{Q} \tag{2.13}$$

At this stage we add damping back to the system by assuming that the damping is proportional to the modes. This assumption is valid for lightly damped systems:

$$\ddot{\xi} + 2\mathbf{Z}\Omega\dot{\xi} + \Omega^2\xi = \mathbf{Q} \tag{2.14}$$

where **Z** is the diagonal matrix of damping coefficients.

The forcing term is partitioned into two components: forces from disturbances, $F_w$, and forces from control actuators, $F_u$:

$$\mathbf{Q} = {}^0\Phi^T\mathbf{F} = {}^0\Phi^T\mathbf{F}_u + {}^0\Phi^T\mathbf{F}_w = {}^0\Phi^T\beta_u\mathbf{u} + {}^0\Phi^T\beta_w\mathbf{w} \tag{2.15}$$

where the $(n \times n_u)$ matrix, $\beta_u$, and $(n \times n_w)$ matrix, $\beta_w$, map the actuator forces and disturbances, respectively, onto the correct degrees of freedom, $n_u$ are the number of actuator inputs and $n_w$ are the number of disturbance inputs. The ${}^0\Phi^T$ matrix completes the coordinate transformation so that the actuator forces and disturbances act on the correct modal coordinates. Substituting into equation (2.14) and rearranging we have:

$$\ddot{\xi} = -2\mathbf{Z}\Omega\dot{\xi} - \Omega^2\xi + {}^0\Phi^T\beta_u\mathbf{u} + {}^0\Phi^T\beta_w\mathbf{w} \tag{2.16}$$

Equation (2.16) is the equation of motion in the modal coordinate system. It is rearranged as a system of equations and written in matrix form by defining a new state variable:

$$\mathbf{q}_p \equiv \begin{bmatrix} \xi \\ \dot{\xi} \end{bmatrix} \tag{2.17}$$

Then the equations of motion in state-space form are:

$$\dot{\mathbf{q}}_p = \underbrace{\begin{bmatrix} 0 & \mathbf{I} \\ -\Omega^2 & -2\mathbf{Z}\Omega \end{bmatrix}}_{\mathbf{A}_{(2m\times 2m)}}\mathbf{q}_p + \underbrace{\begin{bmatrix} 0 \\ {}^0\Phi^T\beta_u \end{bmatrix}}_{\mathbf{B}_{u\,(2m\times n_u)}}\mathbf{u} + \underbrace{\begin{bmatrix} 0 \\ {}^0\Phi^T\beta_w \end{bmatrix}}_{\mathbf{B}_{w\,(2m\times n_w)}}\mathbf{w} \tag{2.18}$$

where **A** is the plant dynamics matrix, m is the number of modes retained $\mathbf{B}_u$ is the plant actuation input matrix, $n_u$ is the number of controller inputs, $\mathbf{B}_w$ is the plant disturbance input matrix, $n_w$ is the number of disturbance inputs.

Equation (2.18) is written in the structural-modal form. This form is most useful when the mass and stiffness matrices are unknown, but the eigenvalues and eigenvectors are known.

To complete the state space representation, the output is written as a combination of the state variables:

$$\mathbf{y} = \mathbf{C}\mathbf{x} + \mathbf{D}_{yu}\mathbf{u} + \mathbf{D}_{yw}\mathbf{w} \tag{2.19}$$

where C maps the correct degrees of freedom to the output. To transform to modal coordinates, $\mathbf{x} = {}^{0}\Phi\xi$ is substituted in equation (2.19). To rewrite equation (2.19) in matrix form, $\xi$ and $\dot{\xi}$ are factored out and replaced by $\mathbf{q}_p$ to obtain:

$$\mathbf{y}=\underbrace{\left[\mathbf{C}_{yx}\,{}^{0}\Phi \;\; \mathbf{C}_{y\dot{x}}\,{}^{0}\Phi\right]}_{\mathbf{C}_{y(n_y\times 2m)}}\mathbf{q}_p+\underbrace{\left[\mathbf{D}_{yu}\right]}_{\mathbf{D}_{yu(n_y\times n_u)}}\mathbf{u}+\underbrace{\left[\mathbf{D}_{yw}\right]}_{\mathbf{D}_{yw(n_y\times n_w)}}\mathbf{w} \tag{2.20}$$

where $\mathbf{C}_y$ is the plant output matrix and $n_y$ is the number of outputs. The matrices $\mathbf{D}_{yu}$ and $\mathbf{D}_{yw}$ are the feedthrough matrices from the control forces and disturbances, respectively, to the output and are usually zero.

Similarly, the performance can be written:

$$\mathbf{z}=\underbrace{\left[\mathbf{C}_{zx}\,{}^{0}\Phi \;\; \mathbf{C}_{z\dot{x}}\,{}^{0}\Phi\right]}_{\mathbf{C}_{z(n_z\times 2m)}}\mathbf{q}_p+\underbrace{\left[\mathbf{D}_{zu}\right]}_{\mathbf{D}_{zu(n_z\times n_u)}}\mathbf{u}+\underbrace{\left[\mathbf{D}_{zw}\right]}_{\mathbf{D}_{zw(n_z\times n_u)}}\mathbf{w} \tag{2.21}$$

where $\mathbf{C}_z$ is the performance matrix, and $n_z$ is the number of performances. The matrices $\mathbf{D}_{zu}$ and $\mathbf{D}_{zw}$ are the feedthrough matrices from the control forces and disturbances, respectively, to the performance and are usually zero. The difference between y and z is that the outputs, y, are the sensor measurements used by controllers for calculating actuator control signals and the performances, z, are the metrics used to determine if the plant is meeting requirements.

The complete state space system for the plant is thus written:

$$\begin{aligned} \dot{\mathbf{q}}_p &= \mathbf{A}_p\mathbf{q}_p + \mathbf{B}_u\mathbf{u} + \mathbf{B}_w\mathbf{w} \\ \mathbf{y} &= \mathbf{C}_y\mathbf{q}_p + \mathbf{D}_{yu}\mathbf{u} + \mathbf{D}_{yw}\mathbf{w} \\ \mathbf{z} &= \mathbf{C}_z\mathbf{q}_p + \mathbf{D}_{zu}\mathbf{u} + \mathbf{D}_{zw}\mathbf{w} \end{aligned} \tag{2.22}$$

A state-space model can be derived through an analytical model of the M and K matrices. If the structure being modeled has already been built, then the analytical model can be compared to the experimental data. Noise is input at the correct location and data are taken from sensors at the output nodes. A set of A,B,C,D matrices is then found that best fits the system ID transfer function. This model is called the measurement model and is assumed to be a more accurate representation of the plant dynamics than the analytical model [Marco-Gomez,1999]. Unfortunately, the measurement model is not created based on relationships among physical parameters and, therefore, must be recalculated anytime the structure or environmental conditions change.

**Disturbance states:**

As described in Section 1.2, disturbance can be modeled as a state space filter through which unit intensity white noise is shaped to produce a Power Spectral Density (PSD) with the equivalent energy and frequency content as the actual PSD of the disturbance.

The disturbance represented in state space form is denoted by a subscript d:

$$\begin{aligned} \dot{\mathbf{q}}_d &= \mathbf{A}_d\mathbf{q}_d + \mathbf{B}_d\mathbf{d} \\ \mathbf{w} &= \mathbf{C}_d\mathbf{q}_d \end{aligned} \tag{2.23}$$

where $\mathbf{q}_d$ are the disturbance states, $\mathbf{d}$ is the white noise input, and $\mathbf{w}$ is the shaped disturbance output.

A new state vector is created by appending the disturbance states to the plant states:

$$\mathbf{q} = \begin{bmatrix} \mathbf{q}_d \\ \mathbf{q}_p \end{bmatrix} \tag{2.24}$$

and the system equations are:

$$\dot{\mathbf{q}} = \begin{bmatrix} \mathbf{A}_d & 0 \\ \mathbf{B}_w\mathbf{C}_d & \mathbf{A}_p \end{bmatrix}\mathbf{q} + \begin{bmatrix} \mathbf{B}_d \\ 0 \end{bmatrix}\mathbf{d}$$
$$\mathbf{z} = \begin{bmatrix} 0 & \mathbf{C}_z \end{bmatrix}\mathbf{q} + \begin{bmatrix} 0 \end{bmatrix}\mathbf{d} \tag{2.25}$$

where d is the white noise input and z is the performance output.

## 2.2 Problem Formulation

A simple truss is used as a sample problem to illustrate the evolution of model fidelity, which is the increase in the accuracy of the model as the design iterates to the true system. The initial design is a simple beam and the final design is a beam-like truss. To adequately compare the low fidelity beam-type model with the high fidelity truss model, the beam is forced to have properties equivalent to the final truss design. In an actual design scenario, where the final design is not known a priori, the initial design will include parametric errors in addition to the non-parametric errors discussed in this section.

In this example, model fidelity evolution is demonstrated through the use of different finite elements and by refinement of the finite element mesh. The truss is first represented as a stick model with Bernoulli-Euler beam elements and then with Timoshenko beam elements. The next step in the model evolution is to accurately model the truss geometry. However, the truss is first modeled using rod members which only have forces and displacements in each member's axial direction. Finally, the members are modeled as bending members. A highly refined model of the truss with bending members is considered the "truth" model against which to compare the others.

The type of finite element determines the modes that are modeled. The stick models only capture the global modes of the truss and not the effects of the flexibility of the individual truss members. Because the truss has a low aspect ratio (length/depth) the Timoshenko beam captures the truss' global bending modes at a significantly higher accuracy than the

Bernoulli-Euler beam. A truss modeled with rods does not capture the local bending modes of the members, but captures the stiffness characteristics of the truss more accurately than the beam elements. Finite element mesh refinement increases the number of modes calculated and allows the lower-frequency modes to converge to the continuous solution.

The truss consists of eight square bays with alternating diagonals across each face. It is fixed at one end, x = 0, and free at the other, x = L. The members of the truss are circular beams of radius r. The horizontal and vertical members have length ($L_m = L/8$) and the diagonal members have length $\sqrt{2}L_m$. The nodes are labeled across the top from left to right then across the bottom from left to right. A downward force is applied to the top of the truss at node 6, and the performance is the truss tip displacement as shown in Figure 2.2. The truss configuration and property values resemble one face of the three dimensional truss tower of the Origins Testbed. However the total length was fixed to 1m for numerical simplicity. The property values are listed in Table 2.1.

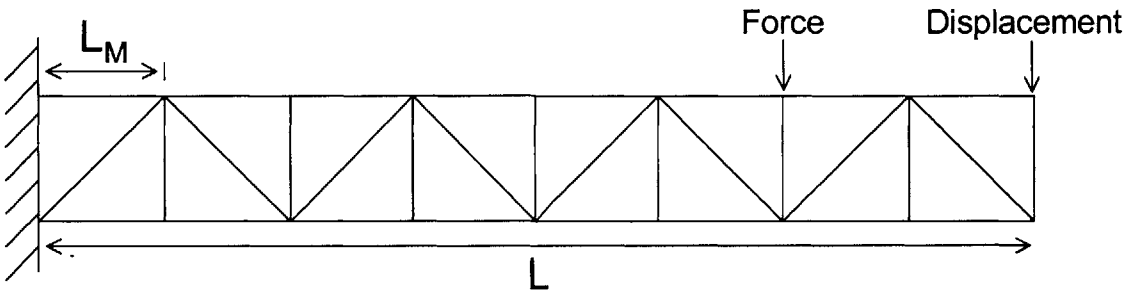


**Figure 2.2** Example problem truss schematic

## 2.2.1 Equivalent Inertia

An advantage of modeling a truss with a stick model is the reduction of the number of degrees of freedom and thus the reduction of the size of the model and computational time. However, to accurately represent the truss as a beam, the stick model must have similar fundamental characteristics, such as static deflection (static similarity) and/or funda-

**TABLE 2.1** Truss property values

| Variable | value |
|---|---|
| material | AL |
| E | 7.2E-10 Pa |
| $\nu$ | 0.33 |
| $\rho$ | 2800 kg/m$^3$ |
| L | 1 m |
| $L_m$ | 0.125 m |
| r | 0.004 m |

mental mode(s) (dynamic similarity). A simple analysis of the truss is deformed to determine the equivalent beam properties. Then the beam is used for analysis of the larger system.

Sun et al. present a method to find the equivalent properties for a truss [Sun, 1981]. The authors solve for the three equivalent beam stiffnesses: e.g. axial stiffness (EA), bending stiffness (EI), and shear stiffness (GA) assuming that these properties are decoupled. Necib et al. discusses how to calculate the entire matrix of coupled stiffnesses as well, which is important for asymmetrical structures [Necib, 1989]. The decoupled stiffnesses will be used for the sample problem. The equivalent inertia properties of the truss are the mass per unit length ($\rho$A) and the rotary inertia per unit length ($\rho$I) and their calculations are also presented by Sun et al.

Because equivalent beam properties are calculated via static deflections of the truss, the following derivation is for a simple, static truss using ideal truss assumptions: members experience only compression and tension [Strang, 1986]. Each node has two degrees of freedom as shown in Figure 2.3. There are eighteen nodes and 33 members.

The vector, **x**, is a vector of unknown displacements at each node, where superscripts H and V specify horizontal and vertical displacement, respectively:

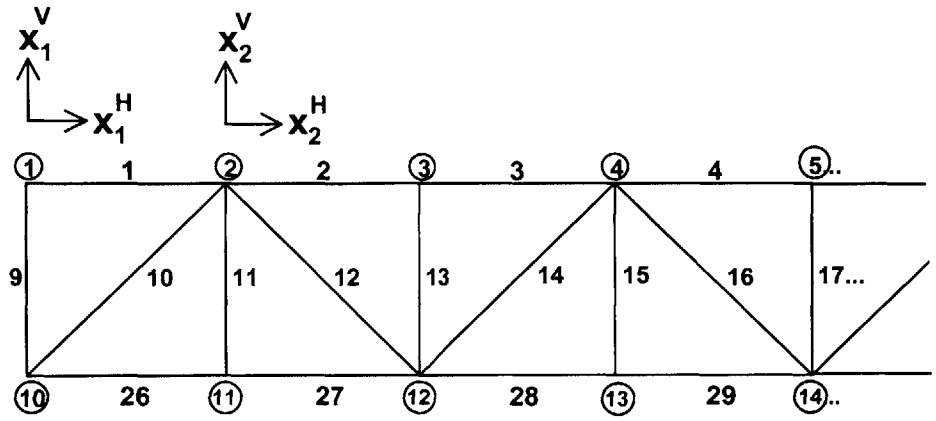


**Figure 2.3** Labeling of the truss (left four bays shown)

$$\mathbf{x} = \begin{bmatrix} x_1^H & x_1^V & x_2^H & x_2^V & \cdots & x_{18}^V \end{bmatrix}^T \tag{2.26}$$

The vector, **e**, is a vector of elongations, where $e_i$ is the elongation of the $i^{th}$ member:

$$\mathbf{e} = \begin{bmatrix} e_1 & e_2 & e_3 & \cdots & e_i & \cdots & e_{33} \end{bmatrix} \tag{2.27}$$

The elongations are calculated via the geometry of the truss. The following is an example of the equation for the elongations of members 2 and 14:

$$\begin{aligned} e_2 &= x_3^H - x_2^H \\ e_{14} &= \frac{1}{\sqrt{2}} x_4^H - \frac{1}{\sqrt{2}} x_{12}^H + \frac{1}{\sqrt{2}} x_4^V - \frac{1}{\sqrt{2}} x_{12}^V \end{aligned} \tag{2.28}$$

The set of equations for **e** is written in matrix form such that:

$$\mathbf{e} = \mathbf{A}\mathbf{x} \tag{2.29}$$

where **A** is the $(m \times n)$ incidence matrix, m is the number of members and n is the number of nodes. The internal force in member i, $y_i$, is determined via the beam constitutive equation:

$$y_i = c_i e_i$$
$$c_i = \frac{E_i A_i}{L_i} \tag{2.30}$$

where $E_i$ is the modulus of elasticity of the $i^{th}$ member, $A_i$ is the cross-sectional area and $L_i$ is the length of the member. The product, $E_i A_i$, is the axial stiffness and is the same for all members. Only $L_i$ is different and is 0.125m for the horizontal and vertical members and $\sqrt{2}$*0.125 for the diagonal members.

Equation (2.30) can be written in matrix form

$$\mathbf{y} = \mathbf{Ce} \tag{2.31}$$

where the diagonal matrix, **C**, is formed with the elements, $c_i$, along the diagonal.

Finally, the nodal force, **f**, is the sum of the internal forces from each member connected to the node. The equilibrium equation is written:

$$\mathbf{A}^T\mathbf{y} = \mathbf{f} \tag{2.32}$$

Combining equations (2.29), (2.30), and (2.32), produces a relationship between the nodal forces, **f**, to the displacements, **x**:

$$\mathbf{x} = (\mathbf{A}^T\mathbf{CA})^{-1}\mathbf{f} \tag{2.33}$$

**Axial Stiffness**

To calculate the equivalent axial stiffness, EA, for the truss, constrain the truss such that node 10 is pinned and node 1 is free to move vertically (Figure 2.4). A force of -1N is applied at the right end of the truss by applying 0.5 N at nodes 9 and 18 in the negative $x^H$ direction.

The deflection of the tip nodes as a result of the compressive force is related to the axial stiffness by:

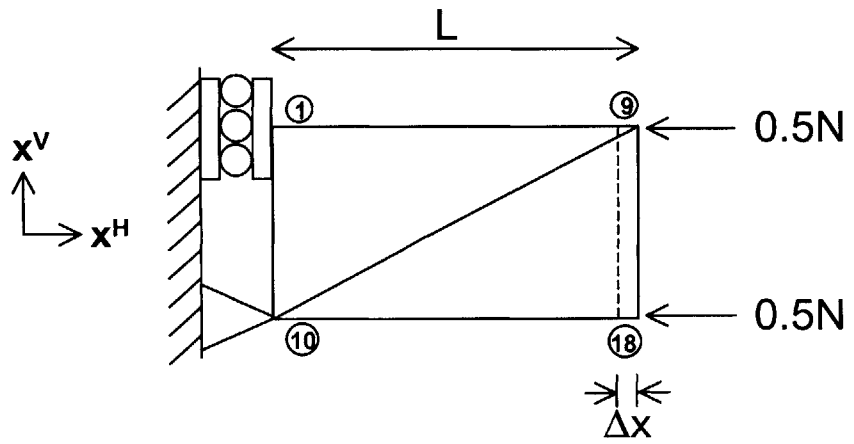


**Figure 2.4** Axial Compression

$$\Delta x = \frac{FL}{EA} \tag{2.34}$$

where F is the applied force, L is the total length, $\Delta x$ is the change in length of the truss, E is the modulus of elasticity and A is the cross-sectional area. The displacement of nodes 9 and 18 are both calculated to be from Equation (2.32) $-1.382 \times 10^{-7}$m, and then Equation (2.34) gives $EA = 7.238 \times 10^{6}$N.

### Bending Stiffness

The bending stiffness, EI, is calculated by decoupling the bending and shear deflections. A moment is applied at the end of the truss and the truss is constrained the same as for the compression test. A force of 1N is applied at node 9 in the positive horizontal direction and a force of 1N is applied to node 18 in the negative horizontal direction to create a bending moment of 0.125Nm (Figure 2.5).

The resulting angular deflection, $\phi$, of the end member is related to the bending moment by:

$$M = F \times L_m = EI\frac{\phi}{L_m} \tag{2.35}$$

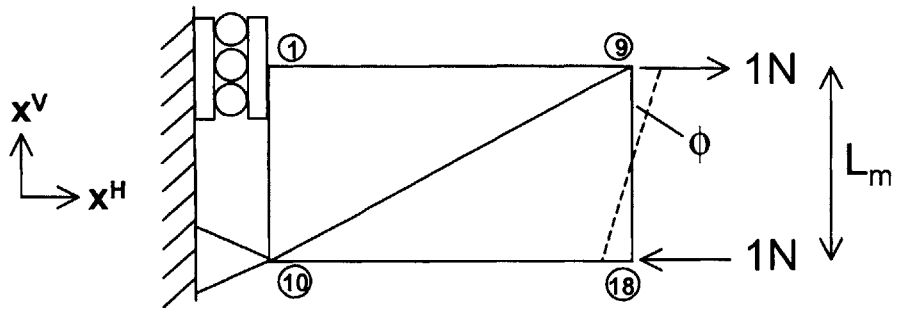


**Figure 2.5** Bending Moment

where M is the moment acting on the beam, $L_m$ is the moment arm, E is the modulus of elasticity, I is the inertia and $\phi$ is the tip angular displacement due to bending. The angle, $\phi$, is assumed to be small. The resulting displacement of node 9 is $x^H = 2.762e\text{-}7$, $x^V = 1.105e\text{-}6$ and node 18 is $x^H = -2.762e\text{-}7$, $x^V = -1.105e\text{-}6$ from Equation (2.33). The resulting bending stiffness calculated from equation (2.35) is $EI = 2.2619 \times 10^5 Nm^2$.

### Shear Stiffness

The shear stiffness, GA, is calculated by applying a shear force of 1N at the end of the truss and constraining nodes 1, 9, 10, and 18 such that the truss cannot bend, but can only deflect due to shear deformation. Node 10 is pinned and nodes 1, 9 and 18 are only free to move vertically (Figure 2.6).

The resulting angular deflection, $\theta$, is related to the shear force by:

$$Q = GA\theta \tag{2.36}$$

where Q is the shear force, G is the shear modulus of elasticity, A is the cross-sectional area, and $\theta$ is the total angular deflection due to the applied force. From Equation (2.33), the vertical displacement of node 9 is calculated to be $1.645 \times 10^{-6}$m, and node 18 is calculated to be $1.610 \times 10^{-6}$m. These two results are averaged to obtain an average displacement and then the equivalent shear stiffness, $GA = 2.6113 \times 10^5$N, from Equation (2.36).

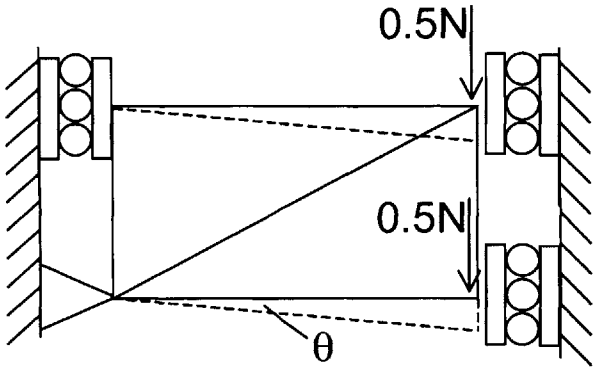


**Figure 2.6** Shear Force

### Mass Per Unit Length

The the mass per unit length for the equivalent beam is given by $m = \rho A$. This term is calculated by dividing the mass of the truss by its total length. The mass of the truss is calculated from the volume of each member ($V_{VH} = \pi r^2 L_m$ or $\pi r^2 \sqrt{2} L_m$), the density of aluminum (2800 kg/m$^3$) and the number of members.

$$\rho A = \frac{n_{HV} \pi r^2 L_{HV} \rho + n_{diag} \pi r^2 L_{diag} \rho}{L} \tag{2.37}$$

where $n_{HV}$ is the number of horizontal and vertical members, $n_{diag}$ is the number of diagonal members, $L_{HV} = L_m$, and $L_{diag} = \sqrt{2} L_m$. The mass per unit length, $\rho A$, for the sample truss is 0.6389 kg/m.

### Rotary Inertia Per Unit Length

Timoshenko beams account for the rotary inertial effects of the beam. The rotary inertia appears in the equations of motion as the product, $\rho I$, which is the inertia per unit length about an axis perpendicular to the plane of the truss through the centerline. The rotary inertia per unit length is equivalent to the rotary inertia about the centerline divided by the total length.

$$\rho I = \frac{n_H \rho A\left(\frac{L_{HV}}{2}\right)^2 + n_V \rho A\frac{(L_{HV}^3)}{12} + n_{diag}\rho A\left(\frac{L_{diag}^3}{12}\right)\left(\frac{L_{HV}}{L_{diag}}\right)^2}{L} \tag{2.38}$$

where $n_H$ is the number of horizontal members, $n_V$ is the number of vertical members, $n_{diag}$ is the number of diagonal members, $L_{HV} = L_m$, and $L_{diag} = \sqrt{2}\,L_m$.

Calculating the inertia about the centerline gives the rotary inertia per unit length because an infinitesimal cross section of the truss (perpendicular to the centerline) has the same inertia when rotated about the point of intersection with the centerline in any direction (Figure 2.7).

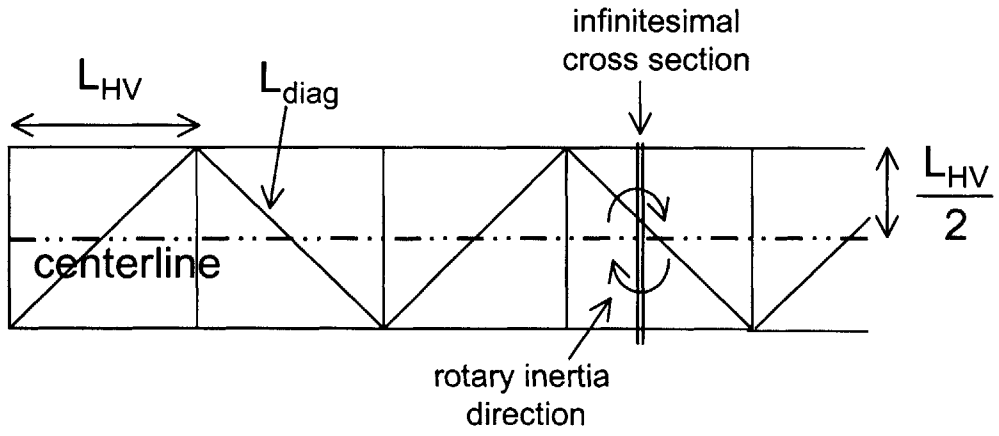


**Figure 2.7** Rotary inertia per unit length is equivalent to the inertia of the truss calculated about the centerline, rotating in and out of the plane divided by the total length

The rotary inertia, ρI, calculated for the truss is 0.0016 kg·m.

### Equivalent Material and Beam Properties

In order to implement the beam model in MSC/NASTRAN, the material properties (E, G and ρ) and the beam properties (A,I) are required individually, not as products (EA, EI, GA, ρA, and ρI). Unfortunately, the five products cannot be used to produce five unique quantities, E, G, ρ, A, and I. If the product EA is dividing by EI to obtain the ratio,

$A/I = EA/EI$, and the same is done for the products $\rho A$ and $\rho I$ to get another value for the ratio, $A/I = \rho A/\rho I$, then these two ratios are equal when calculated for real beams and materials. However, these products were determined by finding equivalent beam properties and they do not equal each other in this example. Because rotary inertia terms are small, the errors from removing the $\rho I$ term should be small [Sun, 1981] and then the rest of the products can be used to find the equivalent material and beam properties. By setting E to be Young's modulus for aluminum ($7.2 \times 10^{10}$Pa), the other four quantities can be solved.

**TABLE 2.2** Equivalent beam properties

| | |
|---|---|
| E | 7.200 e10 Pa |
| G | 2.598 e9 Pa |
| $\rho$ | 6345 kg/m$^3$ |
| A | 1.005 e-4 m$^2$ |
| I | 3.142 e-6 m$^4$ |

## 2.2.2 Continuous Beam Solutions

In this section, the natural frequencies and mode shapes for the Bernoulli-Euler and Timoshenko beams are derived from continuous formulations. These analytical solutions serve as a benchmark against which to compare the effect of refinement of the finite element models on the accuracy of the dynamic predictions.

### Bernoulli-Euler Beam

The Bernoulli-Euler (BE) beam model assumes that rotary inertia and shear deformation are negligible. The continuous model of the Bernoulli-Euler beam is shown in Figure 2.8, where m(x) is the mass per unit length, E(x) is the modulus of elasticity, and I(x) is the inertia of the cross-sectional area, A(x) is the cross-sectional area. All properties are constant with respect to x in this example.

The partial differential equation (PDE) of a Bernoulli-Euler beam is:

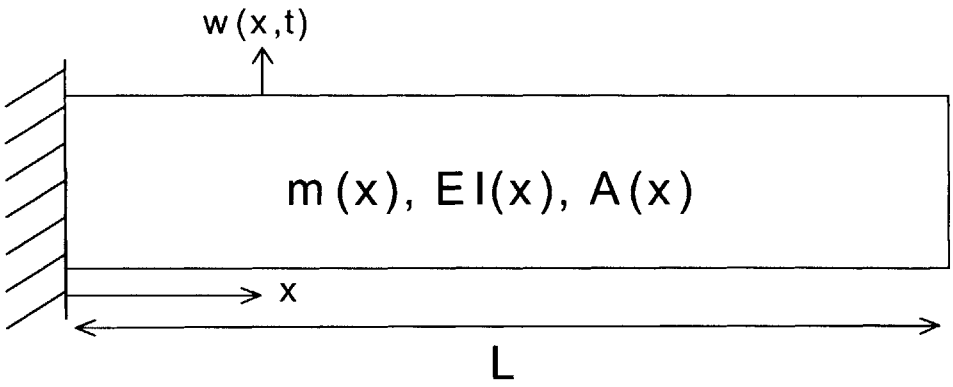


**Figure 2.8** Truss modeled as beam

$$EI\, w^{iv}(x, t) + m\ddot{w} = f(x, t) \tag{2.39}$$

where $(\ )^{iv}$ indicates the fourth derivative with respect to x and $(\ddot{\ })$ indicates the derivative with respect to time. The beam is fixed at x = 0 and free at x = L. The corresponding boundary conditions for this configuration are:

$$\begin{aligned} &\text{at } x = 0 \qquad w(0, t) = 0 \qquad w^{i}(0, t) = 0 \\ &\text{at } x = L \qquad EI\, w^{ii}(L, t) = 0 \qquad EI\, w^{iii}(L, t) = 0 \end{aligned} \tag{2.40}$$

The initial conditions w(x,0) and $\dot{w}(x,0)$ are given. For modal analysis, however, the initial conditions are not necessary.

The homogenous solution for the PDE is assumed to be a product of independent temporal and spatial functions:

$$w(x, t) = W(x)F(t) \tag{2.41}$$

Substituting the solution into the PDE, we obtain:

$$EI\, W^{iv}(x)F(t) + mW(x)\ddot{F}(t) = 0 \tag{2.42}$$

Separating the functions of time, t, and space, x:

$$\frac{\ddot{F}(t)}{F(t)} = -\frac{EI}{m}\frac{W^{iv}(x)}{W(x)} = \text{constant} = -\lambda \tag{2.43}$$

The temporal solution gives the relationship between the natural frequencies, $\omega$, and the eigenvalues, $\lambda$. The differential equation for the temporal solution is:

$$\ddot{F}(t) + \lambda F(t) = 0 \tag{2.44}$$

The general solution is assumed to be in the following forms:

$$\begin{aligned} F(t) &= Ae^{i\omega t} + \bar{A}e^{-i\omega t} \\ &= C\cos(\omega t + \phi) \end{aligned} \tag{2.45}$$

where

$$\lambda = \omega^2 \tag{2.46}$$

The constants A and its complex conjugate, $\bar{A}$, (or C and the phase, $\phi$) are determined from the initial conditions. The natural frequency, $\omega$, is determined by solving the spatial problem given by:

$$W^{iv}(x) - \beta^4 W(x) = 0 \tag{2.47}$$

where

$$\beta = \sqrt[4]{\frac{m\lambda}{EI}} \tag{2.48}$$

The solution of equation (2.47) is of the form:

$$\begin{aligned} W(x) &= Ae^{\beta x} + Be^{-\beta x} + Ce^{i\beta x} + De^{-i\beta x} \\ &= C_1\sinh\beta x + C_2\cosh\beta x + C_3\sin\beta x + C_4\cos\beta x \end{aligned} \tag{2.49}$$

The constants are determined through the boundary conditions:

$$\begin{array}{rcl} W(0) = 0 & \Rightarrow & \\ W^{i}(0) = 0 & \Rightarrow & \\ W^{ii}(L) = 0 & \Rightarrow & \\ W^{iii}(L) = 0 & \Rightarrow & \end{array} \begin{bmatrix} 0 & 1 & 0 & 1 \\ 1 & 0 & 1 & 0 \\ \sinh\beta L & \cosh\beta L & -\sin\beta L & -\cos\beta L \\ \cosh\beta L & \sinh\beta L & -\cos\beta L & \sin\beta L \end{bmatrix} \begin{Bmatrix} C_1 \\ C_2 \\ C_3 \\ C_4 \end{Bmatrix} = \begin{Bmatrix} 0 \\ 0 \\ 0 \\ 0 \end{Bmatrix} \tag{2.50}$$

Non-trivial solutions are obtained by setting the determinant of the matrix equal to zero. The resulting equation is:

$$\cosh\beta L \cdot \cos\beta L + 1 = 0 \tag{2.51}$$

Since the model is a continuous beam, there are an infinite number of solutions and thus an infinite number of modes. The first eight solutions of equation (2.51) are: $\beta L = 1.8750$, 4.6940, 7.8550, 10.9960, 14.1370, 17.2790, 20.4200, 23.5620. These values of $\beta L$ hold true for all BE beams that have clamped-free boundary conditions.

The natural frequencies are calculated from $\beta L$ by equations (2.46) and (2.48):

$$\omega_r = \sqrt{\lambda_r} = (\beta_r L)^2 \sqrt{\frac{EI}{mL^4}} \tag{2.52}$$

The natural frequencies are dependent upon the material and beam properties. Stiffer beams (large EI) have higher natural frequencies and heavier beams (large mL) have lower natural frequencies. Since there were originally five unknowns ($C_{1\text{-}4}$ and $\beta$), and four equations the system is under determined. However, if we set the value for one constant, we can solve for the other three.

If $C_4 = -1$, then:

$$\begin{aligned} C_1 &= -\frac{\cosh\beta L + \cos\beta L}{\sinh\beta L + \sin\beta L} \\ C_2 &= 1 \\ C_3 &= \frac{\cosh\beta L + \cos\beta L}{\sinh\beta L + \sin\beta L} \\ C_4 &= -1 \end{aligned} \tag{2.53}$$

and the complete solution for W(x) is:

$$W(x) = (\cosh\beta x - \cos\beta x) - (\sinh\beta x - \sin\beta x) \cdot \left(\frac{\cosh\beta L + \cos\beta L}{\sinh\beta L + \sin\beta L}\right) \qquad (2.54)$$

The mode shapes of the beam are obtained by substituting in the values of $\beta$ and $\beta L$ into Equation (2.54). Note that the mode shapes are only dependent upon the boundary conditions and the length of the beam. However, the length of the beam can be removed from the mode shape expression through a non-dimensional variable $\xi = x/L$. Using the equivalent beam parameters in Table 2.2, natural frequencies of the first eight modes are listed in Table 2.3 and Figure 2.9 shows the first three mode shapes.

**TABLE 2.3** Continuous Bernoulli-Euler Beam

| | **Natural Frequencies** | |
|---|---|---|
| **Mode #** | $\omega_r$ **[rad/s]** | $f_r$ **[Hz]** |
| 1 | 2094 | 333.3 |
| 2 | 1.312e4 | 2089 |
| 3 | 3.675e4 | 5849 |
| 4 | 7.202e4 | 1.146e4 |
| 5 | 1.190e5 | 1.895e4 |
| 6 | 1.778e5 | 2.830e4 |
| 7 | 2.484e5 | 3.953e4 |
| 8 | 3.307e5 | 5.263e4 |

### 2.2.3 Timoshenko Beam

In the Bernoulli-Euler beam formulation rotary inertia and shear deformation are neglected. This simplification is valid for slender beams at lower frequencies, but degrades higher mode predictions. The effects become significant for thick beams and slender beams at higher frequencies.

Shear effects are accounted for in the Timoshenko beam model by redefining the deflection angle as follows:

Figure 2.9(a)
Mode #1
333.3 Hz

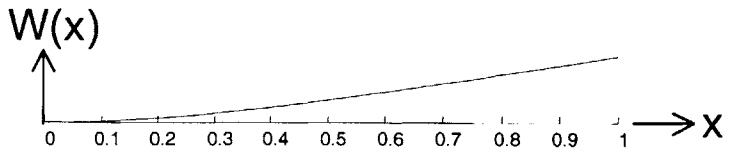


Figure 2.9(b)
Mode #2
2089 Hz

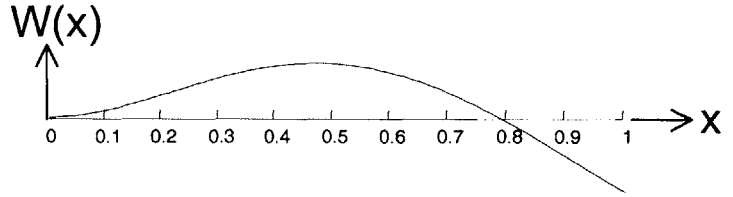


Figure 2.9(c)
Mode #3
5849 Hz

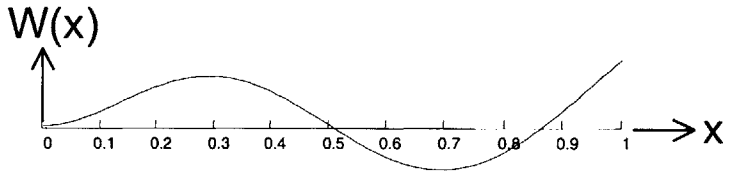


**Figure 2.9** First three mode shapes for continuous Bernoulli-Euler beam

$$\frac{\partial}{\partial x} w(x, t) = \psi(x, t) + \beta(x, t) \tag{2.55}$$

where w(x,t) is the translational displacement of the beam, $\psi(x,t)$ is the angle of deflection without shear effects (only due to the translational displacement) and $\beta(x,t)$ is the angle of deflection due to shear as shown in Figure 2.10.

Equation (2.55) includes two dependent variables, $\psi$ and $\beta$. Substituting (2.55) into the Timoshenko beam equations of motion results in a set of two dependent PDE's:

$$\begin{aligned} m\ddot{w} - k'AG(w^{ii} - \psi^{i}) &= 0 \\ EI\psi^{ii} + k'AG(w^{i} - \psi) - J\ddot{\psi} &= 0 \end{aligned} \tag{2.56}$$

where k' is the shear area factor, A is the cross-sectional area, G is the modulus of elasticity in shear and J is the rotary inertia per unit length defined by the product, $\rho I$.

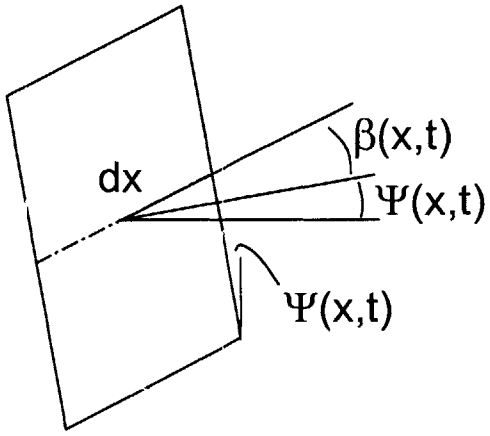


**Figure 2.10** Deflection for Timoshenko beam [Meirovich, 1997]
In a Bernoulli-Euler beam, $\beta = 0$.

Decoupling equations (2.56) and writing two PDE's in terms of $\psi$ and w gives:

$$\begin{aligned} EIw^{iv} + m\ddot{w} - \left(J + \frac{EIm}{k'AG}\right)\frac{\partial^4 w}{\partial x^2 \partial t^2} + \frac{Jm}{k'AG}\frac{\partial^4 w}{\partial t^4} &= 0 \\ EI\psi^{iv} + m\ddot{\psi} - \left(J + \frac{EIm}{k'AG}\right)\frac{\partial^4 \psi}{\partial x^2 \partial t^2} + \frac{Jm}{k'AG}\frac{\partial^4 \psi}{\partial t^4} &= 0 \end{aligned} \tag{2.57}$$

The following derivation of the solutions to the Timoshenko PDE (Equation (2.57)) is taken from Huang [Huang, 1961]. With the introduction of a non-dimensional variable, $\xi$, the solutions for w(x,t) and $\psi$(x,t) are assumed to be in the following form:

$$\begin{aligned} w(\xi) &= We^{i\omega t} \\ \psi(\xi) &= \Psi e^{i\omega t} \\ \xi &= \frac{x}{L} \end{aligned} \tag{2.58}$$

Substituting Equations (2.58) into Equation (2.57) we obtain:

$$\begin{aligned} W^{iv} + b^2(r^2 + s^2)W'' - b^2(1 - b^2r^2s^2)W &= 0 \\ \Psi^{iv} + b^2(r^2 + s^2)\Psi'' - b^2(1 - b^2r^2s^2)\Psi &= 0 \end{aligned} \tag{2.59}$$

where:

$$b^2 = \frac{mL^4\omega^2}{EI}$$
$$r^2 = \frac{I}{AL^2} \tag{2.60}$$
$$s^2 = \frac{EI}{k'AG}$$

The boundary conditions for the cantilever beam are:

$$\begin{array}{lll} \text{at } \xi = 0 & W(0) = 0 & \Psi(0) = 0 \\ \text{at } \xi = 1 & \frac{1}{L}W^i(1) - \Psi(1) = 0 & \Psi^i(1) = 0 \end{array} \tag{2.61}$$

The solutions of equation (2.59) can be written as:

$$\begin{aligned} W &= C_1\cosh(b\alpha\xi) + C_2\sinh(b\alpha\xi) + C_3\cos(b\beta\xi) + C_4\sin(b\beta\xi) \\ \Psi &= C_1^i\cosh(b\alpha\xi) + C_2^i\sinh(b\alpha\xi) + C_3^i\sin(b\beta\xi) + C_4^i\cos(b\beta\xi) \end{aligned} \tag{2.62}$$

where

$$\frac{\alpha}{\beta} = \frac{1}{\sqrt{2}}\left\{\mp(r^2+s^2) + \left[(r^2-s^2)^2 + \frac{4}{b^2}\right]^{1/2}\right\}^{1/2} \tag{2.63}$$

when the following condition holds

$$\left[(r^2-s^2)^2 + \frac{4}{b^2}\right]^{1/2} > (r^2+s^2) \tag{2.64}$$

When the condition in Equation (2.64) is not met, as is the case for the sample problem, substitute the solutions for W and $\Psi$ are written as:

$$\begin{aligned} W &= C_1\cos(b\alpha'\xi) + iC_2\sin(b\alpha'\xi) + C_3\cos(b\beta\xi) + C_4\sin(b\beta\xi) \\ \Psi &= iC_1'\sin(b\alpha'\xi) + C_2'\cos(b\alpha'\xi) + C_3'\sin(b\beta\xi) + C_4'\cos(b\beta\xi) \end{aligned} \tag{2.65}$$

where $\alpha'$ is given by:

$$\alpha' = \frac{1}{\sqrt{2}}\left\{(r^2+s^2) - \left[(r^2-s^2)^2 + \frac{4}{b^2}\right]^{1/2}\right\}^{1/2} \tag{2.66}$$

The eight constants in equation (2.65) are not independent; there are only four independent constants ($C_{1\text{-}4}$ or $C'_{1\text{-}4}$) and they are related to each other through equation (2.56). As done for the Bernoulli Euler beam in Equation (2.50), the non-trivial solutions for the constants produce the characteristic equation for the clamped-free beam:

$$2 + [b^2(r^2-s^2)^2 + 2]\cos b\alpha'\cos b\beta - \frac{b(r^2+s^2)}{(b^2r^2s^2-1)^{1/2}}\sin b\alpha'\sin b\beta = 0 \tag{2.67}$$

The characteristic equation is obtained in terms of the natural frequencies, $\omega$, by substituting the expressions for $\alpha$, $\beta$, and b (equations (2.60) and (2.66)). The natural frequencies are the roots of the resulting polynomial.

The four constants ($C_{1\text{-}4}$ or $C'_{1\text{-}4}$) are determined from the remaining three independent equations by choosing a value for one constant and solving for the other three. These constants are substituted back into to equation (2.65) to obtain the complete solution for W and $\Psi$:

$$\begin{aligned} W &= D[\cos b\alpha'\xi + \lambda'\zeta\eta\sin b\alpha'\xi - \cos b\beta\xi + \eta\sin b\beta\xi] \\ \Psi &= H\left[\cos b\alpha'\xi - \frac{1}{\lambda'\zeta}\mu\sin b\alpha'\xi - \cos b\beta\xi + \mu\sin b\beta\xi\right] \end{aligned} \tag{2.68}$$

where:

$$\lambda' = \frac{\alpha'}{\beta}$$

$$\zeta = \frac{(\beta^2 - s^2)}{(\beta^2 - r^2)}$$

$$\eta = \frac{\frac{1}{\lambda'}\sin b\alpha' - \sin b\beta}{\zeta \cos b\alpha' + \cos b\beta} \tag{2.69}$$

$$\mu = \frac{\lambda' \sin b\alpha' - \sin b\beta}{\frac{1}{\zeta}\cos b\alpha' + \cos b\beta}$$

The constants D and H are dependent upon the initial conditions. They, too, are related to each other through equations (2.56). The translational mode shape is given by W, the slope is given by $W^1$ and $\Psi$ (equation (2.68)). The first eight natural frequencies and the first three mode shapes for the Timoshenko cantilevered beam are presented in Table 2.4 and Figure 2.11, respectively. Comparing the mode shapes of the BE beam and the Timoshenko beam, the difference that is most readily apparent is the angle of the deflection towards the tips of the beam in all three modes. Note also that the Timoshenko beam has significantly lower frequencies than the BE beam.

**TABLE 2.4** Modes for continuous equivalent Timoshenko beam

| Mode # | rad/s | Hz |
|---|---|---|
| 1 | 909.4 | 144.7 |
| 2 | 2731 | 434.7 |
| 3 | 4872 | 775.3 |
| 4 | 6257 | 995.8 |
| 5 | 7190 | 1144 |
| 6 | 9029 | 1437 |
| 7 | 1.104 e4 | 1757 |
| 8 | 1.303 e4 | 2075 |

Figure 2.11(a)
Mode #1
145 Hz

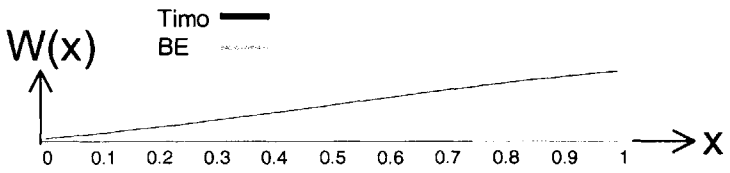


Figure 2.11(b)
Mode #2
435 Hz

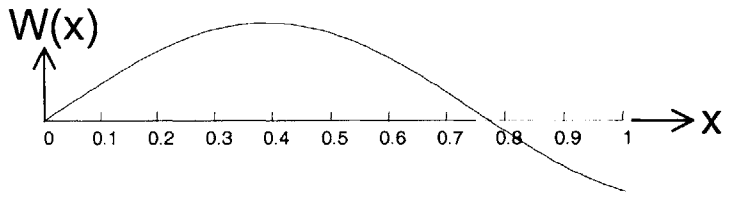


Figure 2.11(c)
Mode #3
775 Hz

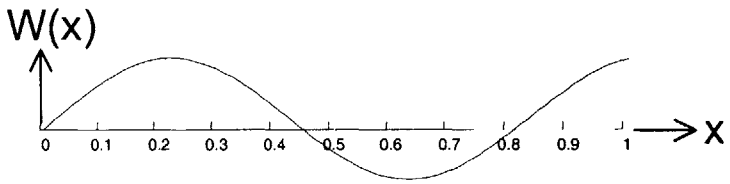


**Figure 2.11** Mode shapes of cantilevered Timoshenko beam (with BE beam)

## Stick Models

### Rod in axial compression

Figure 2.12 shows the finite element representation of a rod carrying only axial loads, where m is the mass per unit length, E is the modulus of elasticity, and A is the cross-sectional area [Meirovich, 1975]. All the material properties are considered constant across the length of the element.

The axial displacement of any point on the rod, u(x,t) is assumed to be a superposition of two displacement functions, one at each node. Each nodal function is assumed to be a function of both time, t, and length along beam, x. Total axial displacement u(x,t) is given by:

$$u(x,t) = \phi_1(x)u_1(t) + \phi_2(x)u_2(t) \tag{2.70}$$

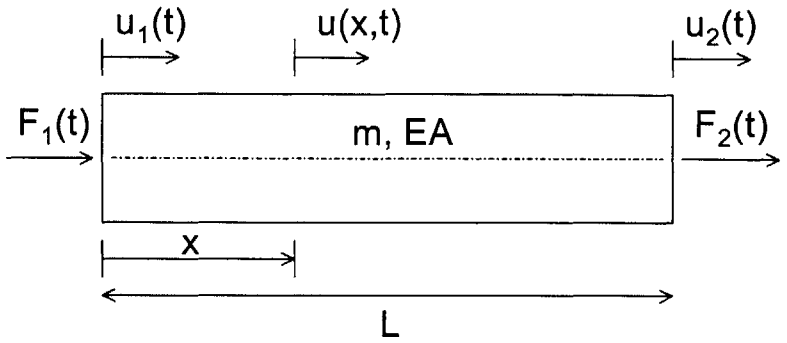


**Figure 2.12** rod with axial forces

where $\phi_i(x)$ are shape functions that linearly represent static displacement patterns subject to the boundary conditions:

$$u(0, t) = u_1(t) \qquad u(L, t) = u_2(t) \tag{2.71}$$

In terms of $\phi$, the boundary conditions are:

$$\begin{aligned} \phi_1(0) &= 1 \qquad \phi_1(L) = 0 \\ \phi_2(0) &= 0 \qquad \phi_2(L) = 1 \end{aligned} \tag{2.72}$$

The equation of motion for axial vibration of a beam is:

$$-m\frac{\partial^2 u}{\partial t^2} + EA\frac{\partial^2 u}{\partial x^2} = f(x, t) \tag{2.73}$$

where f(x,t) is the force function.

For static displacement, the frequency in equation (2.73) is zero. Setting time derivatives and forcing term to zero, the homogenous equation is:

$$\sum_{i=1}^{2} \phi_i^{ii} = 0 \qquad 0 < x < L \tag{2.74}$$

Integrating equation (2.74) twice, we obtain:

$$\phi_i(x) = c_1 x + c_2 \tag{2.75}$$

Using the boundary conditions to solve for the constants, we have:

$$\begin{aligned} \phi_1(x) &= 1 - \frac{x}{L} \\ \phi_2(x) &= \frac{x}{L} \end{aligned} \tag{2.76}$$

The axial displacement is obtained by substituting equation (2.76) into equation (2.70):

$$u(x, t) = \left(1 - \frac{x}{L}\right) u_1(t) + \frac{x}{L} u_2(t) \tag{2.77}$$

The equations of motion for the beam in terms of nodal forces and nodal displacements are formulated using the Lagrangian. The kinetic co-energy and potential energy terms are given by:

$$\begin{aligned} T^*(t) &= \frac{1}{2}\int_0^L m\left[\frac{\partial}{\partial t} u(x, t)\right]^2 dx \\ V(t) &= \frac{1}{2}\int_0^L EA\left[\frac{\partial}{\partial x} u(x, t)\right]^2 dx \end{aligned} \tag{2.78}$$

The principal of virtual work is used to formulate the nonconservative work done on the beam:

$$\delta \overline{W} = \int_0^L f(x, t)\delta u(x, t)dx + \sum_{j=1}^{2} f_j^*(t)\delta u_j(t) \tag{2.79}$$

where f(x,t) is a distributed non-conservative force and $f^*_j(t)$ is a nodal force imparted on node j by adjacent elements.

The equations of motion are then obtained with equations (2.78) and (2.79) and Lagrangian methods:

$$\begin{bmatrix} \frac{mL}{3} & \frac{mL}{6} \\ \frac{mL}{6} & \frac{mL}{3} \end{bmatrix} \begin{Bmatrix} \ddot{u}_1(t) \\ \ddot{u}_2(t) \end{Bmatrix} + \begin{bmatrix} \frac{EA}{L} & -\frac{EA}{L} \\ -\frac{EA}{L} & \frac{EA}{L} \end{bmatrix} \begin{Bmatrix} u_1(t) \\ u_2(t) \end{Bmatrix} = \begin{Bmatrix} f_1(t) \\ f_2(t) \end{Bmatrix} \tag{2.80}$$

where:

$$\begin{aligned} f_1(t) &= \int_0^L f(x,t)\left(1 - \frac{x}{L}\right)dx + f_1^*(t) \\ f_2(t) &= \int_0^L f(x,t)\frac{x}{L}dx + f_2^*(t) \end{aligned} \tag{2.81}$$

Equation (2.80) can be written in the form:

$$[m]\ddot{\mathbf{u}}(t) + [k]\mathbf{u}(t) = \mathbf{f}(t) \tag{2.82}$$

where $\mathbf{u}(t)$ is the nodal displacement vector, $\mathbf{f}(t)$ is the nodal forces given in equation (2.80) and [m] and [k] are the mass and stiffness matrices, respectively:

$$\begin{aligned} [m] &= \begin{bmatrix} \frac{mL}{3} & \frac{mL}{6} \\ \frac{mL}{6} & \frac{mL}{3} \end{bmatrix} \\ [k] &= \begin{bmatrix} \frac{EA}{L} & -\frac{EA}{L} \\ -\frac{EA}{L} & \frac{EA}{L} \end{bmatrix} \end{aligned} \tag{2.83}$$

**Beam in Bending**

The finite element representation of a Bernoulli-Euler beam in bending, restricted to motion in the plane, has a total of four degrees of freedom (Figure 2.13). There are two degrees of freedom at each node: transverse displacement and rotation in the plane of the beam.

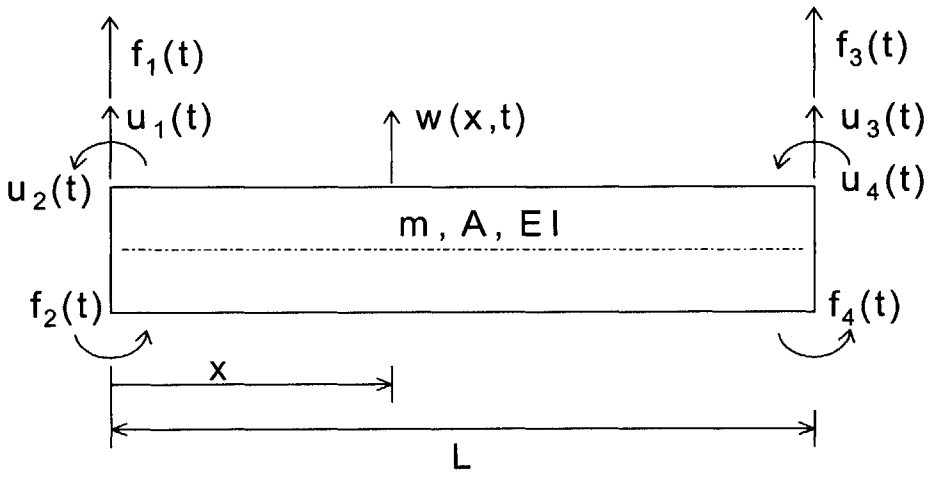


**Figure 2.13** degrees of freedom for BE beam in bending

The total displacement is given by a sum of the displacements of the four nodal displacements. The nodal displacements are assumed to be a product of shape functions and temporal functions. The shape functions linearly represent static displacement patterns subject to the boundary conditions. The translational displacement is given by:

$$w(x, t) = \sum_{i=1}^{4} \phi_i(x) u_i(t) \tag{2.84}$$

The boundary conditions for the beam are:

$$\begin{aligned} w(0, t) &= u_1(t) \qquad \frac{\partial}{\partial x} w(x, t)\Big|_{x=0} = u_2(t) \\ w(L, t) &= u_3(t) \qquad \frac{\partial}{\partial x} w(x, t)\Big|_{x=L} = u_4(t) \end{aligned} \tag{2.85}$$

The boundary conditions in terms of the shape functions are:

$$\begin{array}{llll}
\phi_1(0) = 1 & \phi_1(L) = 0 & \left.\frac{d\phi_1}{dx}\right|_{x=0} = 0 & \left.\frac{d\phi_1}{dx}\right|_{x=L} = 0 \\
\phi_2(0) = 0 & \phi_2(L) = 0 & \left.\frac{d\phi_2}{dx}\right|_{x=0} = 1 & \left.\frac{d\phi_2}{dx}\right|_{x=L} = 0 \\
\phi_3(0) = 0 & \phi_3(L) = 1 & \left.\frac{d\phi_3}{dx}\right|_{x=0} = 0 & \left.\frac{d\phi_3}{dx}\right|_{x=L} = 0 \\
\phi_4(0) = 1 & \phi_4(L) = 0 & \left.\frac{d\phi_4}{dx}\right|_{x=0} = 0 & \left.\frac{d\phi_4}{dx}\right|_{x=L} = 0
\end{array} \tag{2.86}$$

To create a Bernoulli-Euler bending beam element, use equation (2.39), set the time derivative to zero to remove the inertia terms, set f(x,t) = 0, and divide through by EI to get:

$$\frac{d^4}{dx^4}\phi_i(x) = 0 \qquad 0 < x < L \tag{2.87}$$

Integrating equation (2.87) four times gives the general solution:

$$\phi_i(x) = \frac{1}{6}c_1x^3 + \frac{1}{2}c_2x^2 + c_3x + c_4 \tag{2.88}$$

The constants are determined from the boundary conditions to obtain:

$$\begin{aligned}
\phi_1(x) &= 1 - 3\frac{x^2}{L^2} + 2\frac{x^3}{L^3} \\
\phi_2(x) &= x - 2\frac{x^2}{L} + \frac{x^3}{L^2} \\
\phi_3(x) &= 3\frac{x^2}{L^2} - 2\frac{x^3}{L^3} \\
\phi_4(x) &= -\frac{x^2}{L} + \frac{x^3}{L^2}
\end{aligned} \tag{2.89}$$

Substituting equation (2.89) into equation (2.84), Lagrangian methods are used to calculate the equations of motion, similarly to derivation of the rod equations. The equations of

motion written in matrix form are given by equation (2.82), where the [m] and [k] matrices for the BE beam finite element are:

$$[m] = \frac{mL}{420}\begin{bmatrix} 156 & 22L & 54 & -13L \\ 22L & 4L^2 & 13L & -3L^2 \\ 54 & 13L & 156 & -22L \\ -13L & -3L^2 & -22L & 4L^2 \end{bmatrix}$$

$$[k] = \frac{EI}{L^3}\begin{bmatrix} 12 & 6L & -12 & 6L \\ 6L & 4L^2 & -6L & 2L^2 \\ -12 & -6L & 12 & -6L \\ 6L & 2L^2 & -6L & 4L^2 \end{bmatrix} \qquad (2.90)$$

The finite element matrices in equation (2.90) only represent four out of twelve possible degrees of freedom for a Bernoulli-Euler beam. The other eight are from: the bending and translational degrees of freedom in the plane perpendicular to the plane shown in Figure 2.13; axial translation along the length of the beam; and torsional rotation.

**Truss as Bernoulli-Euler beam**

Beam elements are represented in NASTRAN with a CBAR card. CBAR cards represent either Bernoulli-Euler beams or Timoshenko beams depending on the values of the shear area factors, K1 and K2. These values are set to infinity by default, effectively removing the effects of shear flexibility, and creating BE beam elements [Kilroy, 1997]. Timoshenko beams are obtained by setting finite values for the factors. The material values and the equivalent beam property values entered in NASTRAN are those listed in Table 2.2.

Table 2.5 lists the natural frequencies of a selection of modes of the Bernoulli-Euler beam truss calculated for different mesh refinements. The first column is the number of elements used to represent the 1m long beam. The continuous solution is shown in the bottom line for comparison and essentially represents infinite elements for the beam. The frequencies calculated from the finite element models converge to these continuous solutions. The "-" in some table entries means that there are not enough degrees of freedom to calculate

**TABLE 2.5** Bending modes of the BE beam FEM

| number of elements (n) | Natural Frequencies $f_1$ [Hz] | $f_2$ [Hz] | $f_3$ [Hz] | $f_8$ [Hz] |
|---|---|---|---|---|
| 1 | 232.2 | - | - | - |
| 2 | 299.2 | 1541 | - | - |
| 3 | 317.2 | 1790 | 832.6 | - |
| 4 | 324.0 | 1904.5 | 5043 | - |
| 6 | 329.1 | 2001 | 5456 | - |
| 8 | 330.9 | 2038 | 5619 | 3.975 e4 |
| 10 | 331.8 | 2056 | 5700. | 4.683 e4 |
| 15 | 332.6 | 2074 | 5781 | 5.064 e4 |
| 20 | 332.9 | 2081 | 5811 | 5.155 e4 |
| 30 | 333.1 | 2085 | 5832 | 5.216 e4 |
| 40 | 333.2 | 2087 | 5839 | 5.237 e4 |
| continuous | 333.3 | 2089 | 5849 | 5.263 e4 |

the mode. Axial modes are also calculated in the FE analysis, but since the continuous solution only considers transverse bending modes the axial mode frequencies from NASTRAN are not included in the table. The mode number in the first row indicates the bending modes only; for example, $\omega_8$ is the eighth bending mode, not the eighth mode.

Figure 2.14 shows the mode shapes for the first three bending modes of the beam with 40 elements. They are the discrete representation of the mode shapes plotted from the continuous solution shown in Figure 2.9. The finite element mode shape resembles the continuous solution well with 40 elements as can be seen by comparing the frequencies listed in Table 2.5 for 40 elements with those of the continuous solution.

The percent error of the finite element natural frequency prediction compared to the continuous solution for the four modes listed in Table 2.5 is shown in Figure 2.16. The trend shows that as the mode number increases, the error increases and as the mesh refinement increases, the error decreases. The general rule of thumb for mesh sizing is to have 5 to 10

Figure 2.14(a)
Mode #1
333 Hz

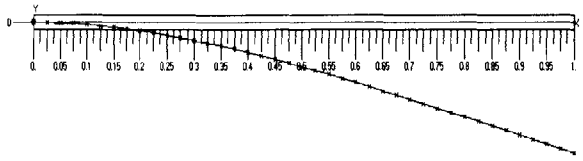

Figure 2.14(b)
Mode #3
2087 Hz

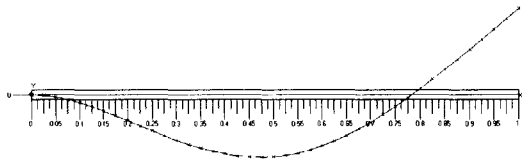

Figure 2.14(c)
Mode #6
5839 Hz

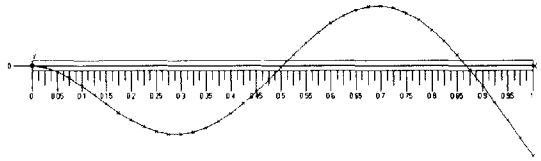

**Figure 2.14** Bernoulli Euler (40 elements) - modes shapes

Figure 2.15(a)
mode #1
331 Hz

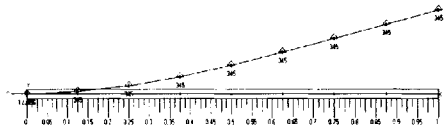

Figure 2.15(b)
Mode #7
5619 Hz

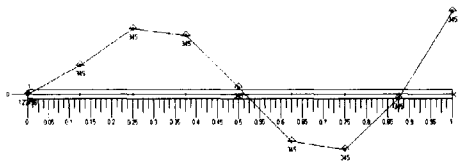

**Figure 2.15** Bernoulli-Euler Beam (8 elements) - mode shapes

nodes per half cycle of the response amplitude of interest [Blakely, 1993]. In Figure 2.9, the third mode has slightly more than two half cycles (the clamped-free condition does not produce clear half cycles as a clamped-clamped or pinned-pinned boundary conditions). Therefore, the rule of thumb would indicate 15-30 nodes (15-30 elements) are necessary

to adequately represent mode 3. Table 2.5 shows that 15 or 30 modes predicts the third mode to the accuracy of two significant digits. Figure 2.16 shows that there is about 1% error for 15 elements and less than 1% error for 30 elements.

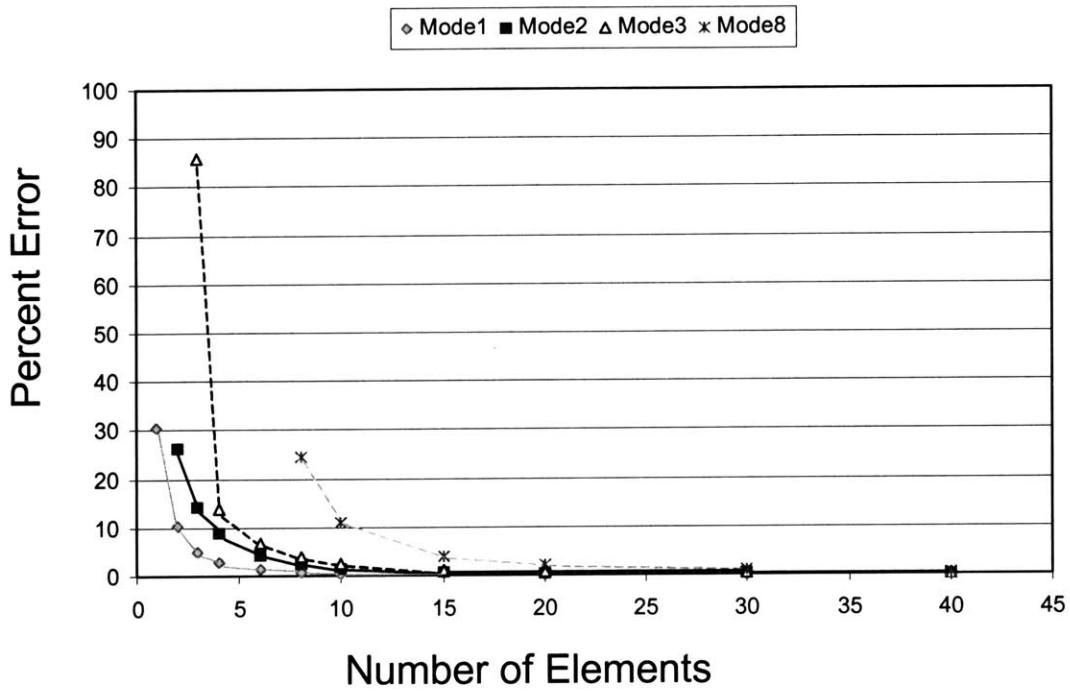


**Figure 2.16** percent error of BE-beam FEM mode compared to continuous BE-beam verses number of elements

### FE model for Timoshenko Beam

The FE elements for the Timoshenko beam are derived in a similar fashion as the rod and Bernoulli-Euler elements. The most significant difference with the Timoshenko beam is that because there are two dependent variables, two shape functions must be calculated, one for translation, w, and one for rotation, $\psi$ [Petyt, 1990]. However, the derivation will not be presented here since they are quite complicated and the resulting mass and stiffness matrices are extremely large. To read about the derivation of the Timoshenko finite element, see Dawe [Dawe, 1978] or Necib et al. [Necib, 1989].

NASTRAN is used to create the finite element of the Timoshenko beam stick model with the material and beam properties given by Table 2.2. Table 2.6 lists a selection of modes calculated for different mesh refinements.

**TABLE 2.6** Timoshenko beam FEM modes

| number of elements (n) | Natural Frequencies | | | |
|---|---|---|---|---|
| | $f_1$ [Hz] | $f_2$ [Hz] | $f_3$ [Hz] | $f_8$ [Hz] |
| 1 | 122.4 | - | - | - |
| 2 | 139.6 | 343.5 | - | - |
| 3 | 142.7 | 396.6 | 574.4 | - |
| 4 | 143.7 | 416.7 | 661.7 | - |
| 6 | 144.5 | 431.3 | 728.4 | - |
| 8 | 144.76 | 436.5 | 752.5 | 1616 |
| 10 | 144.9 | 438.9 | 763.8 | 1876 |
| 15 | 145.0 | 441.3 | 775.0 | 2154 |
| 20 | 145.0 | 442.1 | 779.0 | 2257 |
| 30 | 145.1 | 442.7 | 781.8 | 2332 |
| 40 | 145.1 | 442.9 | 782.8 | 2359 |
| continuous | 144.7 | 434.7 | 775.3 | 2075 |

The first three mode shapes for the Timoshenko beam with 40 elements are shown in Figure 2.17. They, too, are similar to the mode shapes of the continuous solution shown in Figure 2.11. Figure 2.18 shows the percent errors in the modes of the finite element model compared to the continuous solution. Though the errors get smaller with more elements, the errors do not approach zero as the number of modes increases. According to Figure 2.18 the ideal FE model has approximately 10 to 15 elements. This discrepancy is due to the assumptions made for the Timoshenko beam such as the elimination of the equivalent rotary inertia. As a result, the finite element model approaches a different continuous solution.

Figure 2.17(a)
Mode #1
145 Hz

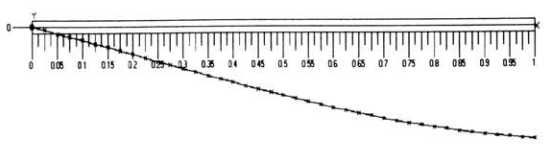

Figure 2.17(b)
Mode #2
443 Hz

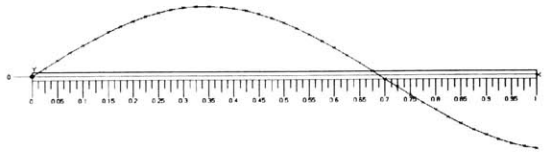

Figure 2.17(c)
Mode #3
783 Hz

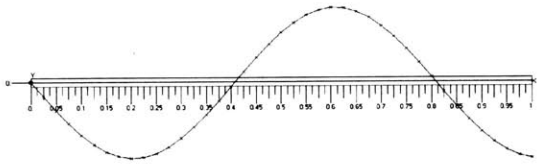

**Figure 2.17** Timoshenko beam (40 elements) - mode shapes

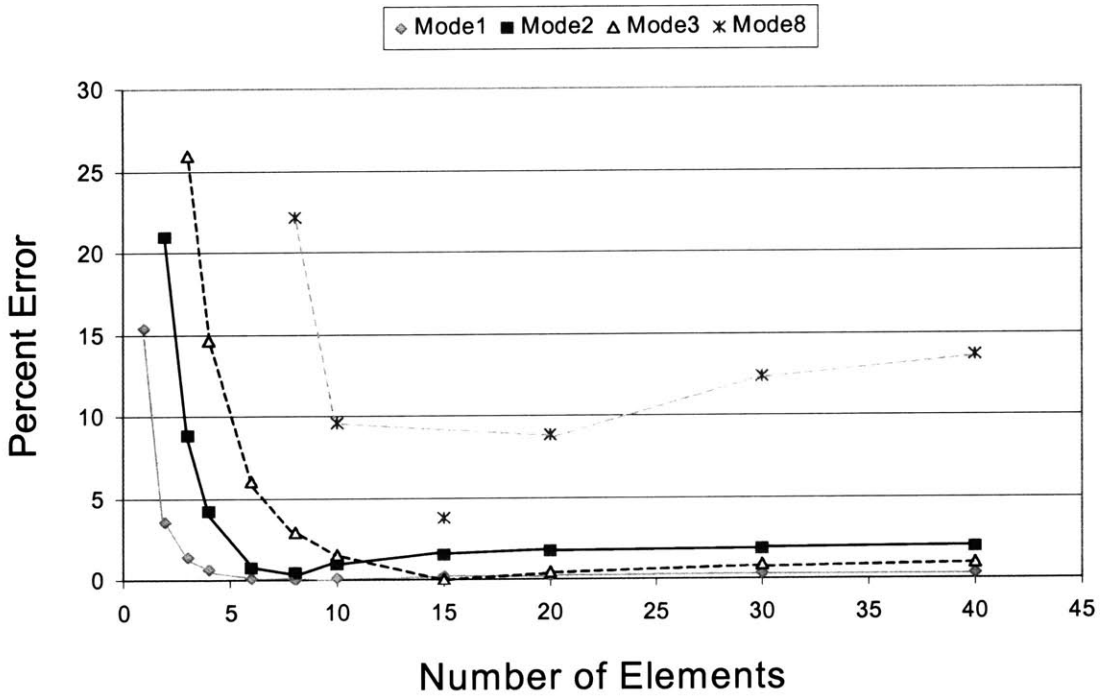


**Figure 2.18** Percent error of Timoshenko finite element models

### Compression rods

The next stage in the evolution of the sample truss problem is to accurately represent the geometry of the truss. The first truss type is the truss with rod members. The NASTRAN element CRODS are used for the finite element model of the truss with axial members.

Only one mesh size is possible for this model. The model assumed an ideal truss; members only experience compression and tension and all nodes are pin joints. Adding more elements per member introduces numerical errors in the solution. However, the mode shapes (Figure 2.19) created with the one rod per member truss shows that this model adequately covers the backbone behavior of the truss, but neglects the local modes of the truss members. Modes 1, 2 and 4 are the first three bending modes and resemble the modes of the stick models. Mode 3 is an axial mode of the truss and resembles the axial modes of the stick models which are not shown.

However, as the modes increase, the bending and axial modes of the truss become more coupled and are not easily segregated. Therefore, the frequencies of the first eight modes listed in Table 2.7 are not pure bending modes.

### FEM of Truss with bending rods

The final step in the evolution of the model fidelity is to use bending beams for the truss members. Timoshenko beam elements were used to eliminate possible errors associated with inaccurate modeling of the members.

Figure 2.19 shows four mode shapes for the truss with bending members. Modes 1 and 2 resemble the first two transverse bending modes of the stick models and the truss with rods. In mode 2, the bending of the truss members is clearly apparent. However, for the first two modes, the bending of the members is not significant enough to cause large errors between the natural frequencies of the rod truss (108.6 and 518.5 Hz) and bending beam truss (108.8 and 520.0 Hz). Mode 3 is an axial mode, also similar to the rod truss, but here the bending of the members are even more significant. After mode 3, none of the modes of

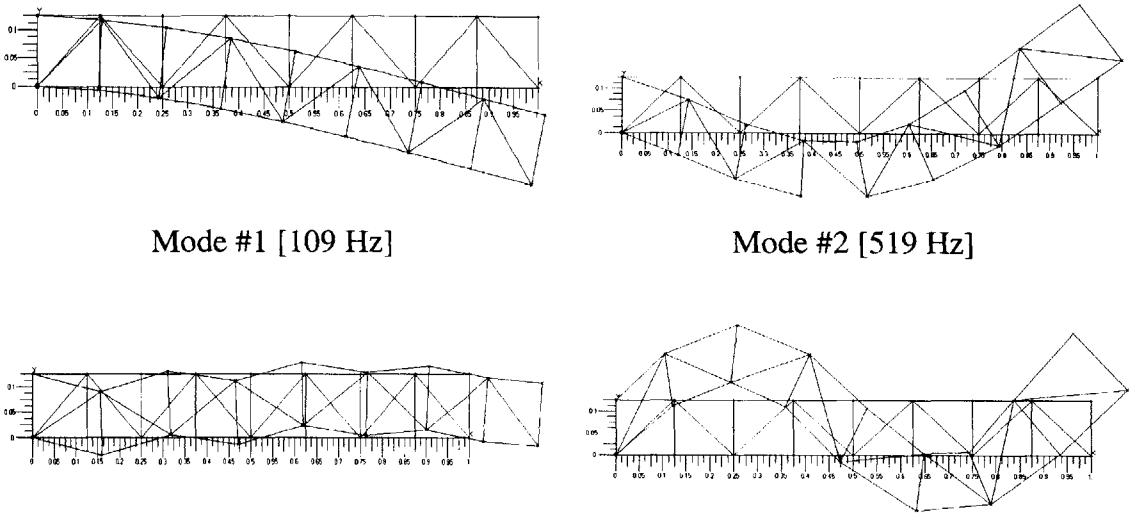

Mode #1 [109 Hz] Mode #2 [519 Hz]

Mode #3 [834 Hz] Mode #4 [1133 Hz]

**Figure 2.19** Truss with rods - mode shapes

**TABLE 2.7** Truss with rods

| Mode # | rad/s | Hz |
|---|---|---|
| 1 | 682.6 | 108.6 |
| 2 | 3258.1 | 518.5 |
| 3 | 5243.1 | 834.5 |
| 4 | 7115.9 | 1132 |
| 5 | 1.072 e4 | 1706 |
| 6 | 1.363 e4 | 2170 |
| 7 | 1.444 e4 | 2298 |
| 8 | 1.610 e4 | 2563 |

the truss with bending members resemble the stick model modes or the truss with rods. The higher mode shapes, represented by mode 54, involve the local bending modes of the truss members. Mode 54 was chosen because it depicts well the individual mode shapes of the members.

Table 2.8 shows the natural frequency values for four modes of varying mesh refinements. Figure 2.21 shows the percent error of the truss modes as a function of the number of ele-

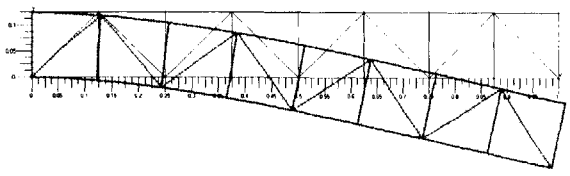

Figure 2.20(a) Mode #1 [109 Hz]

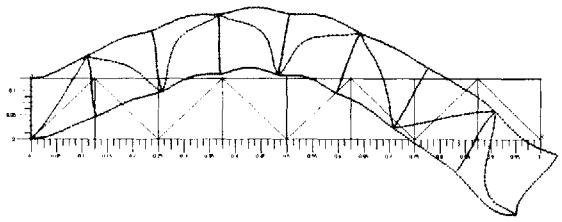

Figure 2.20(b) Mode #2 [519 Hz]

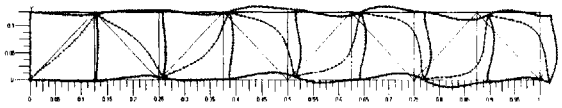

Figure 2.20(c) Mode #3 [711 Hz]

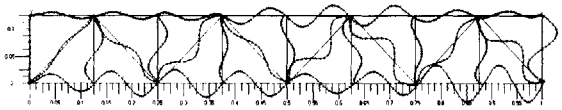

Figure 2.20(d) Mode #54 [4676 Hz]

**Figure 2.20** Truss with bending beams, higher mode

ments per member compared to the truss with 25 elements per member, considered the truth model. From the figure and table, it is seen that only a few elements are needed to model each member. The truss modeled with rods was able to capture the first two modes with zero error. Although only one element was used for each member, the truss is divided into eight bays which behaves as a refinement of at least the eight horizontal elements over the length of the truss. Additionally, even at mode 54, the members are still experiencing lower local mode shapes and thus need fewer elements to represent the behavior at low truss modes.

Comparing the natural frequencies of the truth model with the stick FE models, the stick models have stiffer bending modes than the truss represented by higher natural frequencies. The Bernoulli-Euler beam shows a large jump in frequency from the first mode to the second, but the Timoshenko beam's natural frequencies maintain the same order of magnitude for the first three modes (145.1, 442.9 and 782.8 Hz) as the truth model (109.5, 519.4, 711.0 Hz).

**TABLE 2.8** Truss with Bending Beams

| elements per member | Natural Frequencies | | | |
|---|---|---|---|---|
| | $f_1$ [Hz] | $f_2$ [Hz] | $f_3$ [Hz] | $f_8$ [Hz] |
| 1 | 108.8 | 520.0 | 836.4 | 2585 |
| 2 | 109.3 | 517.5 | 709.3 | 934.8 |
| 3 | 109.4 | 518.7 | 715.2 | 985.1 |
| 4 | 109.4 | 519.0 | 713.9 | 993.8 |
| 8 | 109.4 | 519.3 | 711.7 | 999.1 |
| 15 | 109.4 | 519.4 | 711.1 | 1000 |
| 25[a] | 109.5 | 519.4 | 711.0 | 1000 |

a. truth model

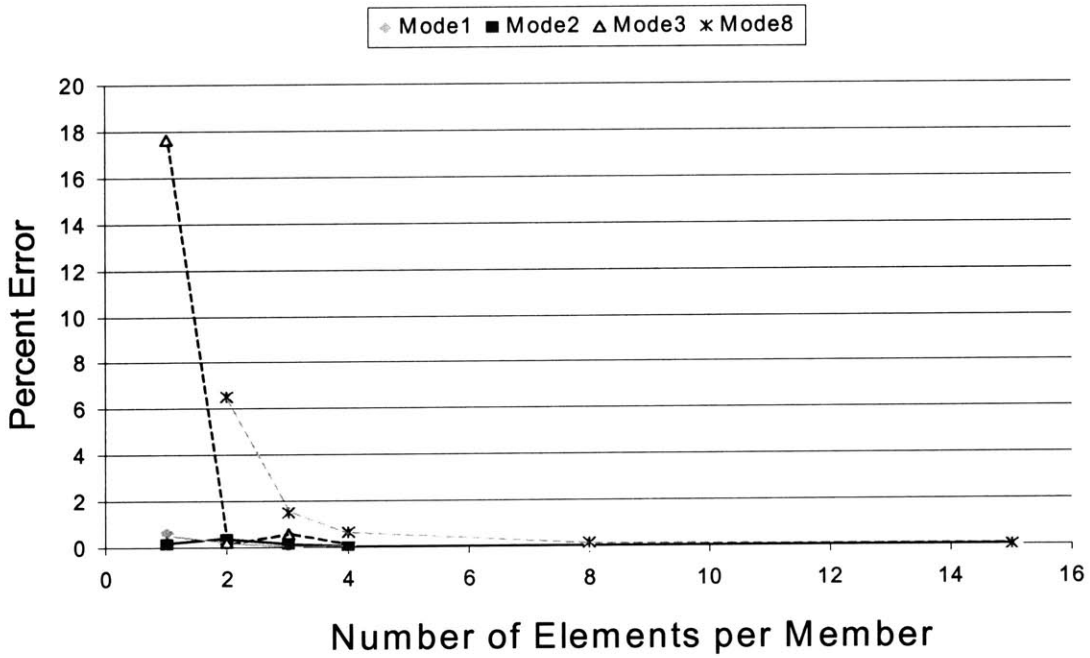


**Figure 2.21** Percent Error of Bar Truss modes vs. number of elements per member

### 2.2.4 Non-homogenous Analysis

Comparing the different models mode by mode may be misleading because the modes that are compared are generally chosen by the mode number (i.e. compare the eighth mode of two different models), or by modes that have similar frequencies (i.e. two modes that are around 5000 rad/s). This method is somewhat arbitrary since, except for the very low modes, the modes do not necessarily map across models.

Another means to compare the different models is to compare transfer functions. In this section the transfer functions from unit intensity white noise at node 7 (Figure 2.3) to the vertical tip displacement (node 9) for the different truss models are compared.

Modal damping of 0.5% is assumed and the **A** matrix is created from the natural frequencies (equation (2.18)). The B matrix has only one column since there is only one input to the system. The C matrix has only one row since there is only one performance from the system. Feedthrough is assumed to be zero so the D matrix is a one by one zero matrix.

First the transfer functions of each model type will be shown. For the two low fidelity models and the truss with bending beams, three different degrees of mesh refinements will be superimposed on the same graph to compare how refinement affects the model. Then, the transfer functions of the highly refined version of each type will be plotted on the same graph to discuss the evolution from one type of model to the next.

#### Bernoulli-Euler Beam

Figure 2.22 shows the transfer function for the BE beam with eight, twenty and one hundred elements. The first four modes are well correlated, but starting at the fifth mode the 8 element beam starts to deviate from the more refined models. The 20 element beam correlates with the 100 element beam well until the eleventh mode, but the errors start increasing significantly after the eighth mode.

The use of more elements increases number of observable modes. The total number of modes that can be calculated is twice the number of elements. Therefore, the 8 element

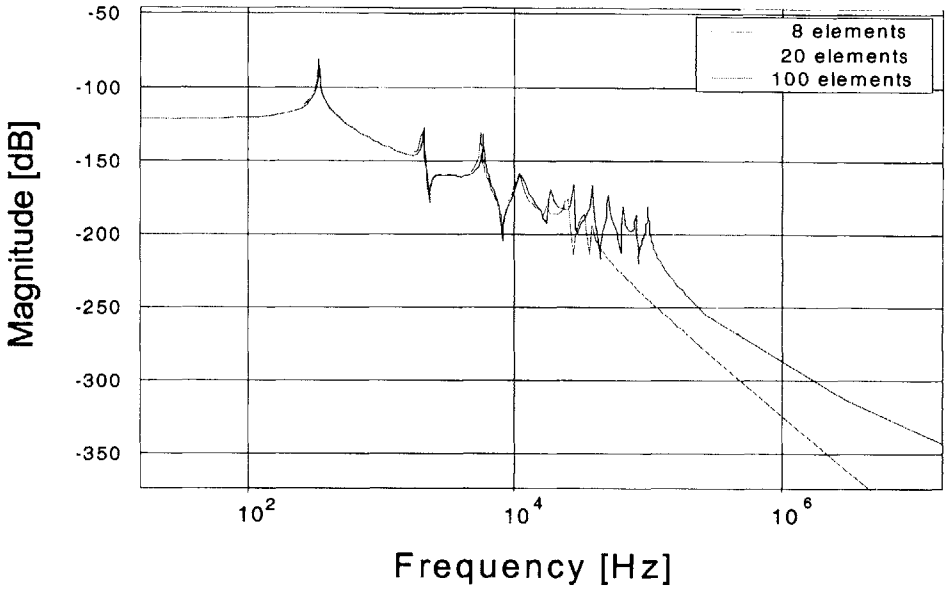


**Figure 2.22** BE beam SYS ID

beam has only 16 modes, the 20 element beam has 40 modes and the 100 element beam has 200 possible modes. The total number of modes calculated for all the modal analyses were limited to the first 100 to reduce computational time. Another difference among the mesh refinements is the slope rolloff. The 100 element model rolls off slightly slower than the previous two models. The 20 element model appears to rolloff more sharply than the 8 element model, but it eventually approaches to the same slope as the 8 element model.

### Timoshenko Beam

Figure 2.23 shows the transfer function for the Timoshenko beam with eight, twenty and one hundred elements. The first mode is well correlated, but by the third mode, there is an obvious deviation between the different models. By the fifth mode, the error between the models prevents comparison of modes. The number of observable modes increases as the mesh is refined, as with the Bernoulli-Euler beam. The total number of possible modes for the Timoshenko beam is also twice the number of elements. The pattern of the rolloff is also similar with the BE model where the 20 element and 8 element models rolloff at the same slope and the 100 element model rolls off at a shallower slope. The transition from

the last observable mode to the rolloff also become becomes more sharp from the 8 element to the 20 element model and the transition from the sharp drop to the rolloff shallows out for the 100 element model compared to the 20 element model.

The dynamics of the 20 element beam shows unusual high frequency behavior. The sudden change in the rolloff slope resembles the presence of a zero and the 20 element beam should not have more modes than the 100 element beam. This discrepancy must be looked at further to be resolved.

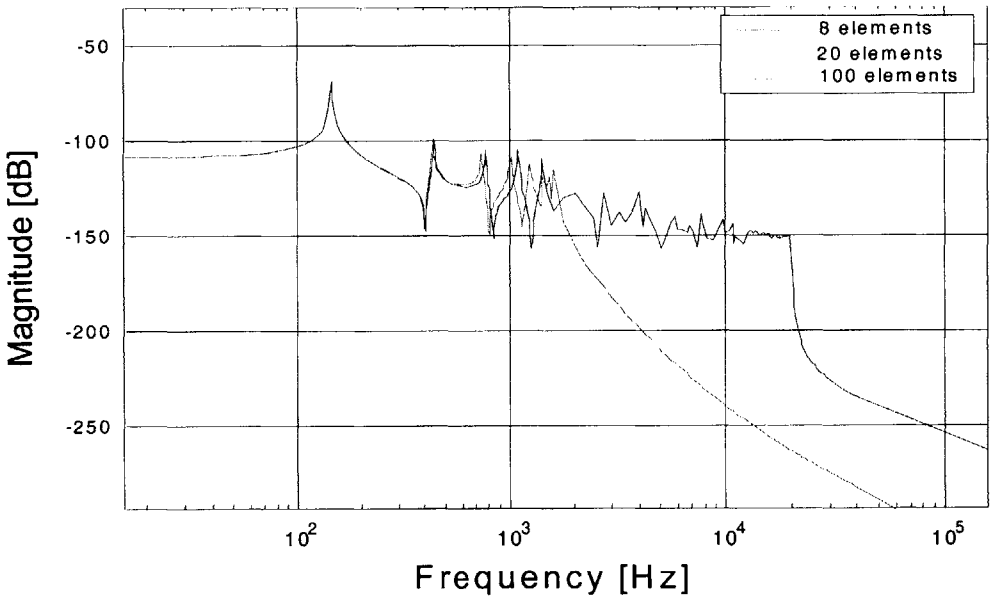


**Figure 2.23** Timoshenko beam transfer function

### Rod Truss

Figure 2.24 shows the transfer function for the truss with rod members. Though there are no other mesh refinements with which to compare the 1 element per member model, the general characteristics of the rod truss can be discussed. For example, the first four modes are very prominent compared to the other modes and the transfer function is modally dense towards $10^4$ Hz. The sharp drop after the last mode and the smooth transition from the drop the rolloff are present like in the transfer functions for the Timoshenko beam.

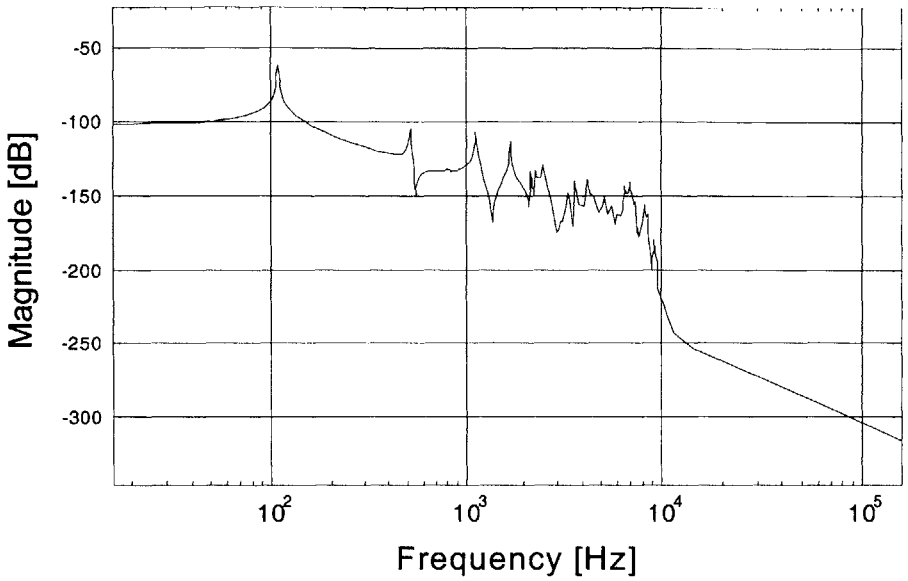


**Figure 2.24** Truss with rod members SYS ID

### Beam Truss

Figure 2.25 shows the transfer function for the beam truss with one, five and twenty-five elements per member. Unlike the two low fidelity models, only the first two modes are correlated between the three mesh models. The modal density increases significantly after the third mode and the 1 element per member model no longer has modal parity with the two other models. Only the slope of the transfer function in the region outlined is similar.

Figure 2.26 shows a close-up of the modally dense portion of the transfer function outlined in Figure 2.25. The 5 element per member model resembles the truth model well until around 1100Hz, at which point, the transfer function envelops the 100 elements model, but does not match modally.

### Model Comparison

The two transfer functions low-fidelity models and the bending beam model all show how the increase in refinement improves the calculations of the modes. The lower modes converge first while the higher modes have similar slope and magnitude. The higher mesh models have more modes and are more dense at high frequencies.

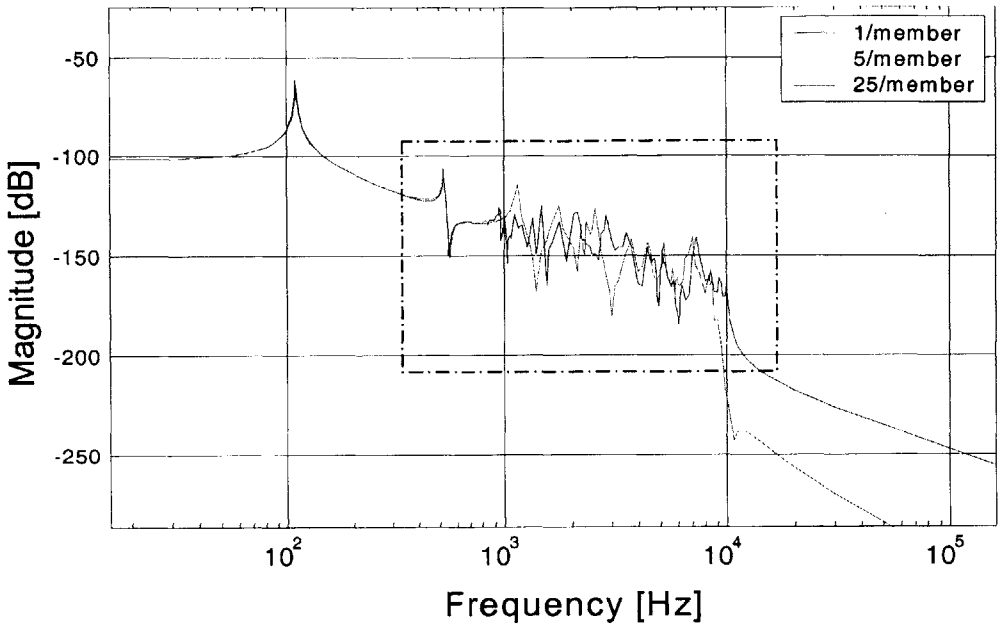


**Figure 2.25** Truss with Bending members SYS ID

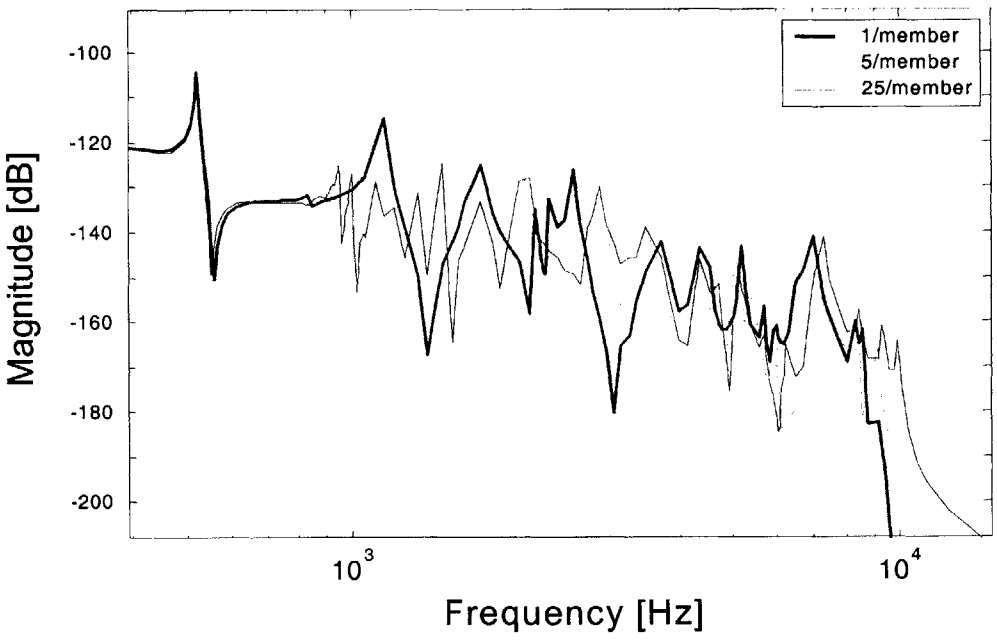


**Figure 2.26** Truss with bending members - zoom

To compare the transfer functions of the different models, the highest refined versions of the four different types are all plotted in Figure 2.27. Note that the first mode of the Bernoulli-Euler beam is higher and more damped than the other models. The Timoshenko beam is significantly closer to the actual mode and is less damped than the BE beam. The rod truss' first mode correlates well with the truth model.

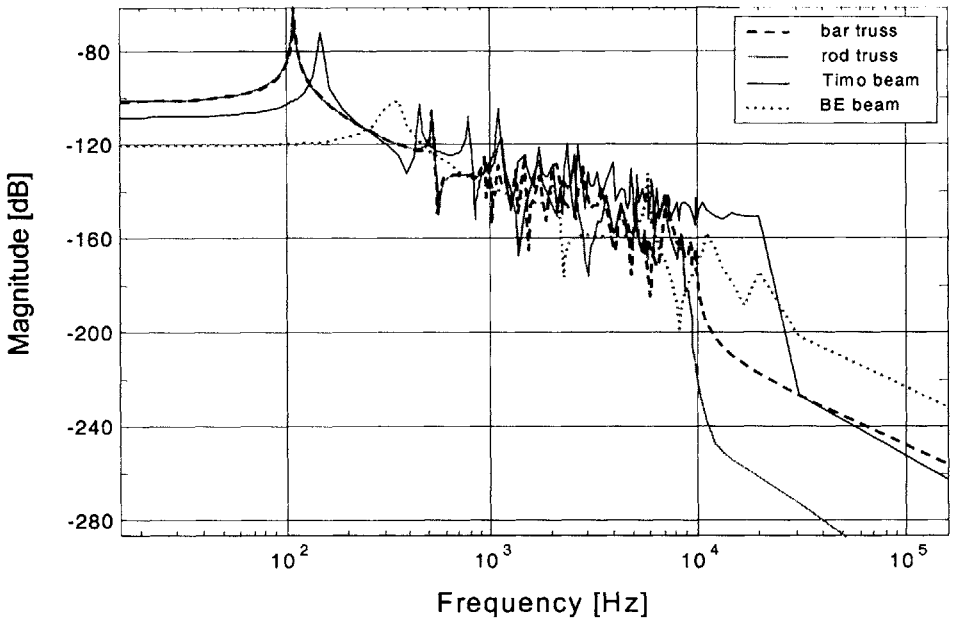


**Figure 2.27** Comparison of all four types

The next point of interest is the rolloff. All models, except the BE beam, have a drop off after the last mode and a shallowing out of the trailing edge of the transfer function. The Timoshenko beam actually overlaps the truth model, though its rolloff is slightly steeper. The rod truss drops off sooner than the truth model because it has 32 total modes compared to the 100 used for the bar truss.

Finally note from this figure is the slope of the dense high frequency portion of the transfer functions. All four models overlap each other in this middle portion, indicating that

they all have the same fundamental backbone to their modal characteristics and represent the same structure.

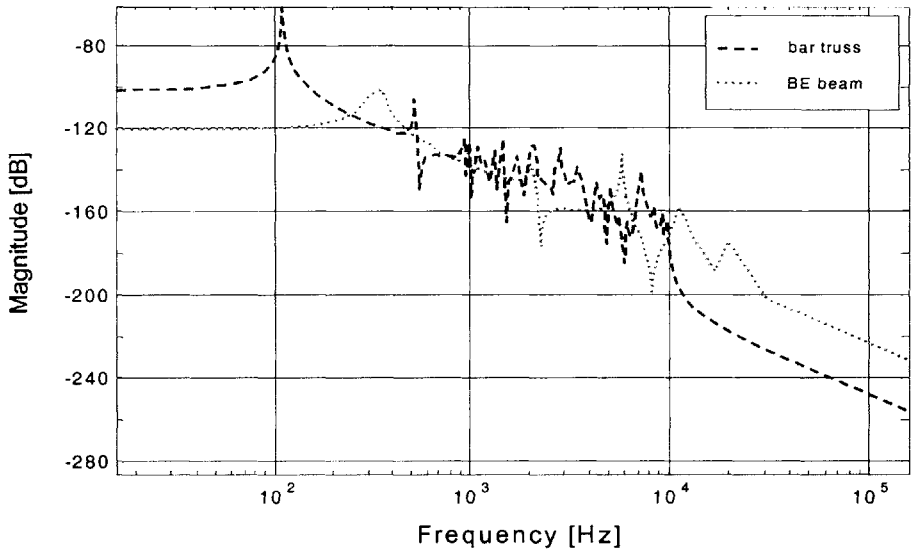


**Figure 2.28** Truth model and Bernoulli-Euler beam transfer functions

Figure 2.28 shows only the Bernoulli-Euler beam compared to the truth model. The first and last modes are shifted towards higher frequencies, but the slope is still similar. The modal density of the in-between modes is less for the BE beam than for the truss and the first four modes are quite spread out compared to the truss model. Because the BE beam has higher modes, it represents the structure as being stiffer than it really is. Since stiffer structures are better at damping out vibrations, the BE beam may inaccurately represent the performance as being better than the truth model.

Figure 2.29 shows the Timoshenko beam compared to the truth model. The first and last modes are less shifted than the BE beam and the first mode, as mentioned before, shows the same level of damping though the frequency of the mode is low. The modal density of the Timoshenko beam is higher than the BE beam, more closely resembling the dynamics of the truth model. The slope of the Timoshenko beam, however, is shallower than that of the truth model resulting in more energy in high-frequency modes than truth. Timoshenko

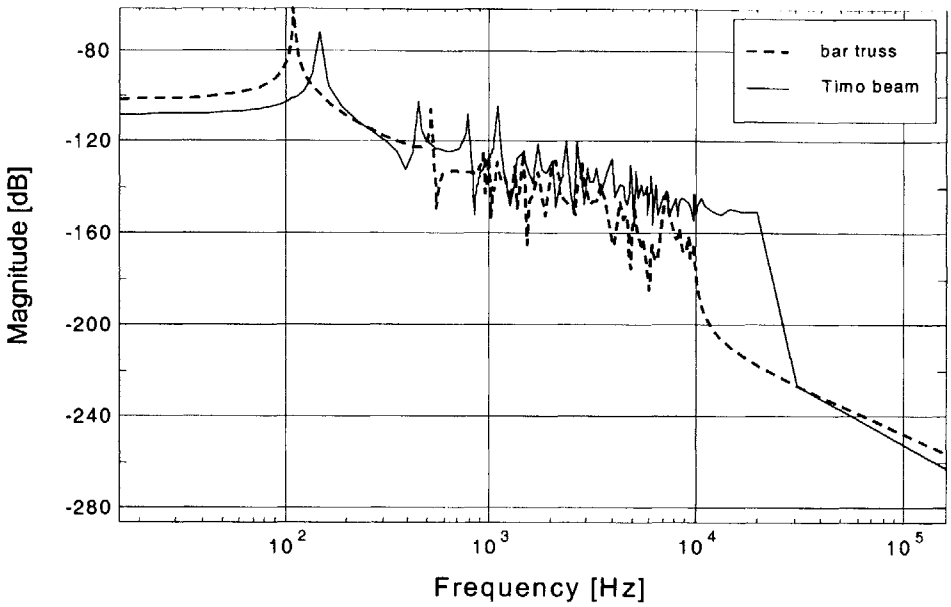


**Figure 2.29** Truth model and Timoshenko beam transfer functions

beam propagates more of the disturbance to the performance and gives a worse estimate than the truth.

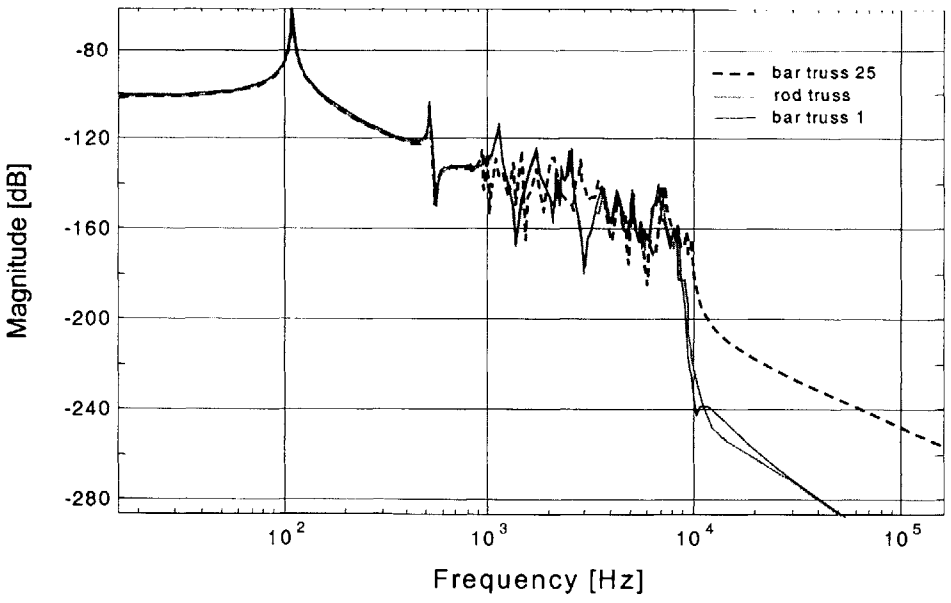


**Figure 2.30** Rod truss, bar truss with 1 element per member and truth model

Figure 2.30 shows the rod truss compared to the truth model. Due to the similarity of the rod truss with the bar truss with 1 element per member, it, too, is included in the figure. The rod truss and the 1-element bar truss have very similar transfer functions and correlate very well. However, the 1-element bar truss is slightly more accurate at representing the lower modes of the truth model. These two models compared to the truth model fare much better than the previous two stick models. They match the lower two modes almost identically and have the same slope through the higher frequency modes. They drop off away from the truth model after the last mode so that the rolloffs are not equal, but because the disturbance contributions from the rolloff contribute very little to the performance, the error from the rolloff is insignificant compared to the error in misrepresenting the middle portion of the transfer function.

### 2.2.5 Conclusions

All models have the same general shape with a few prominent low frequency modes, similar slope at higher frequencies and rolloff. The BE beam stiffens the structure by shifting the modes higher and damping the first mode more than the truth model. The Timoshenko beam better represents the first mode, but it, too, is in error. The rod truss predicts the first several modes, but is less modally dense than the truth model.

Overall, improvements in the mesh refinement of each model type add more modes to the transfer function and improve the natural frequencies towards the true values for the model type. Increasing the number of modes for the BE or Timoshenko beams improves the accuracy of the natural frequencies calculated towards their respective continuous solutions. However, because the modes are off from the truth model at a larger error, the improvement of the mesh is only important if higher frequency modes are wanted in the stick model.

The rod truss cannot be refined, but with only one rod element per member, represents the truth model very well for the lower modes and the general slope of the transfer function.

The bar truss with one element per member can also be used to add a little more accuracy in calculating the fundamental modes.

Finally, increasing the mesh of the truss with beams approaches the truth model and the lower mesh trusses have errors with low orders of magnitude such that performance calculations can more accurately predict the true behavior of the system.

# Chapter 3

# ORIGINS TESTBED

## 3.1 Background

The Origins Testbed was conceived to provide a testbed for implementation of controlled structures technology of space telescopes [DeBlonk, 1996]. To achieve this goal, the testbed is designed to have dynamics, disturbances, performances and control similar to that of actual systems (NGST, SIM). Dynamic similarity refers to the modal density and similar fundamental modes. Additionally, the testbed employs control techniques similar to that employed on space telescopes.

## 3.2 General Description

The origins testbed (Figure 3.1) has four truss arms and one truss tower, which support the optical payload of the testbed, and a welded aluminum base that represents the bus of the system. The structure of the testbed is designed to have similarity to space telescopes designs: a large truss holding the optical payload, a bus holding the reaction wheels, and two flexible brass beams to simulate low frequency flexible modes caused by sunshields, solar arrays, large truss booms, etc.

Slewing is another feature of the testbed, again required in order to simulate space telescope operations. The doctoral thesis for a previous SSL student, Gregory Mallory, relied on the ability of the Origins Testbed to have different modes of operation resembling a

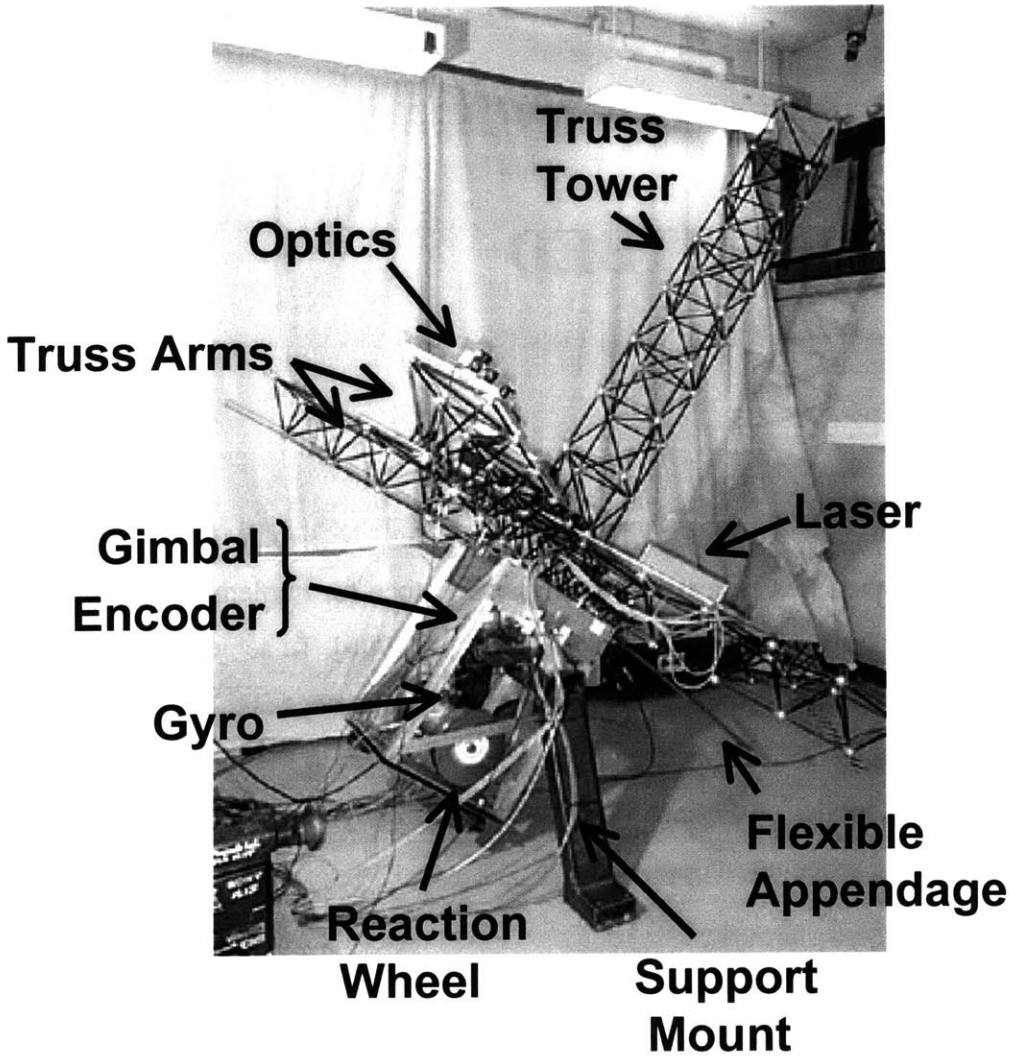


**Figure 3.1** Origins Testbed

space telescope such as slewing towards a desired star, acquiring a target, observing the target, and desaturating the reaction wheels [Mallory, 2000a]. The requirement to slew is satisfied by giving the testbed one rotational degree of freedom controlled by the reaction wheel and gimbal. The center of mass is at the center of rotation which is mounted to a rigid support structure via the gimbal. The reaction wheel has only one axis of control authority due to the mounting of the OT. The gimbal is used to desaturate the reaction wheels as thrusters would on actual spacecraft.

### 3.2.1 Optics

The Origins Testbed can perform both internal metrology for fine phasing, and the capture of simulated external science light for pointing control, using a single laser source. The payload of the testbed are the optical elements (such as relay optics, fast steering mirrors, delay lines, CCD (Charged Couple Device) camera) that are mounted on aluminum plates along the truss arms and on the top of the truss tower. Internal metrology laser light is split in two, directed along the two opposing truss arms and returned. For external light capture, the laser light is again split in two, sent along the length of the two opposing arms, then sent to an externally mounted mirror elsewhere in the lab, which reflects the light back to the testbed.

The optical train consists of a laser interferometer mounted on aluminum plates, which are themselves mounted on the truss arms. There are several different OPDs that are available to mimic different types of light paths for different types of telescopes. The beam is split into two and then recombined and collected by a CCD camera.

## 3.3 Modeling

Analytical models are physically-based models of a structure. They relate the physical parameters to the dynamics of the system. Measurement models are fit models to experimental data taken through system identification techniques. These are considered to be the more accurate representation of the plant dynamics. However, because measurement models do not relate the modes of the system to the physical parameters, any time the parameters or environment changes, another system identification (SYS ID) has to be done. Controllers based on measurement models can have very high authority since they accurately know the behavior of the system, but are not very robust, because there is no knowledge of how changes to the system will affect changes in the behavior.

Analytical models generally contain errors in the dynamics when first created. The masses of each element are easily determined, but stiffnesses are not as simple to capture. Though

tests can be done on the different elements to determine their stiffnesses, the assembled dynamics will be different than the dynamics of the individual elements. Additionally, when modal damping is used, engineers estimate the initial values for the damping coefficients based on experience as they cannot be directly measured [Bourgault, 2000]. Measurement models are helpful for updating analytical models by comparing the predicted performance with the test data. The physical parameters are treated as variables that are changed to minimize the error between the measurement model and the physical model. With an updated model, the physical parameters can be changed and 1-g conditions removed in order to study how the plant would behave in 0-g. With physical parameters matched to the ground system, this 0-g model is now more accurate than an analytical model updated without experimental validation.

There are two major classifications of errors: parametric and non-parametric errors. Parametric errors are due to incorrect information about the value of a parameter such as mass, density, inertia, Young's modulus, stiffness, or geometry. These errors are due to insufficient data. Mass determined from volume and density is less reliable than actual weight measurements. Relying on look-up tables for nominal parameter values is less accurate than testing the material properties. Parametric errors also include typographical errors during model coding.

Non-parametric errors are errors that cannot be traced to an incorrect parameter value and are analogous to a lack of necessary information. They are due to incorrect modeling assumptions such as poor mesh refinement and assuming that a highly non-linear structure can be modeled in a linear manner.

The following description of the model updating process comes from the work by Glease on the Middeck Active Control Experiment (MACE) [Glease, 1994]. Model updating can be broken down into three steps: engineering insight, automated updating, and closed loop updating. The largest improvement from the initial model to the final product comes from the engineering insight. This step reduces the non-parametric errors caused by wrong

assumptions. Engineering insight also reduces the parametric errors such that the modal parameters of the analytical model are easily paired with the experimental data.

A few considerations for the engineering insight stage are to:

1. Weigh all items to get the correct mass
2. Measure all items to get the correct dimensions
3. Conduct stiffness tests on elements
4. Ensure correct finite element is being used: rod, bar, beam, plate
5. Check typographical errors when entering in values
6. Correct constraints/boundary conditions
7. Improve mesh refinement
8. Check uniformity of units

The non-automated stage is complete when no more erroneous assumptions can be determined. The parametric errors are reduced to those which cannot be adequately measured. The result is a model that closely resembles the measurement model to small percentage errors. During the non-automated updating, the model can be compared to the experimental data or measurement model to see if the modeling is converging towards the truth model.

## 3.4 Modeling the Origins Testbed

The previous work done on the Origins Testbed [Mallory, 2000a] did not require a high fidelity analytical model. However, a few proposals for possible future work to be done on OT require an analytically based model to be made. One such possible experiment for the Origins Testbed is the application of isoperformance methodology created by Olivier de Weck for his doctoral research [DeWeck, 2001]. Experimental validation of a methodology like isoperformance on the Origins Testbed, requires a physical based, high fidelity, analytical model.

The truss arms each consist of five square pyramid bays with the base having 0.25 m sides. The truss tower consists of eight cube bays with 0.25 m sides. One face of the truss tower resembles the truss in the example problem in Chapter 2 (Figure 2.2 on page 47) with a total length of 2 m. Figure 3.2 shows a computer generated drawing of the truss structure. The gray regions on the truss indicate the location of optics plates.

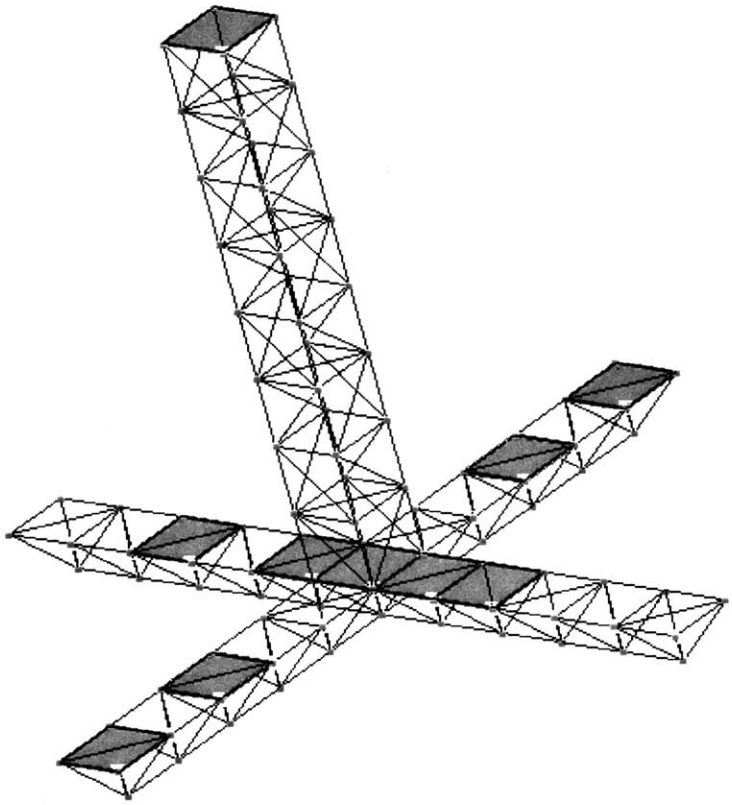

**Figure 3.2** Origins' truss structure

The truss struts are 9.5 mm (3/8") aluminum rods of 1.5 mm (0.058") thickness. They come in two different lengths, 0.25 m for the base of the square pyramid or cube bays, and 0.35 m for the diagonals of the square faces. At each node are 2.5 cm (1") hollow aluminum balls that the struts screw in to. However, in modeling the struts, they are assumed to

span the entire distance from node to node and are given an equivalent modulus of elasticity determined from previous experimental data [Gutierrez, 1999].

**TABLE 3.1** Truss struts

| Property | Value |
|---|---|
| material | aluminum |
| length of short strut | 0.25 m |
| length of long strut | 0.35 m |
| outer diameter | 9.5 mm (3/8") |
| thickness | 1.5 mm (0.058") |

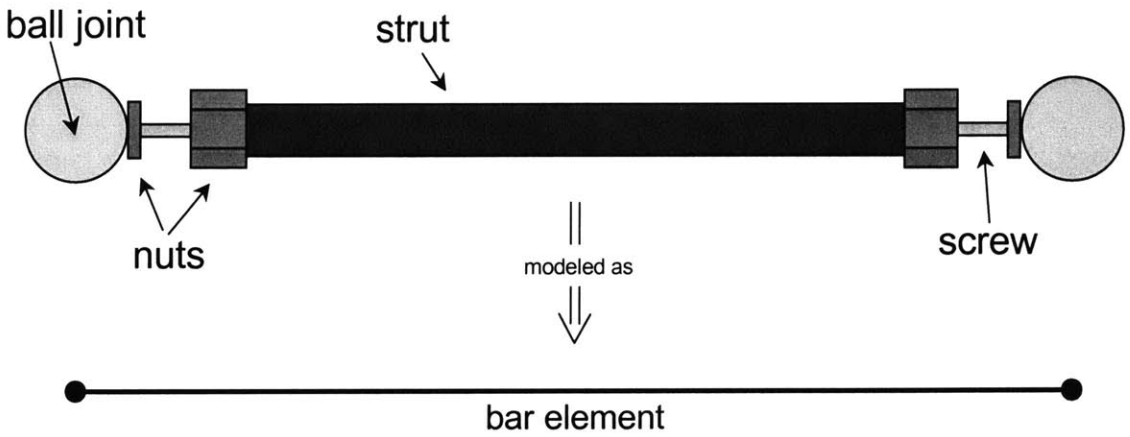


**Figure 3.3** Truss strut modeling [Mallory, 1998]

Because OT has already been built when the modeling began, the masses of each of the components cannot be weighed without taking the testbed apart. The struts masses are measured by weighing extra struts that are not mounted to the structure. The masses of the other components are determined either by calculating the mass via their dimensions and material density (for the plates and flywheel) or through published specifications for commercial-off-the-shelf (COTS) components (for the optical elements like the laser and CCD camera).

The bus portion holds the reaction wheel. The RWA consists of two steel wheels separated by an aluminum axial tube that contains the motors and tachometer for the wheels. The steel wheels are 0.2540 m (10.00") diameter and contain most of the weight around the rim. The axial tube is 0.4064 m (16.00") long, has a 0.141 m (5.56") outer diameter, and a 0.102 m (4.00") inner diameter. Inside the axial tube are two Aerotech, Inc. DC Servomotors Model 1075DC-02. They each weigh 3.3 kg, have a 0.1652 m diameter, are 0.177 m long and are placed axially at the ends of the tube.

**TABLE 3.2** Reaction Wheel

| Property | Value |
|---|---|
| wheel material | steel |
| wheel diameter | 0.2540 m (10.00") |
| axial tube material | aluminum |
| axial tube length | 0.4064 m (16.00") |
| axial tube outer diameter | 0.141 m (5.56") |
| axial tube inner diameter | 0.102 m (4.00") |
| motor make | Aerotech, Inc. |
| motor model | DC Servomotors 1075DC-02 |
| motor weight | 3.3 kg |
| motor diameter | 0.1652 m |
| motor length | 0.177 m |

The brass appendages dimensions are listed in Table 3.3. They are modeled using plate elements.

**TABLE 3.3** Brass Appendages

| Property | Value |
|---|---|
| material | brass |
| thickness | 3.175 mm (1/8") |
| width | 0.102 m |
| length | 1.0 m |

The base structure is constructed out of aluminum plates and beams. The top and bottom plates are 0.50 m squares that are 6.4 mm (1/4") thick. At each corner holding the plates together are square hollow beams 0.737 m long. The outer length of the square cross section is 0.038 m (1.5") with a thickness of 3.175 mm (1/8"). On two opposing sides are plates that cover the top fourth portion of the side with the same thicknesses as the top and bottom plates. There are diagonal beams across the face of each side of the base. On the sides with the plates, the beams are flat and rectangular and reach only halfway up the side; they have the same thickness as the other plates. On the sides without plates, the diagonal beams are square hollow beams with the same cross section as the vertical support beams. The top, bottom, sides and the flat diagonal beams are modeled using plate elements. The vertical and diagonal square-cross-sectional beams are modeled using bar elements.

**TABLE 3.4** Base Frame

| Property | Value |
|---|---|
| material | aluminum |
| top and bottom plate side | 0.50m |
| top and bottom plate thickness | 6.4mm (1/4") |
| vertical support beam length | 0.737m |
| vertical beam cross section outer length | 0.038m (1.5") |
| vertical beam cross section thickness | 3.175mm (1/8") |
| side plate depth | 0.152m |
| side plate thickness | 6.4mm (1/4") |

Attached to the bottom of the base is a steel plate and 2 lb and 3 lb dumbells that act as counterweights in order to bring the center of gravity to the center of rotation. Without these counterweights, the structure would be top-heavy and unstable. The steel plate has the same area as the base aluminum plates. The thickness of the steel is 4.76 mm. The counter-weights are attached at four points under the steel plate via thick screws. Using the screws allows the vertical positioning of the weights to be fine-tuned to get the center

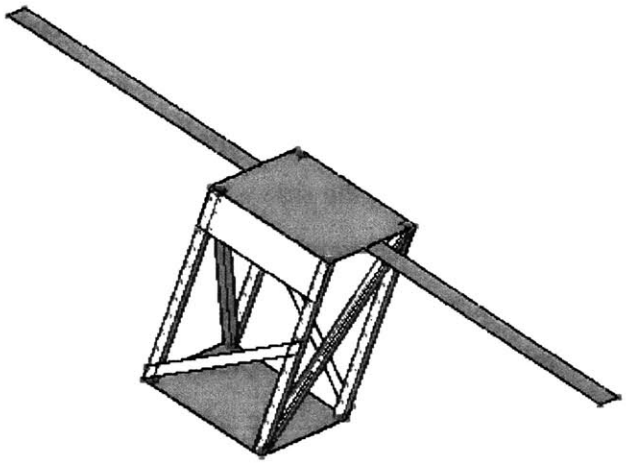

**Figure 3.4** Base

of gravity as close to the center of rotation as possible. Because of the fine-tuning process, the vertical positioning of each of the five weights are all different. The five points are arranged so that there is one weight at three corners and one in the middle as shown in Figure 3.5. Table 3.5 lists the weights that are at each corner numbered as in Figure 3.5. The steel plate is modeled as a plate element. The steel screws holding the counterweights are modeled as bar elements and the counterweights are modeled as point masses.

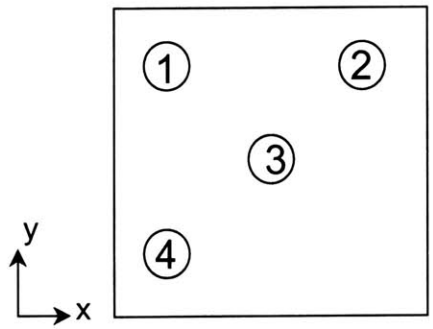


**Figure 3.5** Schematic of counter-weight placement looking down on top of the base

**TABLE 3.5** Counter-weight masses

| Weight ID # | mass [kg] |
|---|---|
| 1 | 0.907 |
| 2 | 1.23 |
| 3 | 1.36 |
| 4 | 0.978 |

The flywheel and optical elements are modeled as a point mass. Only the optics with significant mass are added: the laser, the CCD and the mini-shaker. The inertia contribution of the optical point mass local inertia were considered negligible compared to the inertia contributed by their mass removed from the system center of rotation.

**TABLE 3.6** Point Masses

| Name | mass (kg) | $I_{xx}$ (kg $m^2$) | $I_{yy}$ (kg $m^2$) | $I_{zz}$ (kg $m^2$) |
|---|---|---|---|---|
| RWA | 22.3 | 0.613 | 0.613 | 0.199 |
| laser | 3.4 | - | - | - |
| remote receivers | 0.126 | - | - | - |
| Dalsa CCD | 0.85 | - | - | - |
| Mini-shaker | 1.1 kg | - | - | - |

Material properties for the aluminum, steel and brass elements were chosen from look-up tables.

**TABLE 3.7** Material Properties [Gere, 1997]

| Material | Young's Modulus (Pa) | Poisson's ratio | Mass Density ($kg/m^3$) |
|---|---|---|---|
| Aluminum | 7.2 E 10 | 0.33 | 2800 |
| Brass | 1.00 E 11 | 0.34 | 8500 |
| Steel | 2.00 E 11 | 0.32 | 7860 |

### 3.4.1 Model Evolution

The modeling of the Origins Testbed starts with a low fidelity model. The first step is to model just the truss structure as shown in Figure 3.2 but without the plates. The strut dimensions and aluminum material values are listed in Table 3.1 and Table 3.7, respectively. No constraints are added to ensure that the analysis resulted in six rigid body modes. Figure 3.6 shows the first four flex modes (non-rigid body modes) of the truss. Both the undeformed and the deformed trusses are overlaid in the same figure. The deformed structure represents the total deflection for the mode shape.

At each major model improvement, the model name is incremented by one. The truss-only model shown in Figure 3.6, is Origins1. The next several iterations add the basic shape of the base to the truss. Figure 3.7 shows the image of Origins3, which includes the truss, truss plates, base and brass beams.

Modal analysis on iteration 3 represents the modes of the entire testbed compared to iteration 1. The local modes of the truss structure shifts to higher frequencies since they are now constrained by the base at five points and have the truss plates on the arms and the top of the tower. Iteration 3 also includes the dominant 2 Hz mode of the brass beams. Again, no constraints were added so that the presence of six rigid body modes can be checked to easily ensure that the modeling is proceeding without major modeling errors. Figure 3.8 shows two examples of the mode shapes of Origins 3. Figure (a) is the mode shape of the local brass 2 Hz mode. Figure (b) is the mode shape of a higher frequency global mode that includes the dynamics of the entire structure.

Origins 7 is the first iteration to add constraints and the input/output nodes for conducting a system ID. Other improvements between iterations 3 and 7 are the addition of the flywheel and optical point masses, attached to the structure via rigid body elements, and the addition of the steel plate.

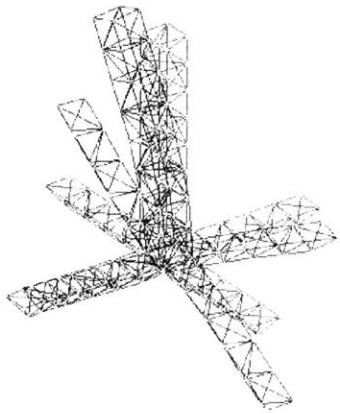

48.9 Hz

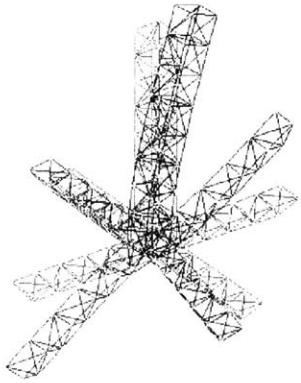

49.2 Hz

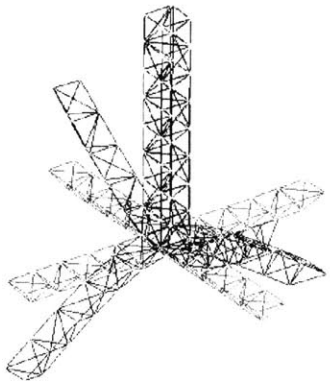

66.5 Hz

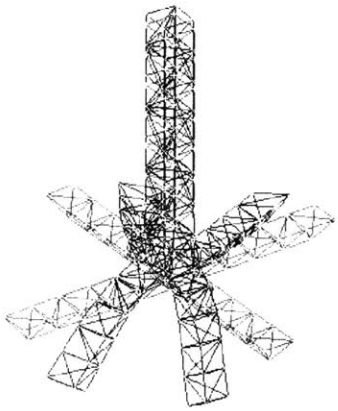

74.8 Hz

**Figure 3.6** Truss only

The rotation axis on the testbed is along the x axis, perpendicular to the longitudinal axis of the brass appendages. The gimbal is located underneath the top base plate and weight of the testbed is supported at three points along the axis of rotation: at each side plate and by the gimbal in the center. These supports are modeled as nodes which are constrained in all degrees of freedom except for the rotation about the x axis. Two of the nodes coincide with nodes of the side plate elements, but the node in the center, representing the gimbal, is not associated with any structural element in the model. It is attached to the structure via

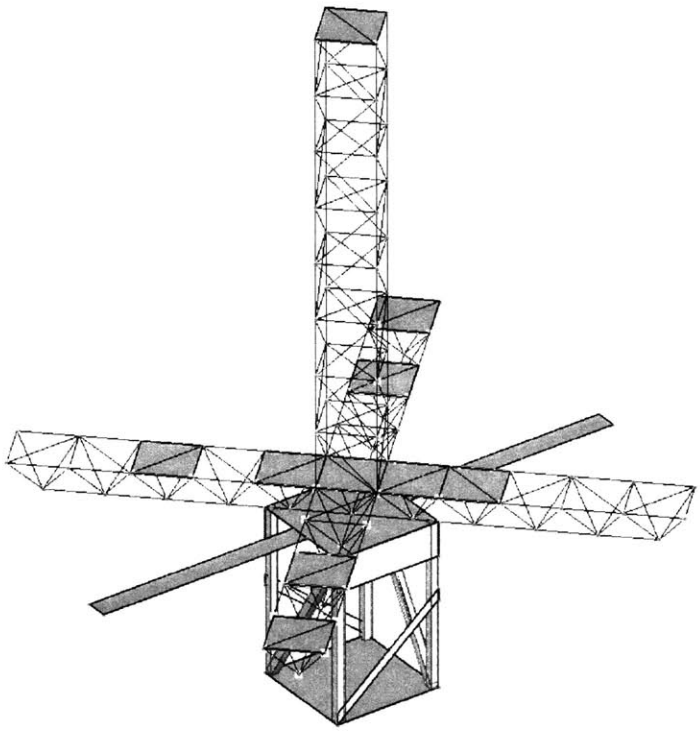

**Figure 3.7** Computer image of Origins Testbed - iteration 3

a rigid body element connected to the top of the base. Figure 3.9 shows a schematic of the constraint locations.

The iterations between 7 and 11 are detailed improvements and do not involve any major changes in assumptions, but mainly parameter values or meshing. The truss member elements are changed from rods to bars in order to refine the truss mesh from one element per member to two. The counterweight masses are added below the steel plate. The property values of the truss members and brass appendages are updated from the initial table values to values calculated in previous experiments. A number of corrections are made, such as the location of the steel plate below the base, the geometry of the truss tower, and the definition of the beam orientation vectors.

Figure 3.8 (a)
Mode #1
Brass Mode
1.65 Hz

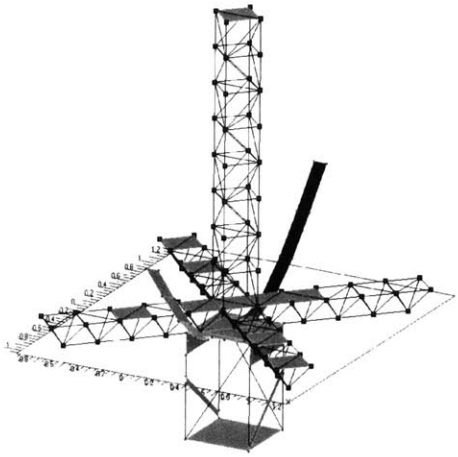

Figure 3.8 (b)
Mode #15
First Global Mode
36.5 Hz

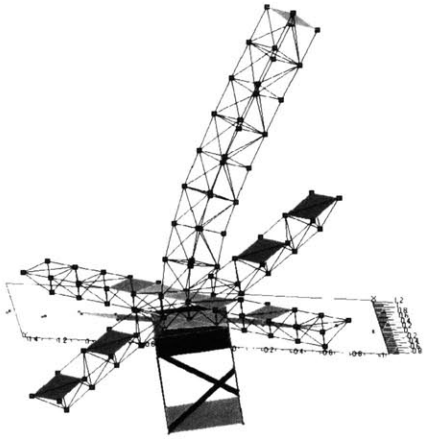

**Figure 3.8** Two modes of Origins 3

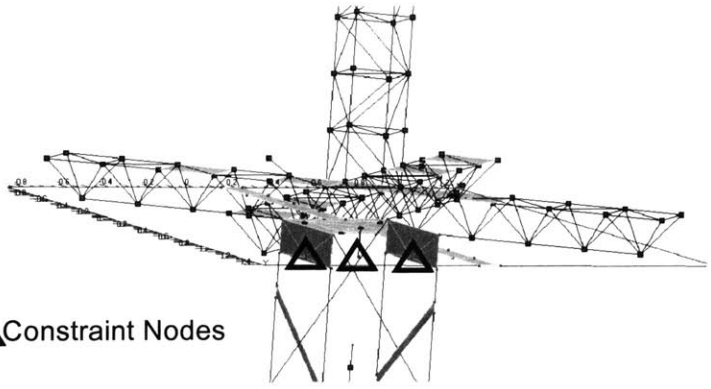


**Figure 3.9** View of constraints on Origins 7

The modes of Origins 11 are listed in Table 3.8. There is one rigid body mode left after constraining the testbed in the x-rotational degree of freedom. The first four flex modes are local modes of the brass appendages. The first global mode of the testbed is mode six at 14 Hz. This mode and two other representative mode shapes of OT version 11 are shown in Figure 3.10.

**TABLE 3.8** Origins 11 Modes

| | | Frequency | |
|---|---|---|---|
| **Mode #** | **Description** | **[rad/s]** | **[Hz]** |
| 1 | RBM | | |
| 2 | Brass | 11.3 | 1.81 |
| 3 | " | 11.7 | 1.87 |
| 4 | " | 69.4 | 11.0 |
| 5 | " | 69.5 | 11.1 |
| 6 | Global | 87.8 | 14.0 |
| 7 | " | 125 | 19.9 |
| 8 | Brass | 125 | 19.9 |
| 9 | " | 125 | 19.9 |
| 10 | Global | 148 | 23.6 |
| 11 | " | 155 | 24.7 |
| 12 | " | 183 | 29.2 |
| 13 | " | 184 | 29.4 |
| 14 | Brass | 190 | 30.3 |
| 15 | " | 190 | 30.3 |

### 3.4.2 System Identification

A SYS ID was performed on the Origins Testbed by Olivier de Weck and Gregory Mallory in summer of 2000 (Figure 3.11). The inputs are unit intensity white noise entered at the reaction wheel and at the gimbal. The white noise is simulated by means of randomly generating the voltage driving the reaction wheel motors and the gimbal motors. There are three outputs from the system. The first is the angular displacement of the testbed mea-

Figure 3.10 (a)
Mode #6
First Global Mode
(non-brass mode)
truss rocking about x-axis
14.0 Hz

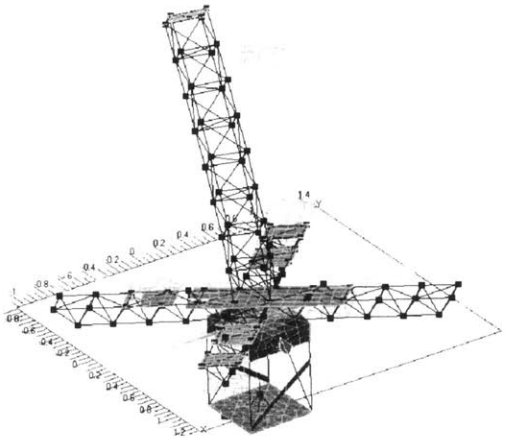

Figure 3.10 (b)
Mode # 11
truss arm twisting
24.7 Hz

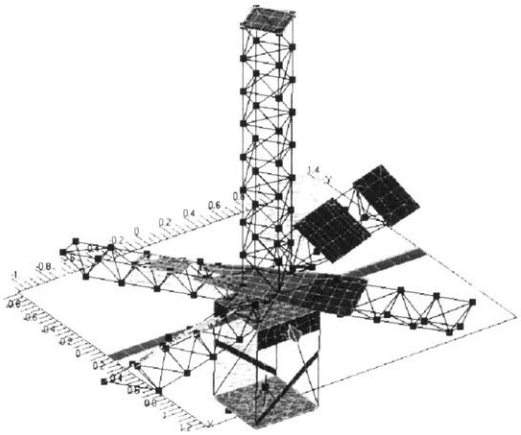

Figure 3.10 (c)
Mode #19
truss tower and arms bending
42.2 Hz

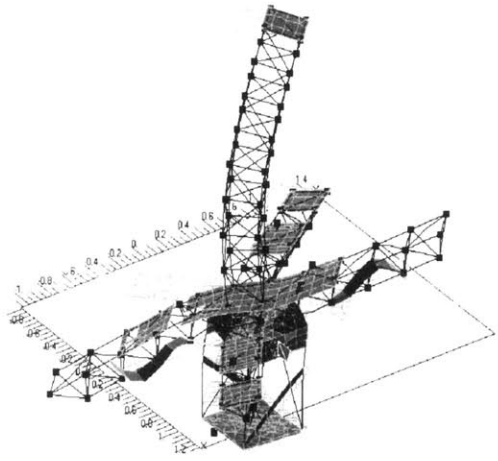

**Figure 3.10** Origins 11 Mode Shapes

sured by angle encoder located at the gimbal node. The second output is angular velocity of the testbed measured by the rate gyro, which is mounted on top of the reaction wheel axial tube. The third output is the differential path length (DPL) of the internal laser metrology system.

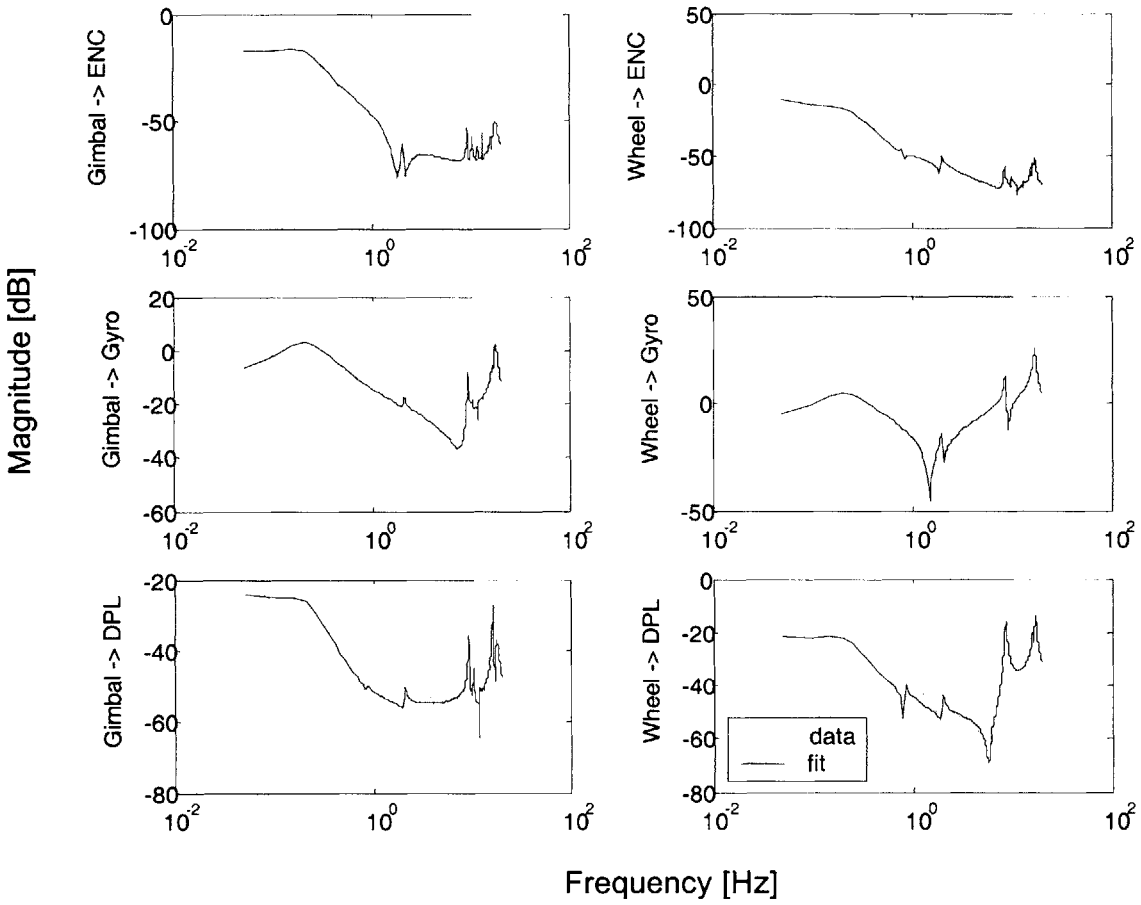


**Figure 3.11** System Identification of the Origins Testbed - Experimental Data

The transfer functions of the experimental data are shown in Figure 3.11. The light, noisier curve is the experimental data and the smoother, dark curve is the measurement model. The x-axis is the frequency in Hz and the y-axis is the magnitude in dB. An initial look at the information from the transfer functions shows a prominent 2 Hz mode in all 6 input-

output pairs. This mode is the low frequency dynamics of the brass appendages and coincides with their first transverse bending mode.

From the figure, we can see that the bandwidth of good data is limited by the sensors. The first row of plots, the angle encoder output, has noise at high frequencies due to the inaccuracies of the encoder. The only mode observable within the sensor bandwidth is the 2 Hz brass mode. The second row, rate gyro output, has non-structural low frequency behavior at approximately $10^{-1}$ Hz due to the limits of the rate gyro.

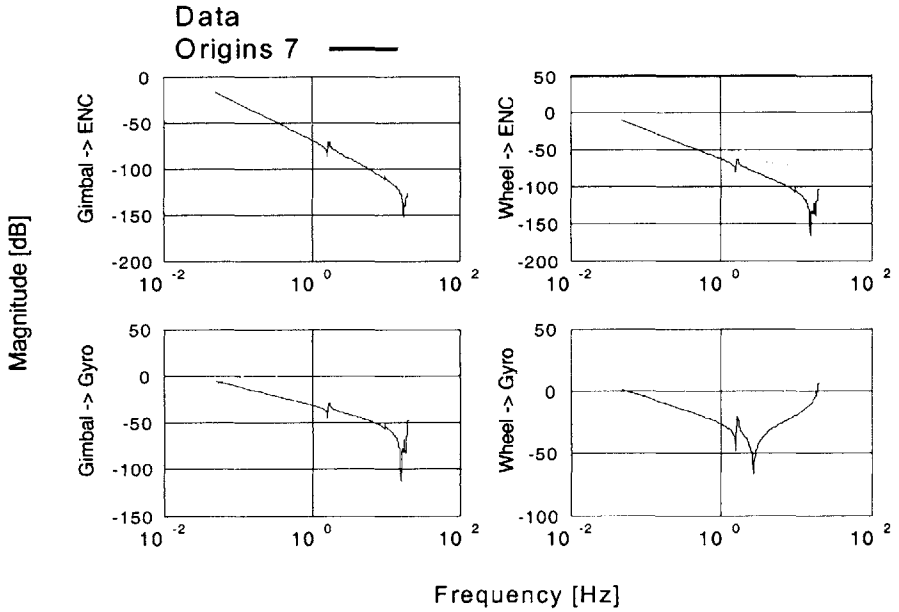


**Figure 3.12** Origins 7 Transfer Functions

The inputs and outputs of the analytical model are chosen to correspond with the first four transfer functions. The DPL transfer functions are not considered in this analysis. A state-space model of the OT is created based on the modal analysis results. Model damping of 0.5% is applied to all modes. The transfer functions created via analytical models are in units of radians/Newton-m or (rad/s)/N-m (displacement output / moment input). However, the SYS ID transfer functions are in the units volts/volts. Therefore, the coefficients

entered in the performance matrix, C, unit conversion factors. The resulting transfer functions for Origins 7 are shown along with the SYS IS data in Figure 3.12.

The 2 Hz brass mode is visible in the model although the numerical value of the natural frequency is slightly low. The general shape of the transfer functions resemble the experimental data except at the limits of the angle encoder data. All four plots show a discrepancy in the gain of the analytical model from the experimental data. The comparison of the two transfer functions with the gyro as the output show that the model is missing several poles and zeros.

Figure 3.13 shows the transfer functions of OT version 11. The gain of the two angle encoder transfer functions are improved from version 7, and overlay the experimental data more closely. The gain is still off from the gyro transfer functions and may be due to inaccurate conversion factors. The poles and zeros missing from the wheel-gyro transfer function in version 7 appears in version 11, with the exception of one zero after the 2 Hz mode.

## 3.5 Summary

Table 3.9 lists an overview of all the improvements made on the Origins Testbed throughout the model updating. Though the testbed has been updated significantly from the initial truss-only model, it still requires more updating to be considered an accurate representation of the Origins Testbed dynamics. The analogy of the model updating procedure to the model fidelity evolution still holds without a completed analytical model.

Although the Origins Testbed is complete, there are modeling errors in the analytical model. The errors in the OT model are from both incorrect assumptions and parameter errors. Although the Origins 11 model does not match the system identification data as closely as desired, it is a relatively high fidelity model and is more accurate than a model based on an incomplete design. The slopes of the transfer functions and the calculation of the fundamental modes are more accurate than for a low maturity design. The stage of the origins model is akin to the rod truss or low mesh bar truss of the sample problem.

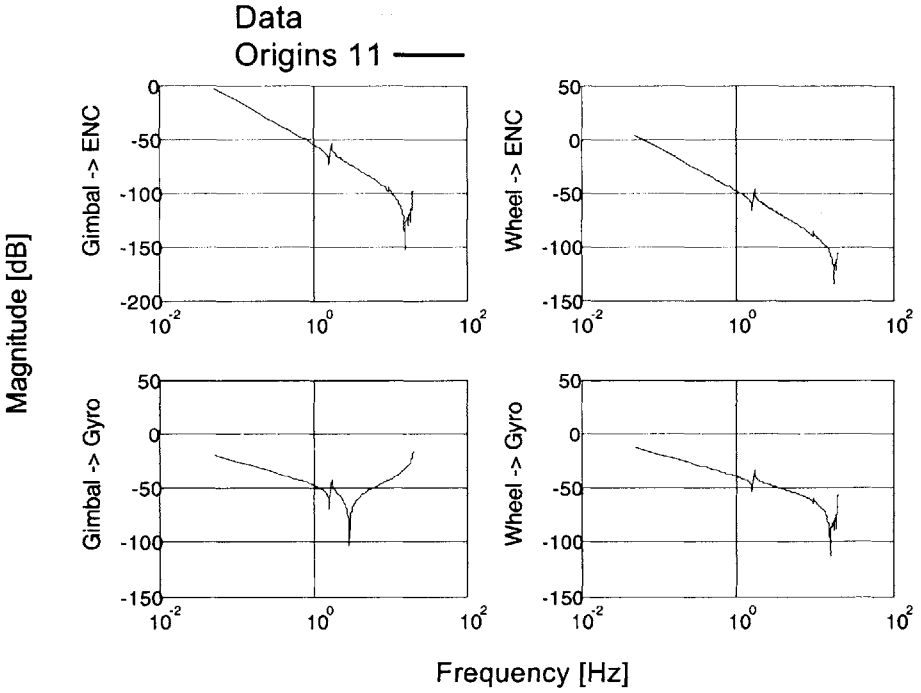


**Figure 3.13** System ID of Origins version 11

**TABLE 3.9** Overview of Origins Model Evolution via Engineering Insight

| Model Version | Updates |
|---|---|
| 1 | truss only |
| 2 | add base plates and truss nodal masses |
| 3 | add base beams and truss plates |
| 4 | add flywheel mass, increase mesh of brass beams |
| 5 | add optical point masses: LASER, CCD, and minishaker |
| 6 | add steel plate |
| 7 | add constraint nodes, input/output nodes and constraints |
| 8 | change truss members from rods to bars<br>corrected tower truss geometry |
| 9 | added counter-weight point masses, added steel screw (one was missing), updated brass properties from previous analysis of brass, updated strut properties from previous analysis of struts, refine mesh of brass, base and truss plates, corrected truss nodal masses, corrected the location of the steel plate |
| 10 | refined truss plate geometry, redefined rigid body elements |
| 11 | correct bar orientation vectors, refine truss member mesh |

# Chapter 4

# ARGOS

The ARGOS (Active Reconnaissance Golay-3 Optical Satellite) testbed is a ground based testbed designed to demonstrate modular Golay-3 technology. It is the project of an undergraduate design class called CDIO (Conceive, Design, Implement, Operate) and is scheduled for completion by the end of the spring term of 2002. Although the multiple aperture array technology concept has been demonstrated by observatories such as the Large Binocular Telescope (LBT), the contribution that ARGOS provides to the field is in its modular design and implementation of fizeau beam-combining on a rotating inertial frame. Currently, the goal of ARGOS is to image the International Space Station (ISS) while ARGOS is slewing. If this main objective is not completed, however, there are lower levels of mission success criteria as shown in Table 4.1.

**TABLE 4.1** Mission Success Criteria (from PDR)

| Level of Success | Criteria 1 | Criteria 2 | Criteria 3 |
|---|---|---|---|
| Minimum | Slew while keeping moving object in FOV | Incoherent imaging | Image of a celestial object of known feature scale |
| Full | Slew while keeping ISS in FOV | Coherent imaging | |

## 4.1 Description of ARGOS

The following description of ARGOS contains an overview of the subsystems relevant to its structural design and a description of the frozen design iteration for the disturbance analysis to follow in the next section. The information on the subsystem designs are based primarily on the Preliminary Design Review (PDR) of May 2001 [CDIO, 2001], with the exception of a few key subsystem design changes that have taken place since PDR.

### 4.1.1 Architecture

ARGOS is a ground based testbed that resembles the behavior of a space based system. As such, most of the design decisions are made as though the testbed will be space-borne to demonstrate flight capabilities of the design concept. However, certain key design features are modified in order for the testbed to function on ground. The first important difference between the two environments is gravity. The space based design does not have to support its weight nor deal with the offset between the center of gravity and the center of rotation. The second important constraint is the time and cost constraint of the CDIO environment. The testbed, to be completed by the end of spring 2002, will be less redundant and simpler than a true space telescope.

The ideal architecture for the space based system is a single function distributed system. The telescope is divided into three subapertures, each holding one collector telescope, and a combiner module. The combiner module is what the subapertures dock to and where they send their light for combining. Each of the three subapertures has its own fully independent bus with modular subsystems (power, computer, RWA, etc.) to allow separate launches and independent docking to the center bus.

The ground system architecture is modified from the space system and is a single-function monolithic design, where monolithic refers to the subsystem functions. All subsystems are modularized for simple interfaces, but complete subsystems are not placed in all three subapertures. All three subapertures are required for the entire system to function because

only one of each subsystem (such as computer, communications system, and reaction wheel assembly) will be placed on the testbed. This simplification is justified because the technological challenge and objective of ARGOS is the modularity of the optics not the redundancy of subsystem. The modularity refers to the ability to remove and replace the subapertures from the center bus and the ability to remove and replace the subsystems, such as the batteries, computers and communications equipment.

### 4.1.2 Optics

This section describes the key components of the optical train and briefly discusses the optical design. The optical design requirements are derived from the mission objectives. In order to be able to image the ISS during its orbit, the passive optics must meet the following requirements:

1. 0.35 arc second angular resolution or better
2. Science light in the visual spectrum
3. less than l/10 wave error
4. greater than 0.65 encircled energy
5. greater than 4 minute field of view
6. greater than 0.03 second integration time

A commercial off-the-shelf telescope, the Takahashi Mewlon 210, serves as the subaperture. It is a Dall-Kirkham type reflecting telescope with an elliptical primary mirror and spherical secondary mirror. The main advantage of the Dall-Kirkham telescope is that spherical aberration is eliminated. Spherical aberration causes the light to not focus at a single point. Additionally, the telescope does not have a correcting lens at the entrance and, therefore, most of the weight of the telescope is from the primary mirror at the base. The lack of a correcting lens makes the Takahashi less heavy than a similar sized Schmidt-Cassegrain telescope. The Takahashi-brand telescope is chosen primarily for its superior surface accuracy. The important properties of the Takahashi are listed in Table 4.2.

**TABLE 4.2** Takahashi properties

| Property | Value |
|---|---|
| Weight | 8 kg |
| Effective Aperture | 210 mm |
| Primary Mirror | 220 mm f/4 |
| Secondary Mirror | 65 mm f/2.9 |
| Tube Diameter | 244 mm |
| Tube Length | 700 mm |

The three Takahashi telescopes are configured into a Golay-3 configuration: 120 degrees apart about a beam combiner in the center of the array. The radius of the circle through the center of the subapertures is 19.185 cm. This configuration is necessary to achieve the required 0.35 arcsecond angular resolution. The Golay-3 configuration is shown in Figure 4.1.

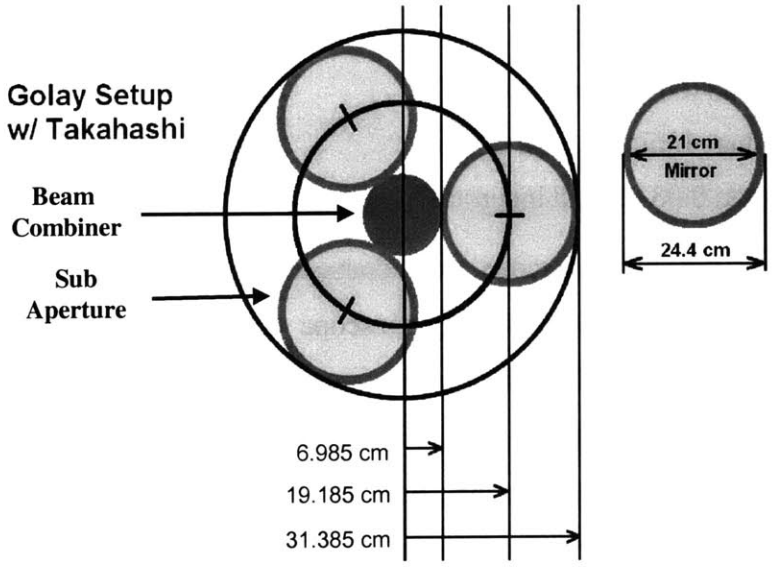


**Figure 4.1** Golay-3 configuration

Relay optics send the light from the subaperture to the beam combiner and include actuators to compensate for errors in the light path (wavefront tilt, beam shear, optical path-

length difference) The elements of the optical train usually include a collimator, fold mirror, optical delay line, and fast steering mirror. The layout of the relay optics for ARGOS is illustrated in Figure 4.2; the elements of the optical train are numbered in order, 1-8, and the dimensions shown are in mm. Table 4.3 lists the relay optics and the displacement between them. The displacements listed for optic n are from the center of optic n-1 to the center of optic n. The only exception is the displacement listed from the collimator to the first fold mirror.

**TABLE 4.3** Relay Optics[a]

| # | Optic | Δx [mm] | Δz [mm] |
|---|---|---|---|
| 1 | Collimator | n/a | n/a |
| 2 | Fold Mirror 1 | 0 | -70.0 |
| 3 | Fold Mirror 2 | -70.0 | 0 |
| 4 | Fold Mirror 3 | 0 | 35.0 |
| 5 | Fold Mirror 4 | 242.7 | 0 |
| 6 | Beam Combiner Primary | 19.2 | -95.0 |
| 7 | Beam Combiner Secondary | 0 | 75.0 |
| 8 | CCD | 0 | 86.0 |

a. The displacements listed are the distance between the bottom of the telescope to the first fold mirror.

The collimator is the only refractive optic used in the telescope. It converts the focusing light exiting the Takahashi telescope into collimated light with a diameter of 21 mm. The collimator is placed within and supported by the Takahashi telescope. The fold mirror, delay line and fast steering mirror are flat mirrors actuated by PZTs and voicecoils to control the optical path to compensate for jitter in the structure. The first three fold mirrors are placed under the Takahashi on an optics bench. The light from the optics bench is then sent from the telescope to the center bus, which holds the last fold mirror, the beam combiner and the CCD.

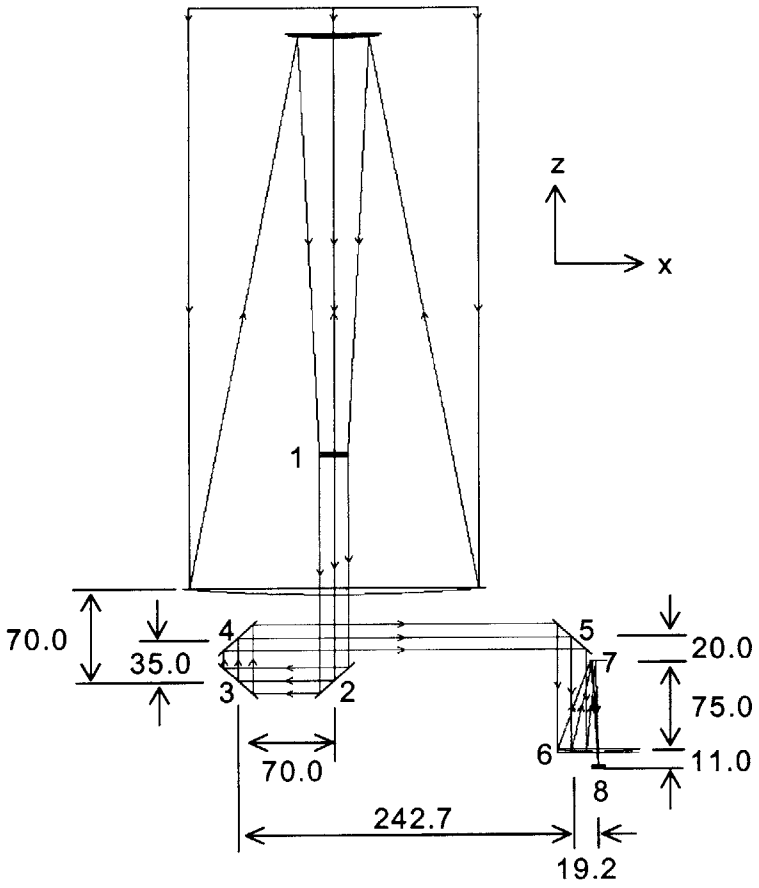


**Figure 4.2** Relay Optics Schematic - dimensions in mm

The beam combiner is sized to obtain the desired 1:10 compression ratio. The beams striking the surface of the combiner primary mirror must have the same configuration as the Golay-3 subaperture configuration, at $1/10^{th}$ scale. To obtain this degree of compression, the minimum optical radius of the primary mirror of the beam combiner must be 29.685 mm. The important dimensions of the beam combiner are listed in Table 4.4.

**TABLE 4.4** Beam Combiner

| Parameter | Value |
|---|---|
| Diameter of single beam | 21 mm |
| Center of beam to center of beam | 33.2 mm |
| Minimum optical radius of combiner | 29.685 mm |

The CCD camera collects the combined science light for imaging the science target. The field of view requirements determine the size of the CCD. Other requirements, such as the speed of data output, determine the quality of CCD necessary. These other requirements affect the ability for ARGOS to capture the ISS while slewing, but does not affect the structural design. The PDR choice of CCD is the Apogee AP10, which has dimensions of 177.8 x 177.8 x 76.2 mm

### 4.1.3 Attitude Control System

The sensors and computers on ARGOS must be able to determine the orientation of ARGOS with respect to the earth, and then find and slew to the science target autonomously. The ability to slew to the target in an inertial reference frame is one of the main features of ARGOS that sets it apart from other current sparse aperture observatories. Slewing is achieved by mounting the testbed on an air bearing and using reaction wheels to provide attitude control.

The air bearing works by blowing air under the object that it supports, which lifts the object enough to prevent contact with the air bearing stand. The mass of ARGOS is limited to 26 kg by the weight capacity of the air bearing. The layout of the optics in the center bus is constrained by the presence of the air bearing at the center of the structure. Figure 4.2 shows that the subaperture optics are all above the plane of the CCD. The CCD must be mounted above the air bearing and thus above the center of rotation. The rest of the optics are then also above the center of rotation. The weight of the optics must be countered by placing weight below the airbearing. Therefore, the subsystems will be placed below the optics. However, when ARGOS tilts, the air bearing stand must be able to clear any structure placed below the center of rotation.

The torque authority of the RWA on ARGOS is required about three axes. The sizing of the RWA depends upon the inertia of the structure and the desired slew rate. The RWA is expected to contribute significantly to the total mass of ARGOS and since the total weight that the air bearing can support is limited, the final design must minimize the size of the

RWA. The rotational inertia of the system is divided into two components: the inertia about the principal axes (the center of gravity) and the displacement of the center of gravity from the center of rotation (parallel axis). Minimizing the inertia about the principal axes is done by keeping the massive subsystems as close to the center of rotation as possible. To reduce the second component of inertia (from the parallel axis theorem) to zero, the center of gravity (CG) and the center of rotation must be at the same point. However, manufacturing tolerances in the structural material and inability to distribute the weight of the subsystems (computers, batteries, GPS receiver, etc.) limit how close these two points can be placed passively. The requirement on the structural design is to get position the CG within a 1 mm radius of the center of rotation. The separation is reduced further through an active balancing system.

### 4.1.4 Structure

The structure is designed to support the optical train, to hold the subsystems together, and to isolate the optics from the disturbance. The primary disturbance is the vibrational noise from the RWA, but the optics are also sensitive to heat from the electrical components. The structure must also meet the modularity requirement that, like the inertial reference frame, sets ARGOS apart from other current observatories.

Figure 4.3, Figure 4.4, and Figure 4.5 show the structural design of ARGOS as of the PDR. The telescope collar is the mount that supports the Takahashi. The component cage supports the subsystems and is designed such that the subsystems can be arranged on a rack that easily slides on and off the cage. The optics bench supports the first three fold mirrors of the optical train. The center bus holds the fourth folding mirror, the beam combiner and CCD camera. The center bus is also the attachment point between the structure and the air bearing.

Figure 4.4 illustrates the clearance of the air bearing between the component cages. The air bearing stand must be able to clear the structure so that ARGOS can tilt in a full 60 degree cone off vertical. This clearance requirement caused the design to have the cages

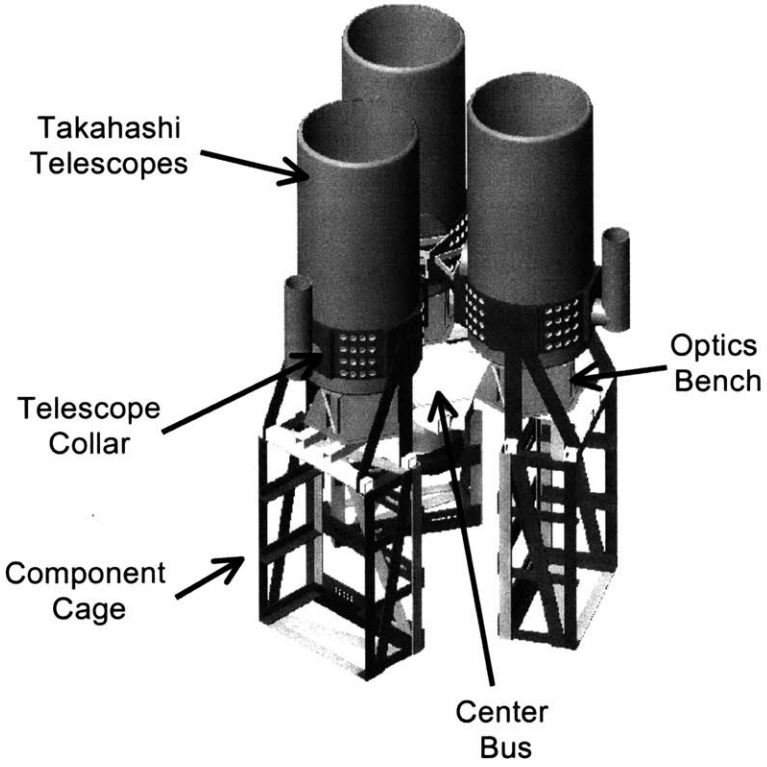


**Figure 4.3** ARGOS structural design

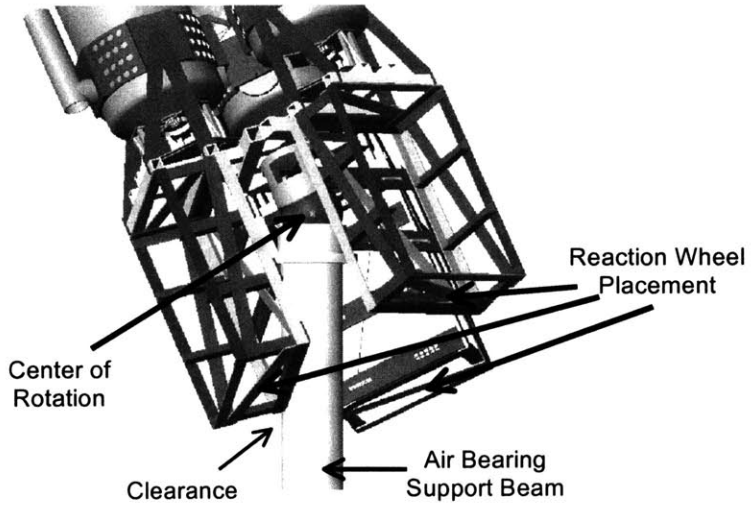


**Figure 4.4** Air Bearing Support Beam Clearance

placed radially outward from the center of rotation. The RWA assembly is distributed among the three subapertures. One wheel will be placed on the bottom rack of each cage for three wheels total.

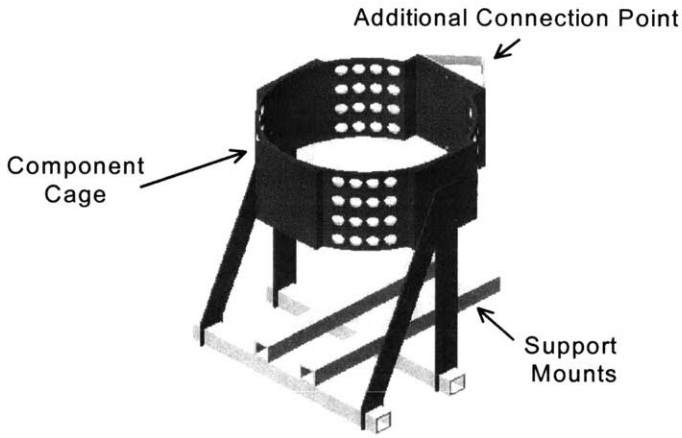


**Figure 4.5** Telescope Collar

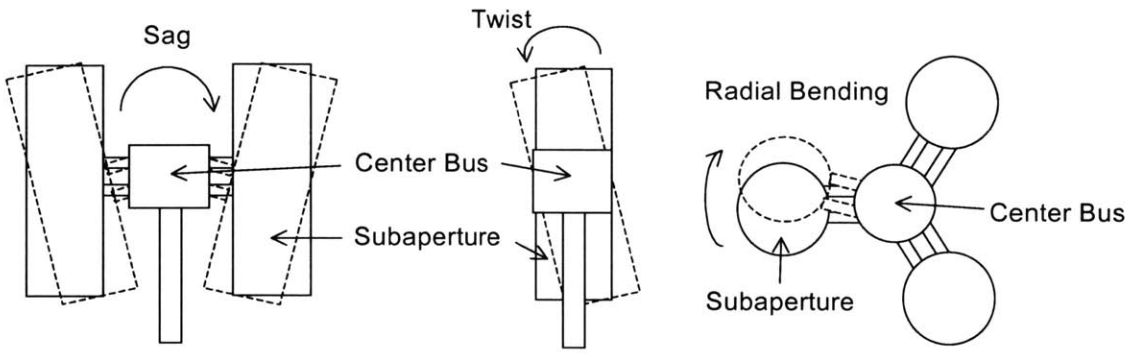


**Figure 4.6** The three bending directions the support beams must counter

Figure 4.5 shows the telescope collar without the Takahashi. The collar is designed to interface with the Takahashi's dove-tail collar mount so that the weight of the telescope is supported as recommended by the manufacturer. The support mounts are the weight bearing members of the subaperture design and connect the subapertures to the center bus. The support beams side by side will add bending stiffness to reduce radial bending as shown in

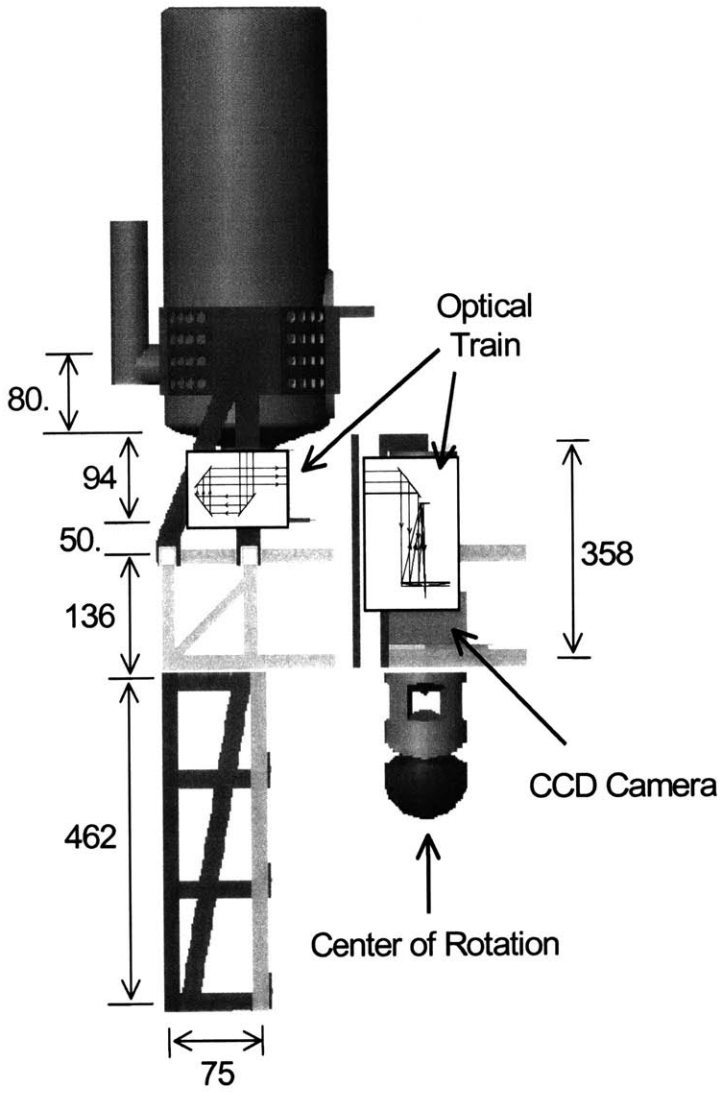


**Figure 4.7** Side view of subaperture and center bus geometry

Figure 4.6, which is the bending about the z-direction (z points vertically upwards). A second set of support beams below the collar (not shown in Figure 4.5) will increase the bending stiffness in the "sag" direction. The optical performance metrics (wavefront tilt, OPD) are most sensitive to the sag direction. In order to increase the sag stiffness more, another connection point for the subaperture has been added at the collar. Each collar will connect to the other two above the center bus. Thus the assembly of ARGOS involves

sliding the subaperture and collar together via the support beams, tightening the support beams with a screw, and pinning the collar connection points together.

Figure 4.7 shows the side view of one subaperture and the center bus. The figure illustrates how the optical train fits into the design.

**TABLE 4.5** Structural Dimensions

| Dimension | Value [mm] |
|---|---|
| Vertical distance between optical bench and bottom of Takahashi | 95. |
| Vertical distance between center of collar and top pair of support beams | 315 |
| Horizontal distance between pair of support beams | 50. |
| Vertical distance between support beam pairs | 136.5 |
| Vertical distance between center of collar and bottom of Takahashi | 80. |
| Total height of center bus | 358 |
| Length of one side of center bus hexagonal optics plate | 116 |
| Height of component cage | 462 |
| Width of component cage | 300. |
| Depth of component cage | 150. |

Table 4.5 lists the principal dimensions of the structure. The Golay-3 layout of the telescopes (Figure 4.1) is used to determine the positions of the subapertures with respect to the center bus. The vertical dimensions of the subaperture with respect to the center bus are designed based on the optical train positions listed in Table 4.3.

## 4.2 ARGOS Integrated Model

ARGOS is currently between the preliminary design phase and the critical design phase and thus all modelling is still low-fidelity. Though the architecture has been chosen, the

design of the subsystems are still evolving. The structural design is dependent upon the other subsystems and must be kept versatile to accommodate refinement of subsystem requirements as they become better defined during the design process. However, in order to perform a disturbance analysis at this stage, a design iteration must be chosen for analysis, i.e. frozen, at the design matures. The disturbance analysis at this early stage will determine if the design is adequate or needs major improvements.

### 4.2.1 Structural Dynamics

Because ARGOS is in a low fidelity design stage, the analytical model created will be analogous to the stick models of Chapter 2. For the stick model, only the main structural components, input nodes and output nodes are needed. Figure 4.8 shows the finite element model of the assembled structure and Figure 4.9 shows the details of one subaperture and the center bus including the optics nodes and the reaction wheels.

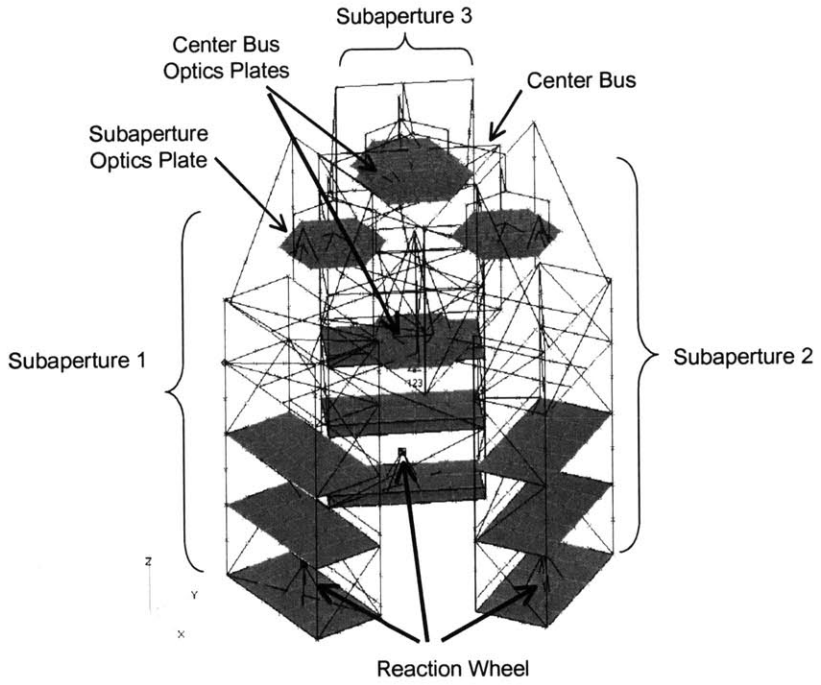


**Figure 4.8** Assembly

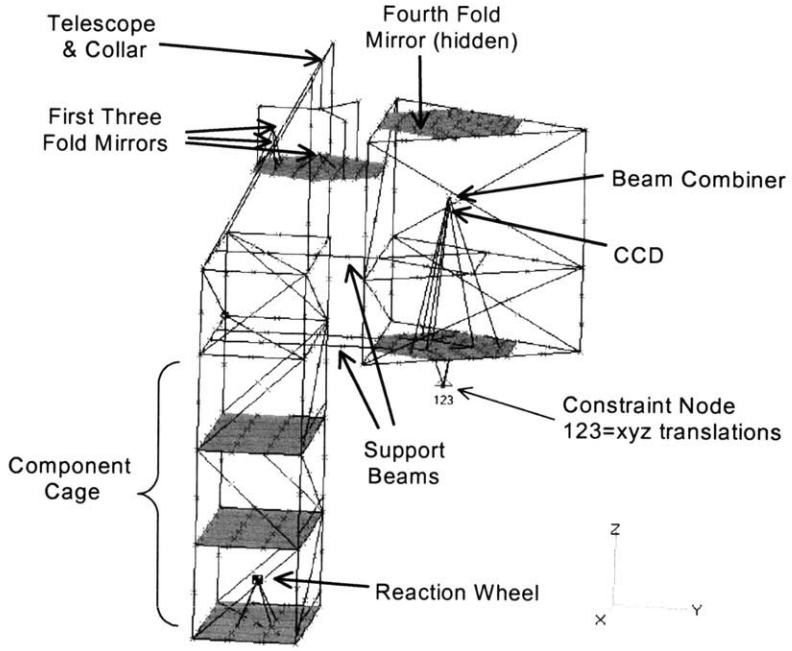


**Figure 4.9** Subaperture and Center Bus

The telescope and collar are modeled as a single rigid element connected the top of the beams supporting the collar to each other. This simplification is made because the collar is holding onto the telescope near the location of the primary mirror and the mirror is made out of rigid glass material. The component cage is modeled in more detail using beams to capture the geometry and plates to model the rack. The component cage is modeled in detail since the reaction wheel disturbances are added to the system via the bottom rack. The optical train is modeled by placing a node at the location of the center of each optical component.

Figure 4.10 illustrates the total deformation of the first mode shape. The image shows that the bending in the sagging direction is a fundamental mode.

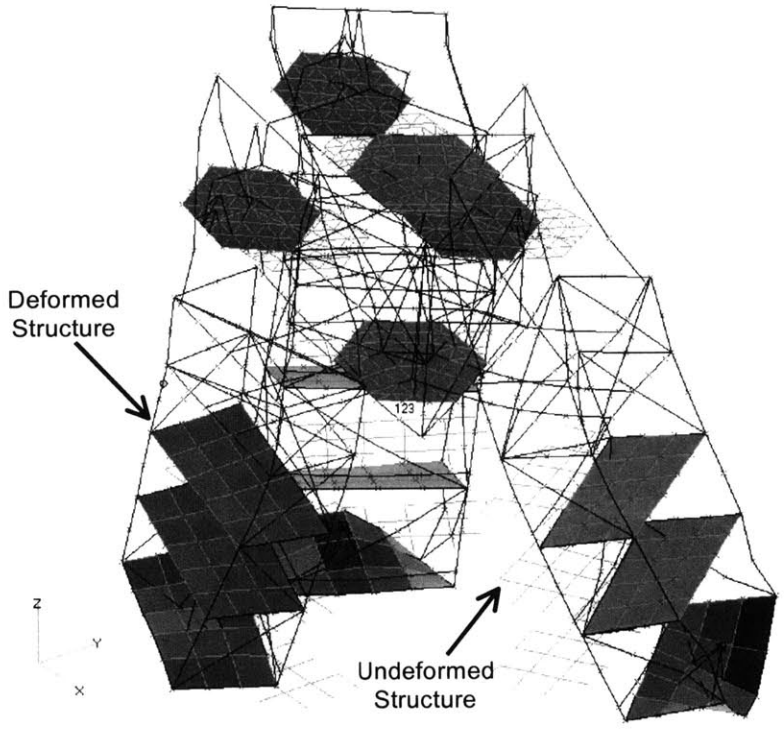


**Figure 4.10** First Mode Shape [52.7 Hz]

### 4.2.2 Disturbance Model

Reaction wheels are expected to be the largest source of disturbances on ARGOS. RWA spin at high speeds and may vibrate due to static and dynamic imbalances. These vibrations can impinge on the structure causing undesired motion of the optical components.

Static imbalance is the offset of the center of gravity from the axis of rotation. It is modeled as a small mass, $m_s$, at distance, $r_s$, that displaces the center of gravity from the center of rotation along the radial direction (Figure 4.11(a)). The dynamic imbalance is the offset of the principal axial axis from the axis of rotation. It is modeled as a pair of small masses, $m_d$, at distance, $r_d$, that are displaced in the z direction, one above the radial axis and one below by distance, h (Figure 4.11(b)) [Bialke, 1997].

The ARGOS reaction wheels are not yet built, but are expected to have a vibration environment similar to that of unbalanced, off-the-shelf professional wheels. Therefore, RWA

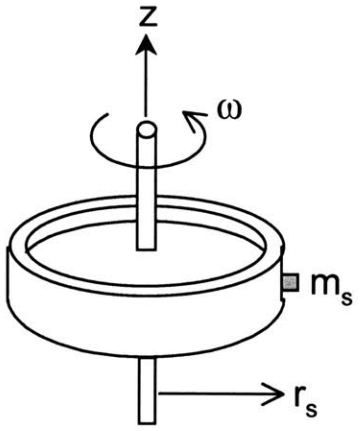


Figure 4.11(a) Static Imbalance

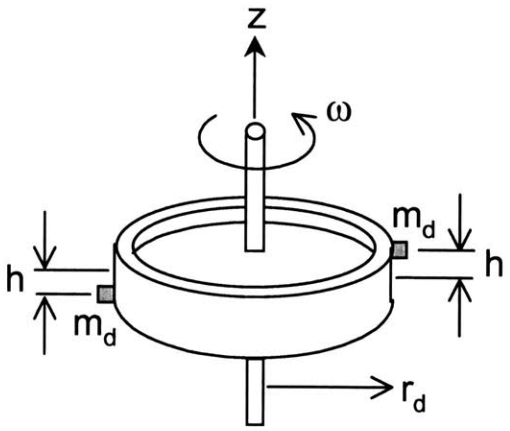


Figure 4.11(b) Dynamic Imbalance

**Figure 4.11** Reaction Wheel Imbalance Representation

disturbance model used in the disturbance analysis is one based on vibration data taken from an Ithaco B Wheel (model TW-16B32), by Orbital Sciences, in February and April of 1997. The disturbance model was created by Masterson [Masterson, 1999].

The disturbance caused by the reaction wheels are expressed as a vector, **m**, of three forces (one in the axial and two in the radial) and three moments (again, one in the axial and two in the radial). From empirical analysis of reaction wheel test data, these disturbances have been found to be tonal in nature occurring at certain harmonics of the wheel speed and their amplitudes can be expressed as a function of the wheel speeds squared:

$$m_{ij}(t) = C_j f_i^2 \sin(2\pi h_j f_i t + \phi_{ij}) \tag{4.1}$$

where m(t) is the disturbance, C is the amplitude coefficient, f is the wheel speed, h is the harmonic number, $\phi$ is the phase, the subscript i indicates the wheel speed, and j indicates the disturbance type. The disturbance type refers to whether the disturbance is a force or a moment and if it is in the axial or radial directions. The harmonics and amplitude coefficients for the Ithaco B-Wheel are given in Table 4.6.

**TABLE 4.6** Ithaco B Wheel Model [Masterson, 1999]

| Radial Force | | Radial Moment | | Axial Moment | |
|---|---|---|---|---|---|
| h | C [N/rpm$^2$] | h | C [Nm/rpm$^2$] | h | C [Nm/rpm$^2$] |
| 0.99 | 2.134 e-8 | .99 | 6.305 e-9 | 0.99 | 7.27 e-9 |
| 1.99 | 5.10 e-9 | 1.99 | 1.314 e-9 | 1.41 | 4.97 e-9 |
| 2.46 | 6.09 e-9 | 3.16 | 8.89 e-10 | 2.82 | 9.75 e-9 |
| 3.16 | 7.83 e-9 | 4.56 | 2.609 e-9 | 5.95 | 1.9889 e-8 |
| 3.87 | 5.28 e-9 | 5.28 | 3.722 e-9 | | |
| 4.56 | 9.05 e-9 | 5.97 | 2.375 e-9 | | |
| 5.28 | 1.752 e-8 | 6.23 | 2.763 e-9 | | |
| 5.98 | 3.04 e-8 | 6.68 | 3.347 e-9 | | |
| 6.71 | 2.053 e-8 | 7.38 | 4.767 e-9 | | |
| 8.09 | 3.246 e-8 | 8.09 | 4.005 e-9 | | |
| 8.83 | 3.517 e-8 | 8.80 | | | |
| 9.54 | 2.991 e-8 | | | | |
| 10.25 | 3.138 e-8 | | | | |

Equation (4.1) models RWA disturbances at discrete wheel speeds. However, RWAs operate in a range of speeds. Melody developed a stochastic broadband model of the RWA disturbances assuming that the wheel speed is a random variable [Melody, 1995]. The Power Spectral Densities (PSDs) for the stochastic model of the B-wheel is shown as the dashed lines in Figure 4.12. The state space model (solid lines) is fit to the broadband disturbance PSDs for use in disturbance analysis.

Because the wheel is symmetric in the radial direction, the forces and moments in and about the radial directions differ by only 90 degree phase and are combined. The moment about the axial direction due to imbalances is considered to be negligible compared to the total moment about the axial direction. Thus, in the wheel frame of reference, there are only three types of disturbances, the radial force, radial moment and the axial force.

Recall that the disturbance state-space representation is given by equation (2.23), rewritten here:

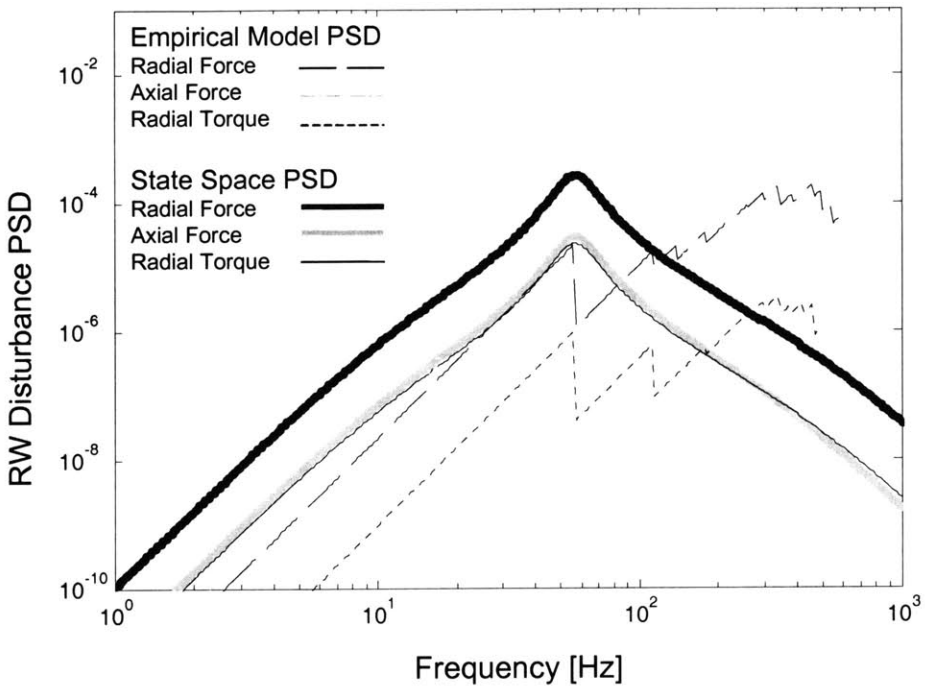


**Figure 4.12** B-Wheel Disturbance PSD's in Wheel Frame

$$\begin{aligned} \dot{\mathbf{q}}_d &= \mathbf{A}_d\mathbf{q}_d + \mathbf{B}_d\mathbf{d} \\ {}^{w}\mathbf{w} &= \mathbf{C}_d\mathbf{q}_d \end{aligned} \tag{4.2}$$

where the superscript, w, indicates that the model is in the wheel reference frame (Figure 4.12). The disturbances, ${}^{w}\mathbf{w}$, correspond to the reaction wheel disturbances, ${}^{w}\mathbf{w}$, must be converted to the spacecraft frame before being inputted as plant disturbances. Equation (2.22) rewritten here from Chapter 2, is the plant's state-space representation:

$$\begin{aligned} \dot{\mathbf{q}}_p &= \mathbf{A}_p\mathbf{q}_p + \mathbf{B}_w{}^{s/c}\mathbf{w} \\ \mathbf{z} &= \mathbf{C}_z\mathbf{q}_p \end{aligned} \tag{4.3}$$

where the superscript, s/c, indicates the disturbance in the spacecraft frame. Homero Gutierrez developed methods to transfer the reaction wheel disturbance models from the wheel

frame to the spacecraft frame [Gutierrez, 1999]. The attitude of the reaction wheels are defined using Euler angles as defined in Figure 4.13.

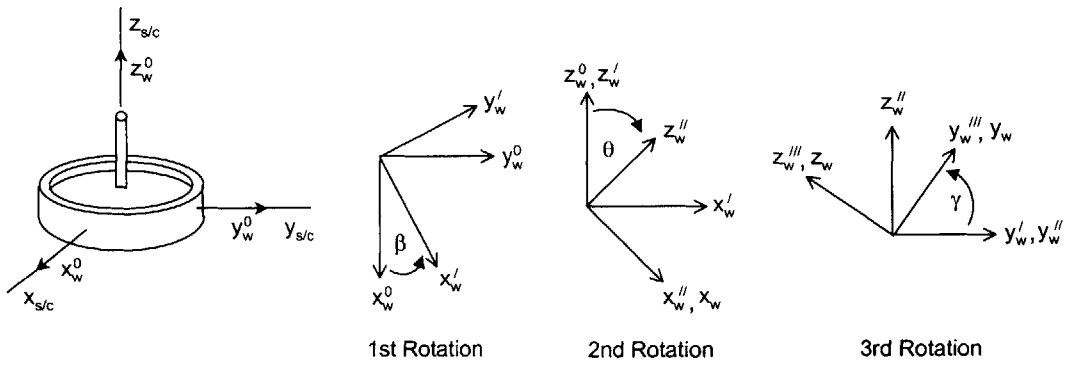


**Figure 4.13** Euler Angles (s/c denotes spacecraft frame; w denotes wheel frame) [Gutierrez, 1999]

The first rotation, $\beta$, is about the wheel's original z axis. The second rotation, $\theta$, is about the wheel's new y axis after the first rotation. The third rotation, $\gamma$, is about the wheel's new x axis after the second rotation. The wheels on ARGOS are arranged 120 degrees about the center and angled 45 degrees down from the vertical pointing radially outward (angled 45 degrees up towards the center) as shown in Figure 4.14.

The combination of the three angles are non-unique since the wheels are symmetric in the radial direction. The orientation angles are chosen such that the only angle that is different between the three wheels is $\beta$, the rotation about z, and such that the third rotation, $\gamma$, is zero. The angles for the three wheels are $\beta_1 = 270$, $\beta_2 = 30$, $\beta_3 = 150$, $\theta = 135$, $\gamma = 0$.

The position of the wheels are given by vector ${}^{w}\mathbf{r}$. The elements of r correspond to the position of the spacecraft CG from the wheel's CG and are the same for all three wheels. The position vector for all three wheels are:

$$ {}^{w}\mathbf{r} = \begin{bmatrix} -0.044 & 0.000 & -0.420 \end{bmatrix}^{T} \tag{4.4} $$

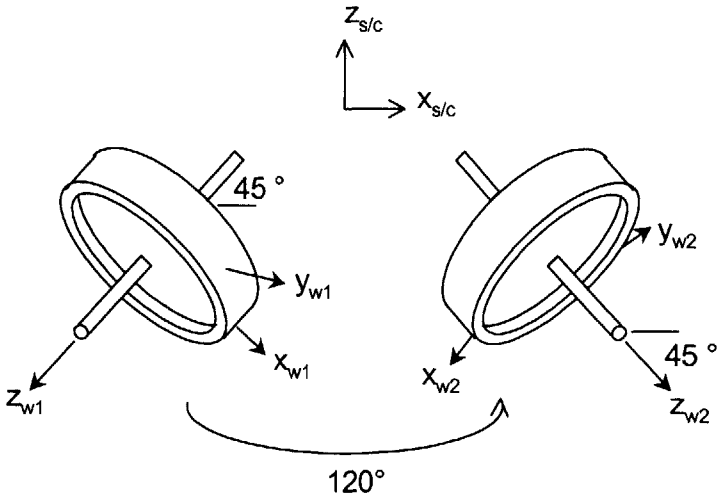


**Figure 4.14** Reaction wheel orientation

**TABLE 4.7** ARGOS wheel Euler angles

| Wheel # | β | θ | γ |
|---|---|---|---|
| 1 | 270 | 135 | 0 |
| 2 | 30 | 135 | 0 |
| 3 | 150 | 135 | 0 |

The Euler angles and the position vector are used to calculate a transformation matrix, **T**, such that Equations (4.2) and (4.3) can be combined to give the following equation for the appended plant and disturbance state-space system:

$$\dot{\mathbf{q}} = \begin{bmatrix} \mathbf{A}_d & 0 \\ \mathbf{B}_w\mathbf{T}\mathbf{C}_d & \mathbf{A}_p \end{bmatrix}\mathbf{q} + \begin{bmatrix} \mathbf{B}_d \\ 0 \end{bmatrix}\mathbf{d}$$
$$\mathbf{z} = \begin{bmatrix} 0 & \mathbf{C}_z \end{bmatrix}\mathbf{q} \tag{4.5}$$

## 4.2.3 Optical Sensitivity

The performance for ARGOS is the optical path length difference (OPD) of the light traveling through two different subapertures to the CCD camera. If the path length of light

traveling through the subapertures are termed $OPL_1$, $OPL_2$ and $OPL_3$, then there are three possible OPDs to calculate:

$$\begin{aligned} OPD_{12} &= OPL_1 - OPL_2 \\ OPD_{23} &= OPL_2 - OPL_3 \\ OPD_{13} &= OPL_1 - OPL_3 \end{aligned} \tag{4.6}$$

However, there are only two unique OPDs to calculate since the third equation is a linear combination of the first two:

$$\begin{aligned} OPD_{13} &= OPD_{12} + OPD_{23} \\ &= (OPL_1 - OPL_2) + (OPL_2 - OPL_3) \\ &= OPL_1 - OPL_3 \end{aligned} \tag{4.7}$$

To get the optical path length difference, first the optical path length of one subaperture must be calculated. The OPL is calculated by summing the distances the light travels between elements in the optical train. However, it is necessary to calculate the OPL as a function of mirror translations and rotations. The calculation can easily be used for the other two subaperture OPLs by simply changing the element nodes and rotating the sensitivities since they are dependent upon the degrees of freedom with respect to the spacecraft frame.

Assuming small displacements, the OPL is calculated as a function of the nodal displacements using finite differences. The first step is to calculating the nominal OPL for the optical train. The next step is then to perturb one degree of freedom by a known amount and calculate the new OPL. This step is iterated through all the degrees of freedom throughout the optical train. A linear sensitivity is assumed such that the change in the ODL is given by:

$$\Delta OPL = \sum_{i=1}^{n} \left( \frac{OPL_i - OPL_0}{\Delta x_i} \right) \Delta x_i \tag{4.8}$$

where the quantity within the parentheses is the sensitivity of the $i^{th}$ degree of freedom. Figure 4.15 shows an example of a sensitivity calculation. The light enters at node a and bounces off two flat mirrors (b and c) at 45 degree angles and exits at d. The nominal path-length is shown by the dotted lines and the new pathlength is shown by the solid line.

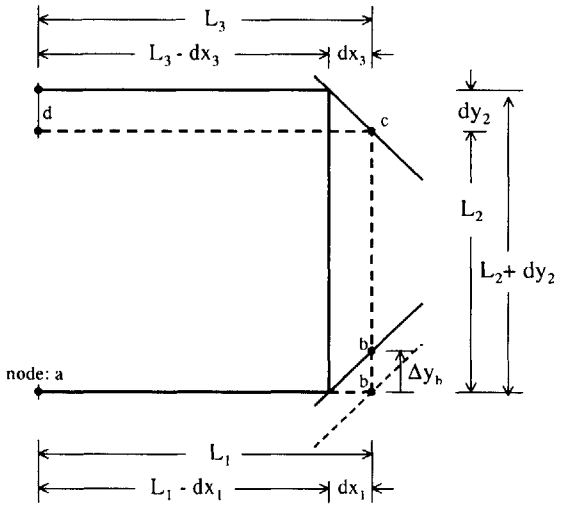


**Figure 4.15** Example calculation of optical path length sensitivity

The pathlengths for the example are given by the following equations:

$$\begin{aligned} OPL_0 &= L_1 + L_2 + L_3 \\ OPL_{\Delta y_b} &= (L_1 - dx_1) + (L_2 + dy_2) + (L_3 - dx_3) \end{aligned} \tag{4.9}$$

Because the mirrors at b and c are nominally at 45 degrees to the light path, $dx_1$, $dy_2$ and $dx_3$ are all equal to $\Delta y_b$. The difference and sensitivity are then calculated to be:

$$\begin{aligned} \Delta OPD_{\Delta y_b} &= -\Delta y_b \\ \frac{\Delta OPD_{\Delta y_b}}{\Delta y_b} &= -1 \end{aligned} \tag{4.10}$$

The optical sensitivity matrix for ARGOS was conducted in a similar fashion, yet with the assistance of a software code developed by Masterson [Masterson, 2000]. The code

requires the geometrical layout of the optical train, the prescription of each optic and the incident ray direction (Figure 4.16).

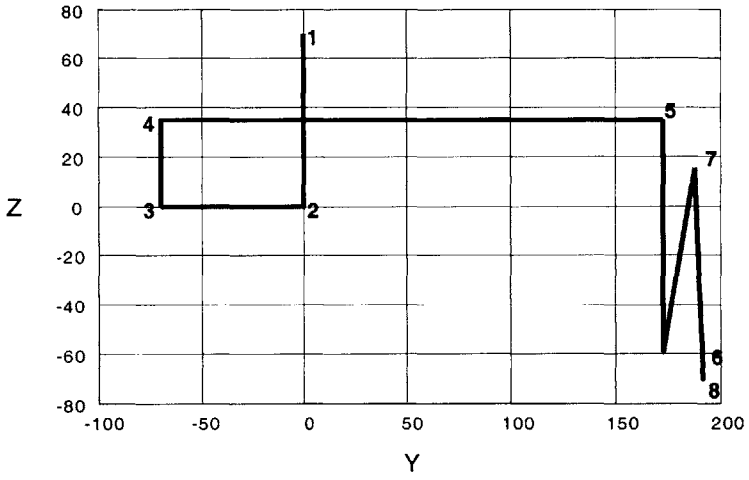


**Figure 4.16** Ray trace for sensitivity calculation

## 4.3 Disturbance Analysis

The A,B,C,D state-space matrices are created for the structure and the disturbances. The A matrix is created from the structural dynamics of the system. The B matrix is the disturbance input matrix denoting where the reaction wheel noise enters the system. The C matrix is created from the optical sensitivities.

The PSD of the disturbance to performance behavior of ARGOS is the bottom figure in Figure 4.17. The methods to calculate the plots are from Gutierrez [Gutierrez, 1999]. The area under the PSD curve is the RMS of the performance. The cumulative RMS plot above the PSD is the integral of the PSD as a function of the frequency. The large jumps in the cumulative RMS curve indicate modes that contribute significantly to the total RMS. Table 4.8 lists the modal frequencies corresponding to the jumps in OPD1 and OPD2; these are approximate values taken empirically from the cumulative RMS plot.

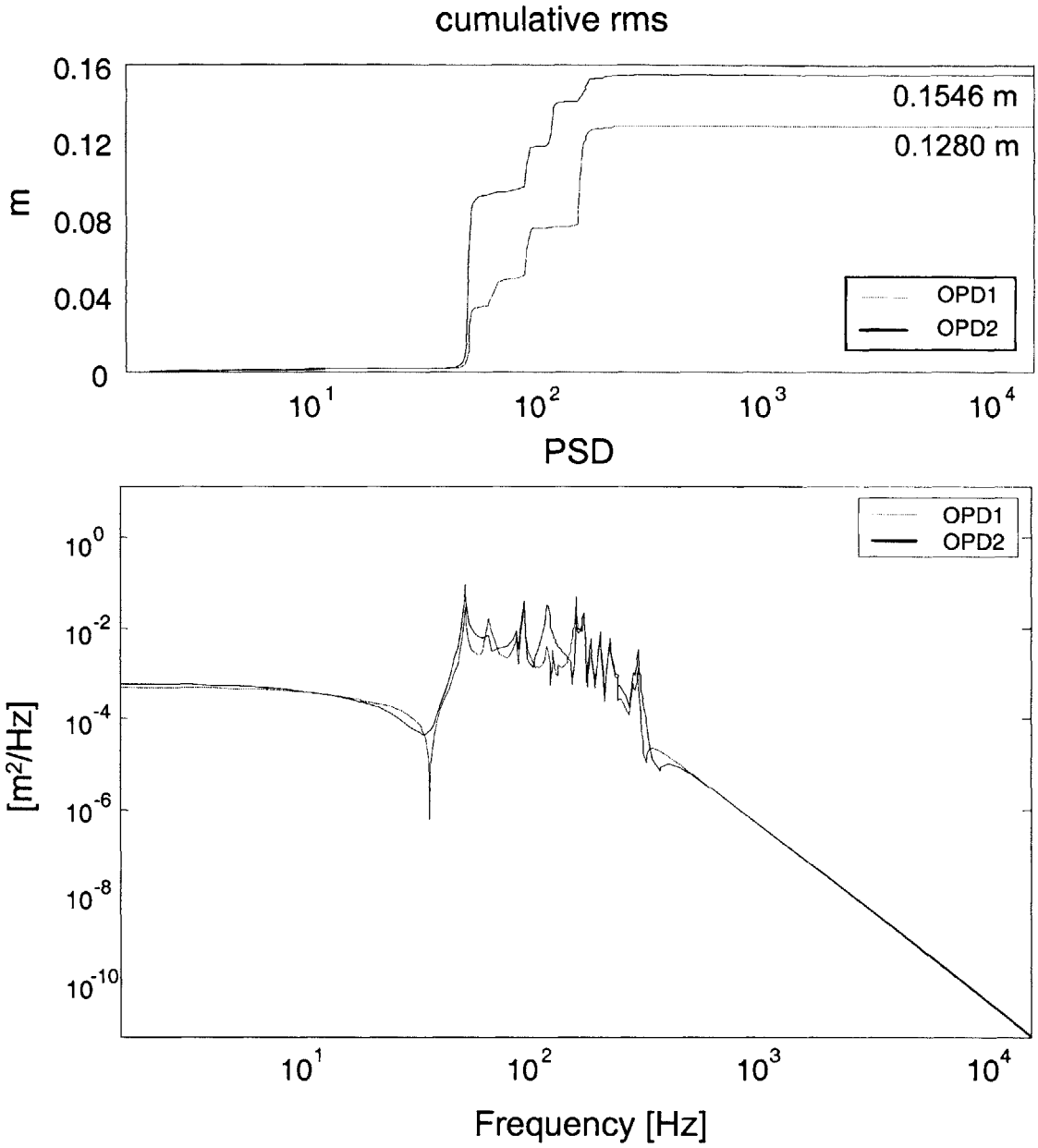


**Figure 4.17** PSD and cumulative RMS for ARGOS

The analysis of the low fidelity stick model in the sample problem showed that the overall modal behavior, such as the mode shape and the slope of the PSD, are similar to the truth model. However, the natural frequencies are not of the same order of magnitude of the

**TABLE 4.8** Critical Modes

| Natural Frequencies [Hz] | |
|---|---|
| **OPD1** | **OPD2** |
| 52 | 52 |
| 67 | 97 |
| 95 | 122 |
| 164 | 179 |

truth model. For a higher fidelity stick model, the natural frequencies are of the same order of magnitude as those for the truth model.

The finite element model of ARGOS is considered to be a low fidelity stick model. It is the first model to be created for disturbance analysis with many assumptions for simplification. As such, the RMS values calculated from the PSD of the ARGOS stick model only indicate the order of magnitude of the OPD. The results obtained indicate that the structure must be stiffened to meet requirements. The mode shapes can be used to determine critical locations for redesign.

For example, the 52 Hz mode corresponds to the first mode of the system shown in Figure 4.10. This is a critical mode for both OPD metrics and is the most significant contributor to OPD2. This result indicates that the bending of ARGOS subsystems in the sag direction is the most flexible of the three bending stiffnesses shown in Figure 4.6. The actual values calculated for OPD1 RMS and OPD2 RMS are 0.12 m and 0.15 m.

Two more mode shapes are shown in Figure 4.18, corresponding to the critical modes at 95 Hz and 97 Hz. Mode #13 is in the twist bending direction and its contribution to the OPD indicates that ARGOS should be stiffened in this direction. One solution is the addition of another beam or beams perpendicular to the support beams to hold them together. Mode #14 is the local plate mode of the rack holding the reaction wheels. The plate and the component cage beams are not stiff enough to isolate the RWA disturbances from the rest of the structure.

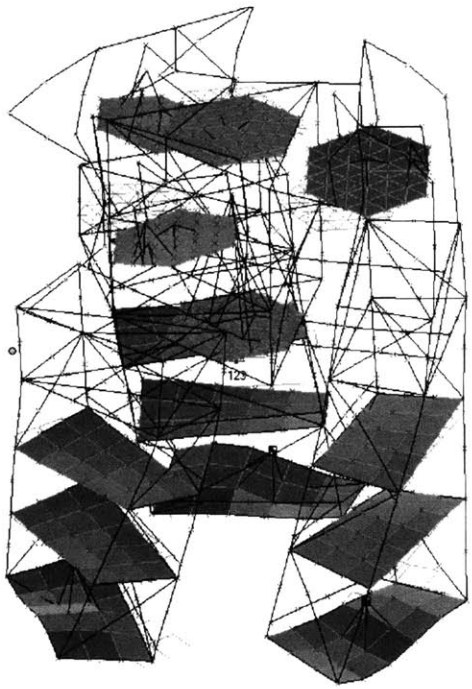

Figure 4.18(a) Mode #13 [95.9 Hz]

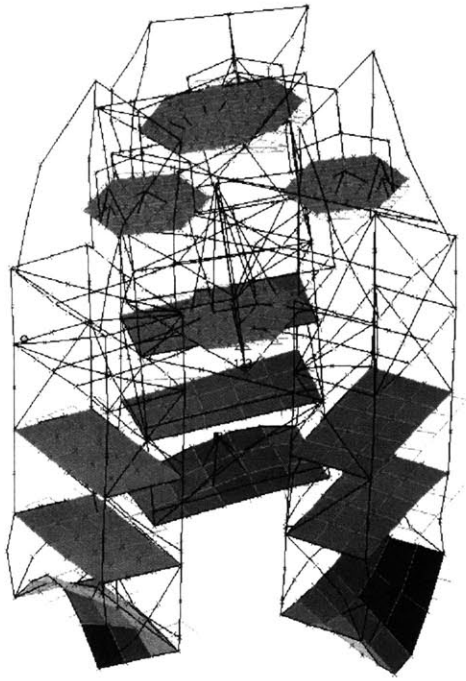

Figure 4.18(b) Mode #14 [98.8 Hz]

**Figure 4.18** High frequency mode shapes for ARGOS

## 4.4 Summary

A first run disturbance analysis of ARGOS indicates that the structure as it currently is designed, is not stiff enough to isolate the optical elements from the disturbances of the reaction wheels. The numerical results of the analysis are indicators of the order of magnitude of the OPD. The critical modes determined through the cumulative RMS plots and their corresponding mode shapes determine where the structural design of ARGOS must be improved. The structural model of ARGOS created to run the analysis is a low fidelity model that will require more refinement as the design matures.

# Chapter 5

# CONCLUSION

## 5.1 Summary

Space telescopes are large, deployable flexible structures that operate in a disturbance environment. To meet their performance requirements, they must demonstrate high stability and pointing accuracy. The size of space telescopes and their 0-g design inhibit full-scale testing on the ground; therefore, accurate models are necessary to predict their performances.

The accuracy of the performance predictions depends upon the level of fidelity of the model. Model fidelity is dependent upon design maturity and model updating. A truss sample problem in Chapter 2 is used to describe the different stages of model fidelity. The design maturity is simulated by different finite element types: (listed in order of increasing fidelity) a Bernoulli-Euler beam, a Timoshenko beam, a truss with rod elements and a truss with bending beam elements. Model updating is simulated by meshing the finite elements at different degrees of refinement. The models are compared to a "truth" model, which is the highly refined truss with bending elements.

Chapter 3 presents the Origins Testbed (OT) as an example of a mature model that is based upon a structure which has been built. Experimental data is available to compare the analytical model transfer functions to assess the fidelity of the analytical model. The pro-

cess of modeling the OT is used as an analogy of the evolution of model fidelity due to design maturity.

Chapter 4 presents the ARGOS testbed as an example of a low fidelity model at a low design maturity level. Though the design of ARGOS is still being changed, one iteration is fixed in order to complete a disturbance analysis. The disturbance analysis requires the development of a reaction wheel disturbance model using Ithaco B-wheels as the disturbance source for ARGOS. Additionally, a sensitivity matrix for the optical train is developed to calculate the performances. The disturbance analysis results are examined based upon the knowledge gained from the sample problem. Only the order of magnitude of the resulting OPD is considered, which indicates that the design of the structure of ARGOS requires significant improvements. The cumulative RMS plot indicates the modes that contribute significantly to the total RMS. The numerical values of the natural frequencies are not significant for low fidelity models. The non-parametric errors from incorrect modeling assumptions and the low design maturity of ARGOS prevent any direct correlation of the modes of a low fidelity model to the final system.

## 5.2 Conclusions

The analysis of model fidelity in chapter 2 is important for understanding how much information can be drawn from the disturbance analysis of a low fidelity model. All levels of fidelity of the truth model have similar transfer function characteristics, such as the backbone and shape of the fundamental modes. The low fidelity models can also predict the mode shapes of the low frequency modes.

The non-parametric errors dominate in the low fidelity models and parametric errors dominate in higher fidelity models. As such, for low maturity designs, estimates of parameter values do not adversely affect the performance predictions; the errors associated by the parameter errors are insignificant compared to those due to the low maturity level of the design.

The analysis in Chapter 3 shows that even if the structure being modeled has been built, the analytical model is still prone to errors. The benefit of having a completed structure is to have a truth model with which to compare the analytical model. The errors associated with different levels of model updating of the analytical model parallel those associated with model fidelity. Lower levels of the model updating have errors dominated by non-parametric errors, due to assumptions in the modeling.

In Chapter 4, the interpretation of the disturbance analysis of ARGOS indicates that the design does not adequately isolate the optics from the disturbances caused by the reaction wheels. The mode shapes corresponding to the critical modes of the system show which parts of the ARGOS structure must be stiffened.

## 5.3 Future Work

The exploration of model fidelity in this thesis is mainly qualitative. To make model fidelity evolution error analysis more useful for designing complex structures, quantitative metrics should be developed. These metrics would identify the level of fidelity of a model, exactly what information is to be used from low fidelity disturbance analysis and an accurate prediction of the error in the performance calculation.

The model updating of the Origins Testbed must continue in order to have a working analytical model to use for future research efforts. The discrepancy between the gains of the analytical models shown in Chapter 3 and the experimental data must be solved. One suggestion is to redo the system identification of the OT and recalculate the conversion factors (Newton-meter to Volt-Volt) for the data. If all modeling assumptions are checked, then automatic modeling procedures, such as those described by Glease [Glease, 1994], can complete the model updating process.

Work on ARGOS is still progressing. As the design evolves, several more design iterations should be frozen for a disturbance analysis. The information from the disturbance analyses should be used to correct the structural design in order to improve the perfor-

mance. The disturbance analysis conducted in this thesis shows that the support beams that hold the subapertures and center bus together must be redesigned to improve resistance to sag, twist and radial bending. Additionally, the component cage beams and plates must be strengthened to adequately support the reaction wheels. Other suggestions for improving the model is to add the masses of the optics, masses of the subsystems, the dimensions of the Takahashi, and improve the model of the racks which hold the subsystems in the component cage.

# REFERENCES


*[Basdogan, 1999]* Basdogan, I., Dekens, F., Neat, G., "An Integrated Model Validation Study of the Wave Front Tip/Tilt System Using the Micro-Precision Interferometer Testbed," *IEEE Aerospace Conference*, Aspen, Colorado, March 1999, Proceedings Vol 4, pp25-32.

*[Berman, 1995]* Berman, Alex, "Multiple Acceptable Solutions in Structural Model Improvement," *AIAA Journal*, vol 33, No. 5, May 1995, pp 924-927.

*[Berman, 1999]* Berman, Alex, "The Inherently Incomplete FEM and its Effects on Model Updating Techniques," 1999, AIAA Paper #99-1450.

*[Bialke, 1997]* Bialke, B., "A Compilation of Reaction Wheel Induced Spacecraft Disturbances," *20th Annual American Aeronautical Society Guidance and Control Conference*, February 1997, AAS paper 97-038.

*[Blakely, 1993]* Blakely, Ken, *MSC/NASTRAN User's Guide: Basic Dynamic Analysis*, The MacNeal-Schwendler Corporation, U.S.A., 1993.

*[Bourgault, 2000]* Bourgault, Frederick, *Model Uncertainty and Performance Analysis for Precision Controlled Space Structures*, MIT S.M. Thesis in Aeronautical and Astronautical Engineering, 2000.

*[CDIO, 2001]* CDIO, *ARGOS Design Document*, MIT Department of Aeronautics and Astronautics, 16.684 Experimental CDIO Capstone Course, Spring semester, 2001.

*[Dawe, 1978]* Dawe, D.J., "A Finite Element for the Vibration Analysis of Timoshenko Beams", *Journal of Sound and Vibration*, Vol 60, 1978, pp 11-20.

*[DeBlonk, 1996]* deBlonk, Brett, Gutierrez, H., Ingham, M., Kenny, S., Kim, Y., Mallory, G., *Origins Technology Testbed: Experiments Requirements Document*, MIT Space Engineering Research Center, Oct. 11, 1996.

*[DeWeck, 1999]* de Weck, Olivier L., *Integrated Modeling and Dynamics Simulation for the Next Generation Space Telescope*, MIT S.M. Thesis in Aeronautical and Astronautical Engineering, 1999.

*[DeWeck, 2000]* de Weck, Olivier L., Miller, D. W., *Introduction to Isoperformance Analysis for Precision Opt-Mechanical Space Systems: Application to Bivariate Problems*, Research Memorandum, MIT SSL, May 19, 2000.

*[DeWeck, 2001]* de Weck, Olivier L., *Multivariable Isoperformance Methodology for*

*Precision Opto-Mechanical Systems*, MIT Ph.D. Thesis in Aeronautical and Astronautical Engineering, 2001.

*[DeYoung, 1998]* DeYoung, D., Dillow, J., Corcoran, S., Andrews, E., Yellowhair, J., DeVries, K., *Ground Demonstration of an Optical Control System for a Space-Based Sparse Aperture Telescope*, SPIE Conference on Space Telescopes and Instruments V, Kona, Hawaii, March 1998, SPIE vol 3356, pp 1156-1167.

*[Donaldson, 1993]* Donaldson, Bruce, *Analysis of Aircraft Structures: An Introduction*, McGraw-Hill, Inc., USA (1993).

*[Dressler, 1996]* Dressler, Alan (ed.), *Exploration and the Search for Origins: A Vision for Ultraviolet-Optical-Infrared Space Astronomy*, Report of the "HST and Beyond" Committee, Association of Universities for Research in Astronomy, Washington, DC. May 1996.

*[Elias, 2001]* Elias, Laila, *A Structurally Coupled Disturbance Analysis Method Using Dynamic Mass Measurement Techniques, with Application to Spacecraft-Reaction Wheel Systems*, MIT S.M. Thesis in Aeronautical and Astronautical Engineering, 2001.

*[Gere, 1997]* Gere, James M., *Mechanics of Materials 4ed*, PWS Publishing Co., USA (1997).

*[Glease, 1994]* Glease, Roger M., *Development of Zero-Gravity Structural Control Models from Analysis and Ground Experimentation*, MIT S.M. Thesis in Aeronautical and Astronautical Engineering, January 1994.

*[Gutierrez, 1999]* Gutierrez, Homero, *Performance Assessment and Enhancement of Precision Controlled Structures During Conceptual Design*, MIT Ph.D. Thesis in Aeronautical and Astronautical Engineering, 1999.

*[Huang, 1961]* Huang, T.C., "The Effect of Rotary Inertia and of Shear Deformation on the Frequency and Normal Mode Equations of Uniform Beams With Simple End Conditions", *Journal of Applied Mechanics*, Trans. of ASME, Vol 28, pp. 579-584, ASME, Applied Mechanics Division, 1961.

*[Huang, 1963]* Huang, T.C., Kung, C.S., "New Tables of Eigenfunctions Representing Normal Modes of Vibration of Timoshenko Beams", *Developments in Theoretical and Applied Mechanics I.*, 1963, pp 59-71.

*[Joshi, 1997]* Joshi, S., Melody, J., Neat, G., "A Case Study of the Role of Structural/ Optical Model Fidelity in Performance Prediction of Complex Opto-Mechanical Instruments," *IEEE Proceedings of the 36th Conference on Decision and Control*, San Diego, California, December 1997, pp 1367-1372.

*[Kilroy, 1997]* Kilroy, Kevin (ed.), *MSC/NASTRAN Version 70 Quick Reference Guide*, The MacNeal-Schwendler Corporation, U.S.A., 1997.

*[Mallory, 1998]* Mallory, Gregory, Gutierrez, H., Miller, D.W., *MIT Origins Testbed: Initial Control Results*, SSL, MIT, 1998.

*[Mallory, 2000a]* Mallory, Gregory, *Development and Experimental Validation of Direct Controller Tuning for Spaceborne Telescopes*, MIT Ph.D. Thesis in Aeronautical and Astronautical Engineering, 2000.

*[Mallory, 2000b]* Mallory, Gregory, Saenz-Otero, A., Miller, D. W., "Origins Testbed: Capturing the Dynamics of Future Space-Based Telescopes", *Optical Engineering*, Vol 39 Num 6 pp1665-1676, Society of Photo-Optical Instrumentation Engineers, June 2000

*[Marco-Gomez,1999]* Marco-Gomez, V., Lopez-Diez, J., Luengo, P., "Finite Element Model of a Large Spacecraft Structure Updated with Modal Test," AIAA Paper 99-1452, pp 2084-2090.

*[Masterson, 1999]* Masterson, Rebecca A., *Development and Validation of Empirical and Analytical Reaction Wheel Disturbance Models*, MIT S.M. Thesis in Aeronautical and Astronautical Engineering, 1999.

*[Masterson, 2000]* Masterson, R., *Matlab Optical Toolbox for Jitter Analysis*, TRW Interoffice Memorandum, July 12, 2000.

*[Meirovich, 1975]* Meirovich, Leonard, *Elements of Vibration Analysis*, McGraw-Hill Book Company, USA (1975).

*[Meirovich, 1997]* Meirovich, Leonard, *Principles and Techniques of Vibrations*, Prentice-Hall, Inc, USA (1997).

*[Melody, 1995]* Melody, J.W., *Discrete Frequency and Broadband Reaction Wheel Disturbance Models*, JPL Interoffice Memorandum, 3411-95-200csi, June 1, 1995.

*[Melody, 1996]* Melody, J., Neat, G., "Integrated Modeling Methodology Validation Using the Micro-Precision Interferometer Testbed," *IEEE Proceedings of the 35th Conference on Decision and Control*, Kobe, Japan, December 1996, Proceeding Vol 4, pp 4222-4227.

*[Moses, 1998]* Moses, S., Iwens, R., Grimm, G., "Verification of the Performance of Large, Space-Based Astronomical Observatories: AXAF Experience and SIM Approaches," *SPIE Conference on Space Telescopes and Instruments V*, Kona, Hawaii, March 1998, SPIE vol 3356, pp 1179-1189.

*[Mosier, 1998a]* Mosier, G., Femiano, M., Ha, K., Bely, P., Burg, R., Redding, D., Kissil,

A., Rakoczy, J., Craig, L., "An Integrated Modeling Environment for Systems-level Performance Analysis of the Next Generation Space Telescope," *SPIE Conference on Space Telescopes and Instruments V*, SPIE vol 3356, Kona, Hawaii, March 1998, pp 89-97.

*[Mosier, 1998b]* Mosier, G., Femiano, M., Ha, K., Bely, P., Burg, R., Redding, D., Kissil, A., Rakoczy, J., Craig, L., "Fine Pointing Control for a Next Generation Space Telescope," *SPIE Conference on Space Telescopes and Instruments V*, SPIE vol 3356, Kona, Hawaii, March 1998, pp 1070-1077.

*[Necib, 1989]* Necib, B., Sun, T.C., "Analysis of Truss Beams Using a High Order Timoshenko Beam Finite Element," *Journal of Sound and Vibration*, vol 130, 1989, pp 149-159.

*[Noecker, 1999]* Noecker, M. C., Leitch, J., Kopp, G., McComas, B., "Optical Design for Terrestrial Planet Finder," *Proceedings of SPIE - the International Society for Optical Engineering*. Vol 3779 1999. pp 40-46.

*[Petyt, 1990]* Petyt, Maurice, *Introduction to Finite Element Vibration Analysis*, Cambridge University Press, Great Britain, 1990.

*[Robertson, 1997]* Robertson, L., Leitner, J., Slater, J., deBlonk, B., "Integrated Modeling and Control of the UltraLITE System," *IEEE Aerospace Conference*, Aspen, Colorado, February 1997, Proceedings Vol 2, pp 337-355.

*[Silva, 1983]* Silva, Julio M.M., Maia, Nuno M. M., *Modal Analysis and Testing*, Kluwer Academic Publishers, Netherlands, 1998.

*[Strang, 1986]* Strang, Gilbert, *Introduction to Applied Mathematics*, Wellesley-Cambridge Press, U.S.A., 1986.

*[Sun, 1981]* Sun, C.T., Kim, B.J., Bogdanoff, J.L., "On the Derivation of Equivalent Simple Models for Beam- and Plate-Like Structures in Dynamic Analysis", *Proceedings of the 22nd Structure, Structural Dynamic and Materials Conference*, 1981, pp 523-532.

*[Thomson, 1988]* Thomson, William T., *Theory of Vibration with Applications 3ED*, Prentice Hall, U.S.A., 1988.

*[Timoshenko, 1937]* Timoshenko, Stephen, *Vibration Problems in Engineering 2ED*, D. Van Nostrand Company, Inc., U.S.A., 1937.

*[Uebelhart, 2001]* Uebelhart, Scott A., *Conditioning, Reduction, and Disturbance Analysis of a Large Order Integrated Models for Space-Based Telescopes*, MIT S.M. Thesis in Aeronautical and Astronautical Engineering, 2001.